VOT 78237

MODELING AND SIMULATION OF QUANTUM NANOSTRUCTURES FOR SINGLE-ELECTRON TRANSISTORS

(PEMODELAN DAN SIMULASI STRUKTUR NANO KUANTUM BAGI TRANSISTOR ELEKTRON TUNGGAL)

AHMAD RADZI MAT ISA
MOHD KHALID KASMIN
NOR MUNIROH MUSA

PUSAT PENGURUSAN PENYELIDIKAN
UNIVERSITI TEKNOLOGI MALAYSIA

2009

VOT 78237

MODELING AND SIMULATION OF QUANTUM NANOSTRUCTURES FOR SINGLE-ELECTRON TRANSISTORS

(PEMODELAN DAN SIMULASI STRUKTUR NANO KUANTUM BAGI TRANSISTOR ELEKTRON TUNGGAL)

AHMAD RADZI MAT ISA
MOHD KHALID KASMIN
NOR MUNIROH MUSA

RESEARCH VOT NO:
78237

Jabatan Fizik
Fakulti Sains
Universiti Teknologi Malaysia

2009

ACKNOWLEDGEMENTS

First of all, in humble way I wish to give all the Praise to Allah, the Almighty God for with His mercy has given me the strength, *keredhaanNya* and time to complete this work.

I would like to express my sincere gratitude and appreciation to the Ministry of Higher Education for providing the financial support through FRGS funding. Thanks are also due to the Research Management Center of Universiti Teknologi Malaysia for the management of funds VOT No. 78237 for this project.

Thanks also to all my friends and colleagues for their views, concerns, encouragement and for their continuing support, patience, valuable advices and ideas throughout the duration of this research.

ABSTRACT

Semiconductor clusters have occupied the centre of scientific interest because of their unique electronic nature. Among the group III-V compound clusters, the gallium arsenide clusters have been the focus of this research due to their importance in constructing fast microelectric devices. The electronic structures of gallium arsenide clusters were studied. The simulations were carried out by using VASP (Vienna Ab-Initio Software Package) which utilizes the method of density functional theory (DFT) and plane wave basis set. Gallium arsenide clusters with surface passivated by hydrogen, $Ga_xAs_yH_z$ were simulated to obtain the density of states (DOS) as well as bandstructure for each cluster. From the DOS graphs, discrete spectrum was observed instead of bulk-like continuous DOS which is the evolvement from bulk to nano-size. Bandstructure graphs also showed the discrete energy level in consistence with the discrete energy spectrum from DOS. It was found that the bandgaps for hydrogenated gallium arsenide clusters increases with the decrease in size. Bare gallium arsenide clusters, Ga_xAs_y were also simulated ($x + y \leq 15$) gallium arsenide atoms. Optimization was performed to obtain the ground state structure. The bandgaps for the ground state gallium arsenide clusters do not show a decreasing trend with the increment of cluster size as that of hydrogenated gallium arsenide cluster. The electronic structures of optimized clusters are affected by the surface orientation of the clusters. Comparison of the bandgap values for $Ga_xAs_yH_z$ and Ga_xAs_y was made.

ABSTRAK

Semikonduktor kluster menjadi matlamat kajian dalam bidang sains disebabkan oleh sifat elektronik semulajadinya. Antara gabungan kluster kumpulan III-V, kluster gallium arsenida menjadi tumpuan dalam kajian ini kerana kepentingannya dalam pembuatan alat-alat mikroelektrik yang lebih pantas. Struktur elektronik kluster gallium arsenida telah dikaji. Simulasi kajian telah dijalankan dengan menggunakan perisian VASP (Vienna Ab-Initio Software Package) yang menggunakan teori fungsian ketumpatan dan set basis gelombang satah. Simulasi ke atas kluster gallium arsenida yang permukaannya dipasifkan dengan hidrogen, $Ga_xAs_yH_z$ telah dilakukan untuk mendapatkan ketumpatan keadaan dan juga struktur jalur untuk setiap kluster. Daripada graf ketumpatan keadaan, spektrum diskrit telah diperolehi. Perubahan ketumpatan keadaan daripada selanjar bagi struktur pukal ke spektrum diskrit bagi struktur nano merupakan evolusi nano. Struktur jalur juga menunjukkan aras tenaga diskrit yang selaras dengan spektrum diskrit daripada ketumpatan keadaan. Jurang jalur untuk gallium arsenida terhidrogenasi semakin berkurang apabila saiz kluster meningkat. Simulasi ke atas kluster gallium arsenik tulen (tak terhidrogenasi), Ga_xAs_y yang mempunyai bilangan atom ($x + y \leq 15$) juga dilakukan. Optimasi dilaksanakan untuk mendapatkan struktur keadaan dasar. Jurang jalur bagi struktur keadaan dasar kluster-kluster itu tidak mempunyai aliran yang menurun dengan peningkatan saiz kluster seperti yang berlaku pada kluster gallium arsenida terhidrogenasi. Struktur elektronik kluster-kluster optimum dipengaruhi oleh orientasi permukaan kluster. Perbandingan nilai jurang jalur bagi $Ga_xAs_yH_z$ dan Ga_xAs_y telah dilakukan.

TABLE OF CONTENTS

CHAPTER	TITLE	PAGE
	ACKNOWLEDGEMENTS	i
	ABSTRACT	ii
	ABSTRAK	iii
	TABLE OF CONTENTS	iv
	LIST OF TABLES	xi
	LIST OF FIGURES	xii
	LIST OF ABBREVIATIONS	xv
	LIST OF SYMBOLS	xviii
	LIST OF APPENDICES	xxi
1	**INTRODUCTION**	1
	1.1 Background of Research	1
	1.2 Atomic and Molecular Clusters	2
	1.3 Applications of Clusters	4
	1.4 Introduction to Modeling and Simulation	6
	1.4.1 Modeling and Simulation Approach Used in This Research	8
	1.5 Research Objectives	9
	1.6 Scopes of Study	9
	1.7 Outline of Dissertation	

10

2 COMPUTATIONAL METHOD 11

2.1 Computational Materials Science (CMS) 11

2.2 Density Functional Theory 16

2.2.1 Development of Density Functional Theory 17

2.2.2 Kohn-Sham Theory 18

2.2.3 Self-Consistent Field (SCF) 22

2.2.4 Non-Self Consistent Field 22

2.2.5 Exchange-Correlation Functionals 23

2.2.5.1 Local Density Approximation for Exchange-Correlation Energy 23

2.2.5.2 Generalized Gradient Approximation (GGA) 26

2.2.6 DFT Choice of Electronic Structure 30

2.3 Basis Set 32

2.3.1 Plane Wave Basis Set 33

2.3.2 Projected Augmented Wave (PAW) –Pseudopotentials (PP) in Plane Wave Basis 37

3 METHODOLOGY 39

3.1 Introduction to VASP 39

3.1.1 Software Packages Needed by VASP 41

3.2 Files Used by VASP 43

3.2.1 INCAR File 44

3.2.2 POTCAR File 44

3.2.3 POSCAR File 45

3.2.4 KPOINTS File 45

3.3 Algorithm Used in VASP 47

3.3.1 Conjugate Gradient Algorithm 51

3.3.2 Block Davidson Algorithms 52

3.3.3 Residual Minimization Scheme-Direct Inversion In The Iterative Subspace (RMM-DIIS) 53
3.4 Simulation Process 54
3.4.1 Construction of Clusters 55
3.4.2 Geometry Optimization 56
3.4.2.1 INCAR for Conjugate Gradient Geometry Optimization 58
3.4.2.2 INCAR for Simulate Annealing 60
3.4.2.3 KPOINTS for Geometry Optimization 65
3.4.3 Electronic Structures Calculations 65
3.4.3.1 INCAR for Self-Consistent Run 66
3.4.3.2 INCAR for Non-Selfconsistent Run 67
3.4.3.3 KPOINTS for Non-selfconsistent and Bandstructure 68

4 SIMULATION RESULT AND ANALYSIS 69
4.1 Simulation of Bulk Gallium Arsenide and Gallium Arsenide Dimer 69
4.2 The Effect of Size on the Electronic Structures of Gallium Arsenide Clusters 73
4.3 The Effect of Shape on the Electronic Structures of Gallium Arsenide Clusters 80
4.3.1 Optimized Geometry Structure 82
4.3.2 Electronic Structures 87
4.4 Effect of Hydrogen and Reconstructed Surface to Electronic Structures 102

5 SUMMARY AND CONCLUSION 105

5.1 Summary and Conclusion 105
5.2 Suggestions 108
5.2.1 Improvement of the Bandgap Accuracy 108
5.2.2 Improvement of the Computation Time 109

REFERENCES 113
APPENDICES 121

LIST OF TABLES

TABLE NO	TITLE	PAGE
1.1	Schematic classification of clusters according to the number *N* of atoms.	3
2.1	Comparison of accuracy of various computational tools.	31
3.1	A relatively large number of input and output files of VASP.	43
3.2	Coordinates of high symmetry *k*-points in Cartesian and reciprocal mode.	46
4.1	Bandgap energy for each of the cluster.	77
4.2	The configurations and point group for each of the gallium arsenide clusters, Ga_xAs_y.	82
4.3	Energy level (HOMO and LUMO) as well as bandgap value of each Ga_xAs_y clusters, ($x + y \leq 15$).	95
4.4	Binding energy per atom of each gallium arsenide cluster, Ga_xAs_y ($x + y \leq 15$). The binding energies are not corrected with zero potential energies.	96
4.5	Second-difference enegies and electron affinity of each gallium arsenide cluster, Ga_xAs_y ($x + y \leq 15$).	97
4.6	Bandgap (eV) comparison of bare non-optimized tetrahedral gallium arsenide clusters, hydrogenated gallium arsenide clusters and surface reconstructed gallium arsenide clusters.	102
5.1	Execution time, speedup and efficiency of VASP using parallel computing.	111

LIST OF FIGURES

FIGURE NO	TITLE	PAGE
1.1	Computational science is defined as the intersection of the three disciplines, i.e. computer science, mathematics and applied science.	8
2.1	Schematic depicting self-consistent loop.	21
2.2	Schematic diagram depicting the energy density for inhomogeneous electron gas system (left hand panel) at any location can be assigned a value from the known density variation of the exchange-correlation energy density of the homogeneous electron gas (right hand panel).	26
2.3	Schematic illustrating the a supercell model for a isolated molecule. The dashed line depicts the boundaries of the supercell.	35
2.4	Schematic representation of a psedopotential (left) and a pseudowavefunction (right) along with all-electron potential and wavefunction. The radius at which all-electron and pseudofunction values match and identical is r_c. the pseudofunctions are smooth inside the core region.	36
2.5	Schematic depicting principle of pseudopotential, of which core electrons are neglected.	36
2.6	Schematic depicting the decomposition of exact wavefunction (and energy) into three terms	38
3.1	The First Brillouin zone of a fcc lattice, with high symmetry *k*-points and direction of planes marked.	46
3.2	Flow chart of iterative methods for the diagonalization of the KS-Hamiltonian in conjunction with an iterative improvement (mixing techniques) of the charge density for the calculation of KS-ground-state.	50

3.3	Flow chart of the electronic structure simulation process of gallium arsenide clusters.	55
3.4	(a) Bulk gallium arsenide with its unit cells repeated in 3 dimensions. (b) supercells with Ga_2As_2 cluster in the center and the distance between clusters is large. The brown's colour show the Ga atoms and purple's colour show the As atoms.	56
3.5	Algorithm of geometry optimization used for large clusters.	58
3.6	Parameters for CG algorithm in INCAR file.	59
3.7	Conjugate gradient techniques: (top) Steepest descent step from $\vec{x}_0$ search for minimum along $\vec{g}_0$ by performing several trial steps to $\vec{x}_1$. (below) New gradient $\vec{g}_0 = \vec{g}(\vec{x}_1)$ is determined and $\vec{s}_1$ (green arrow) is conjugated.	60
3.8	Parameters for SA algorithm in INCAR file.	61
3.9	Flowchart illustrating the algorithm of SA.	64
3.10	Parameters for geometry optimization in KPOINTS file.	65
3.11	Parameters for self-consistent run in INCAR file.	66
3.12	Parameters for non-selfconsistent run in INCAR file.	67
3.13	Parameters for non-selfconsistent run in KPOINTS file.	68
4.1	(Left) Structure of zinc blende bulk gallium arsenide; (Right) Structure of Ga_1As_1 dimer.	70
4.2	Bandstructure of bulk gallium arsenide.	71
4.3	DOS of bulk gallium arsenide	72
4.4	Ball and stick model for hydrogenated gallium arsenide clusters.	74
4.5	Bandstructrue and DOS of hydrogenated gallium arsenide clusters, $Ga_xAs_yH_z$.	76
4.6	Band shift related to the cluster size. The upper line is HOMO energy value while lower line is LUMO energy value.	77

4.7	Lowest energy geometries for the Ga_xAs_y ($x + y \leq 15$).	81
4.8	DOS and bandstructure of Ga_1As_1 cluster.	88
4.9	DOS and bandstructure of Ga_1As_2 cluster	88
4.10	DOS and bandstructure of Ga_2As_2 cluster	89
4.11	DOS and bandstructure of Ga_2As_3 cluster	89
4.12	DOS and bandstructure of Ga_3As_3 cluster	90
4.13	DOS and bandstructure of Ga_3As_4 cluster	90
4.14	DOS and bandstructure of Ga_4As_4 cluster	91
4.15	DOS and bandstructure of Ga_4As_5 cluster	91
4.16	DOS and bandstructure of Ga_5As_5 cluster	92
4.17	DOS and bandstructure of Ga_5As_6 cluster	92
4.18	DOS and bandstructure of Ga_6As_6 cluster	93
4.19	DOS and bandstructure of Ga_7As_6 cluster	93
4.20	DOS and bandstructure of Ga_7As_7 cluster	94
4.21	DOS and bandstructure of Ga_7As_8 cluster	94
4.22	Graph of bandgap versus number of gallium arsenide atom in the cluster.	95
4.23	Graph of binding energy per atom of gallium arsenide clusters.	96

4.24	Graph of second-difference enegies and electron affinity of each gallium arsenide cluster, Ga_xAs_y $(x + y \leq 15)$ corresponding to the table above.	97
5.1	Graph of total time used for completing a parallel calculation versus the number of CPU.	111
5.2	Graph of speedup and efficiency vs number of CPU.	112

LIST OF ABBREVIATIONS

ATLAS	-	Automatically Tuned Linear Algebra Software
BLAS	-	Basic Linear Algebra Subprograms
BO	-	Born Oppenheimer
BP	-	Becke-Perdew
BSSE	-	Basis set superposition error
CC	-	Coupled cluster theory
CG	-	Conjugate gradient
CI	-	Configuration Interaction
CMS	-	Computational materials science
DFT	-	Density functional theory
DOS	-	Density of states
ETB	-	Empirical tight binding
EPM	-	Empirical pseudopotential method
EMA	-	Effective mass approximation
FFT	-	Fast-fourier transform
GEA	-	Gradient expansion approximation
GGA	-	Generalized gradient approximation
GTO	-	Gaussian-type orbital
GVB	-	Generalized valence bond
HF	-	Hartree Fock theorem
HK	-	Hohenberg-Kohn
HOMO	-	Highest Occupied Molecular Orbital
HPC	-	High-performance cluster

IFC	-	Intel Fortran Compiler
Intel® MKL	-	Intel Math Kernel Library
KS	-	Kohn-Sham theorem
LCAO	-	Linear combination of atomic orbitals
LDA	-	Local density approximation
LAPACK	-	Linear Algebra PACKage
LM	-	Langreth-Mehl
LSDA	-	Local spin density approximation
LUMO	-	Lowest Unoccupied Molecular Orbital
LYP	-	Lee-Yang-Parr
MCSCF	-	Multi-Configurations Self Consistent Field
MD	-	Molecular dynamics
MGGA	-	Meta-Generalized Gradient Approximation
MPI	-	Message Passing Interface
NC-PP	-	Norm-conserving pseudopotential
NFS	-	Network file system
PAW	-	Projected Augmented Wave
PBE	-	Perdew-Burke-Ernzernhof
PES	-	Potential energy surfaces
PP	-	Pseudopotential
PW	-	Plane Wave
PW91	-	Perdew-Wang 1991
RMM	-	Residual minimization scheme
rPBE	-	Revised-Perdew-Burke-Ernzernhof
RPA	-	Random phase approximation
SA	-	Simulated annealing
SCF	-	Self-consistent functional
SSH	-	Secure Shell
SET	-	Single-electron transistor
STO	-	Slater-type orbitals

US-PP	-	Ultrasoft Vanderbilt pseudopotential
VASP	-	Vienna Ab-Initio Software Package
VWN	-	Vosko-Wilk-Nusair
QMC	-	Quantum Monte Carlo
WF	-	Wavefunction

LIST OF SYMBOLS

E	-	Energy
E_F	-	Fermi Energy
E_g	-	Energy gap / bandgap
E_{XC}	-	Exchange-correlation energy
$f(E)$	-	Fermi energy
F	-	Force
$g(E)$	-	Density of states
g	-	Spin-scaling factor
G	-	Reciprocal lattice vector
$\hbar$	-	Planck's constant
h	-	Dirac constant
H	-	Hamiltonian
$J[n]$	-	Coulomb interaction
k	-	Wavenumber
k_B	-	Boltzmann's constant
L	-	Edge length
$\hat{L}$	-	Angular momentum operator
m	-	Mass
n	-	Quantum number of state (integer)
N	-	Number of electron
$n(\vec{r})$	-	Electron density
p	-	Momentum
$\hat{p}_r$	-	Linear momentum operator

$\widetilde{p}_{lm\varepsilon}$	-	Projector function
r, $\vec{r}$	-	Position vector
r_i	-	Electron spatial coordinates
r_s	-	Wigner-Seitz radius
$R_{nl}(r)$	-	Radial wavefunction
R	-	Radius
R_A	-	Nuclei spatial coordinates
s, t	-	Dimensionless density gradient
t	-	time
T_o	-	Kinetic energy
T	-	Temperature
u_k	-	Bloch function
U	-	Potential Energy
V	-	Volume
$Y_l^m(\theta,\varphi)$	-	Spherical harmonic
Z_A	-	Nuclei charge
λ	-	Wavelength
$^2\Delta$	-	Second-order difference energy
Ψ	-	Wavefunction
υ	-	Velocity
ω	-	Angular frequency
ν	-	Frequency
$\phi(r)$	-	Envelope function
Θ	-	Unit step function
ε	-	Energy
ε_i	-	Single-particle energy level
μ	-	Chemical potential
∇	-	Laplacian operator
ξ	-	Spin-polarization
$\tau(\vec{r})$	-	Kinetic energy density

Ω	-	Volume of unit cell
η	-	Voltage division factor
ρ	-	Density matrix
Ga	-	Gallium
As	-	Arsenide
Ga_xAs_y	-	Gallium arsenide cluster with x,y atom
$Ga_xAs_yH_z$	-	Hydrogenated gallium arsenide cluster with x,y atom and z hydrogen atom
S_N	-	Speedup
E_N	-	Efficiency

LIST OF APPENDICES

APPENDIX	TITLE	PAGE
A	Parallelization of VASP	113

CHAPTER 1

INTRODUCTION

1.1 Background of Research

In recent years, the structure and properties of microclusters of pure and compound semiconductors have received much attention and have been the subject of great interest both for experimental and theoretical studies. The structure and electronic properties of clusters can be dramatically different from those of the bulk due to the high surface area to volume ratio. The addition of a few atoms to a cluster can also result in major structural rearrangement [1].

Studies of clusters become important also because bulk and surface effects can be modeled using only a few atoms or a supercell of a typical cluster size. Moreover, with the rapid advancement in science and technology, electronic devices have been reduced in size and the behavior of semiconductor surface properties has thus gained more attention. The relation between the geometry and the electronic structure plays a critical role in dictating the properties of a material.

In the case of semiconductors, this evolution is remarkable. Semiconductor clusters have been shown to exhibit exotic properties quite different from those in molecules and solids. Compared to homogeneous clusters such as carbon and silicon, heterogeneous semiconductor clusters like gallium arsenide are more attractive because their properties can be controlled by changing the composition, in addition to the size. For these reasons, theoretical studies on clusters are critical to the design and synthesis of advanced materials with desired optical, electronic, and chemical properties.

However, theoretical studies of heterogeneous semiconductor clusters have been limited due to computational difficulties arising from the large number of structural and permutational isomers formed due to multiple elements. On one hand, sophisticated computational method such as self-consistent quantum mechanical calculation is required to make reliable prediction on the properties of these clusters, in the absence of comprehensive experimental results. On the other hand, the amount of computational work is enormous in order to find all the stable isomers for a given cluster size and composition. A number of theoretical and experimental attempts [2-14] have been made to determine the structure and properties of small Ga_xAs_y clusters. Most of the theoretical studies have been focused on clusters of a few atoms due to the above mentioned difficulties.

1.2 Atomic and Molecular Clusters

Study of physical and chemical properties of clusters is one of the most active and emerging frontiers in physics, chemistry and material science. In the last decade or so, there has been a substantial progress in generation, characterization and understanding of clusters. Clusters of varying sizes, ranging from a few angstroms to nanometers, can be generated using a variety of techniques such as sputtering, chemical vapor deposition, laser vaporization, supersonic molecular beam etc. Their

electronic, magnetic, optical and chemical properties are found to be very different from their bulk form and depend sensitively on their size, shape and composition.

Thus, clusters form a class of materials different from the bulk and isolated atoms/molecules. Looking at the mass distribution of clusters, some are found to be much more abundant than others. These clusters are therefore more stable and are called magic clusters. They act like superatoms and can be used as building blocks or basis to form a cluster assembled solid. It is these kinds of developments that add new frontiers to material science and offer possibilities of designing new materials with desirable properties by assembling suitably chosen clusters. The Table 1 show the schematic classification of clusters according to the number N of atoms.

Table 1.1: Schematic classification of clusters according to the number N of atoms.

Observable	**Very small clusters**	**Small clusters**	**Large clusters**
Number of atoms N	$2 \leq N \leq 20$	$20 \leq N \leq 500$	$500 \leq N \leq 10^7$
Diameter d	$d \leq 1$ nm	1 nm $\leq d \leq$ 3 nm	3 nm $\leq d \leq$ 100 nm
Surface fraction f	undefined	$0.5 < f < 0.9$	$f \leq 0.5$

It should be recognized that if we are to harness full technological potential of clusters, we have to gain a fundamental scientific understanding of them. This involves, for example, understanding why clusters are different from atoms and bulk, what is their geometry and structure and how it evolves with size, the evolution of their electronic, optical, magnetic and chemical properties with size and the high stability of some clusters.

Such an understanding will teach us how we can modify the cluster structure to get a desired property. These are difficult research problems because clusters are

species in their own right and do not fall into the field of atoms or solid state. Thus many techniques of atomic or solid state physics are just not applicable to clusters. New techniques of applying quantum mechanics have to be developed to handle clusters. Similarly, thermodynamics of clusters is of great importance. Many thermodynamical relationships which are derived for the bulk form are not applicable to clusters. Thus one requires new approaches to concepts of melting, freezing and phase changes in dealing with finite clusters and their dependence on size. An understanding of these concepts is important for developing technologies based on clusters.

Since many cluster properties such as geometry and structure of a cluster are not directly measurable from experiments, theoretical models and computation play an important role in the study of clusters. In this respect, the Density Functional Theory (DFT) which is designed to handle a large number of electrons quantum mechanically, has been found to be extremely useful. Using this theory one can calculate very accurately the total energy and other properties of a many electron system in its ground state (ground state energy is the lowest energy of a system; lately, the DFT has also been developed to calculate excited states).

1.3 Applications of Clusters

Clusters are an important state of matter, consisting of aggregates of atoms and molecules that are small enough not to have the same properties as the bulk liquid or solid. Quantum states in clusters are size-dependent, leading to new electronic, optical, and magnetic properties. Clusters offer attractive possibilities for innovative technological applications in ever smaller devices, and the ability to "tune" properties, especially in semiconductors, may produce novel electronic and magnetic capabilities.

Semiconductors are one of the most active areas of cluster research. Many of their properties are very dependent on size; for example, optical transitions can be tuned simply by changing the size of the clusters. Alivisatos [15] describes current research on semiconductor clusters consisting of hundreds to thousands of atoms--"quantum dots." These dots can be joined together in complex assemblies. Because of the highly specific interactions that take place between them, a "periodic table" of quantum dots is envisioned. Such coupled quantum dots have potential applications in electronic devices.

The magnetic properties of clusters are of fundamental interest and also offer promise for magnetic information storage. Shi *et al*. [16] describe recent developments in the study of magnetic clusters, both isolated and embedded in a host material. Such clusters can behave like paramagnets with a very large net moment--superparamagnets. Superparamagnetic particles can be embedded in a metal and show dramatic field changes in electrical conduction. Ion implantation has generated ferromagnetic clusters embedded in a semiconductor host, which can be switched individually.

The constituents of clusters can be arranged in many different ways: Their multidimensional potential energy surfaces have many minima. Finding the global minimum can be a daunting task, to say nothing of characterizing the transition states that connect these minima. Wales [17] describes the fundamental role of the potential energy surface in the understanding of the structure, thermodynamics, and dynamics of clusters. In a Report accompanying the special section, Ball *et al*. [18] analyze Ar_{19} and $(KCl)_{32}$ clusters and illustrate how potential energy surface topography (the sequences of minima and saddles) governs the tendency of a system to form either amorphous or regular structures.

Water is essential to life and to a great number of chemical processes. Hydrogen bonding, the source of many of water's most interesting properties, requires at least two water molecules. Far-infrared laser vibration-rotation tunneling

experiments on supersonically cooled small clusters allow characterization of geometric structures and low-energy tunneling pathways for rearrangement of the hydrogen bond networks. Liu *et al.* [19] describe how these and other recent experiments on water clusters give insight into fundamental properties of water.

Simple aggregates of carbon atoms, especially C_{60}, are remarkably stable. Determination of their actual physical and electronic structures is a formidable task because of the large number of electrons and the many possible isomeric arrangements involved. Scuseria [20] reviews the status of the field, including recent advances and current challenges in ab initio algorithms.

1.4 Introduction to Modeling and Simulation

Modeling is the technique of representing a real-word system or phenomenon with a set of mathematical equations or physical model. A computer simulation then attempts to use the models on a computer so that it can be studied to see how the system works. Prediction may be made about the behavior and performance of the system by changing its variables. In this research, nanostructures are the system targets of the modeling and simulation.

Simulation is a useful and important part of modeling nanostructures to gain insight into the attributes of a structure or a whole system with several structures connected. It is a method to predict the behavior transformation for a variable changing before performing a practical experiment. The simulation can then be proven by the results of experiment. This is also a beneficial approach to test the most optimal and the best performance of a device which is built by those nanostructures before the real fabrication.

Besides, simulation can give detailed theoretical explanation to the phenomenon that could not be solely explained by experiment . Among the examples are the reconstruction of the small cluster structures and the occupation of the electrons. With the 3D graphical viewer and animation, we can view the atomic structure models and the process of the structure transformation. With computer simulation done prior to experiment, the mastering of the small cluster structures principles is improved and 'trial and error' could be reduced during experiment.

However, there isn't a comprehensive simulator which can take into account every factor that would contribute to the system changes. Many of those only adopt the approximation which is the most optimal and closest to the real system for the representation. For nanostructures, first principle calculation is an appropriate simulation approach for studying the electronic structures and properties. The advantage of this calculation is that, it can be done without any experimental data. However, it could be a massive calculation that consumes a very long time to accomplish.

Computational science becomes an essential tool in modeling and simulation. It is the application of computational and numerical technique to solve large and complex problem, for example, complex mathematics that involved a large number of calculations. Therefore, modeling and simulation are commonly accomplished by the aid of computational science and therefore they are always referred to computer modeling and computer simulation. Computational science could be defined as an interdisciplinary approach that uses concepts and skills from the science, computer science and mathematic disciplines to solve complex problems which allow the study of various phenomena. It can be illustrated by Figure 1.1. To improve the performance and speed of large computation, one of the approaches is parallel computing. Parallel computing can reduce the computing time of computational costly calculations such as first principle calculations mentioned above, where it distributes the calculation to two or more processors or computers.

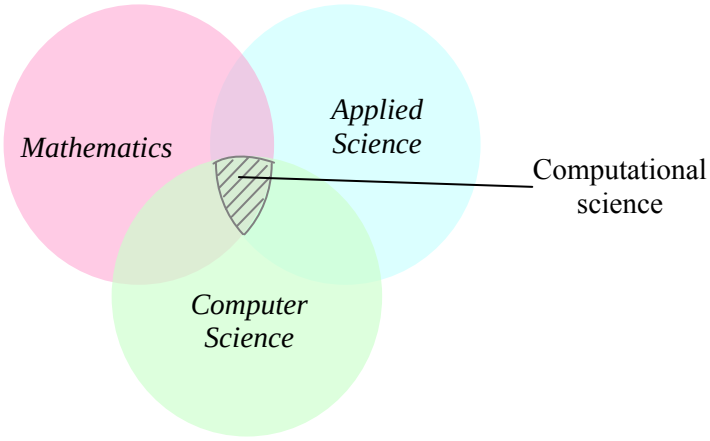

Figure 1.1: Computational science is defined as the intersection of the three disciplines, i.e. computer science, mathematics and applied science.

1.4.1 Modeling and Simulation Approach Used in This Research

In this research, Vienna Ab-initio Simulation Package (VASP) is used as the simulation tools for electronic structures of the gallium arsenide clusters. VASP is the leading density functional code to accurately compute structural, energetical, electronic and magnetic properties for a wide range of materials including solids and molecules. VASP is highly efficient for structural optimizations and ab-initio molecular dynamics (MD). It covers all elements of the periodic table of practical interest. With its projector-augmented-wave (PAW) potentials, VASP combines the accuracy of all electron methods with the elegance and computational efficiency of plane wave approaches.

1.5 Research Objectives

The main interest of this research is to study the electronic structures of gallium arsenide clusters. The objectives of this research can be summarized as the following:

a) to study the electronic structures of gallium arsenide clusters with variable size and structures.

b) to study the relation between the bandgap and the structures size of the gallium arsenide clusters.

1.6 Scopes of Study

The scopes of this research are as the following:

a) Clusters is simulated as isolated small range nanocluster.

b) Gallium arsenide is adopted as the material of the clusters.

c) Bandstructures and energy spectrum are studied for the electronic structures of gallium arsenide clusters.

d) Density functional theory is used to calculate and simulate the electronic structures of gallium arsenide clusters.

1.7 Outline of Thesis

A general background of study and brief introduction to clusters are discussed in Chapter 1. This is followed by introduction of modeling and simulation, objective and scope of study. There are a lot of approaches to simulate the electronic structures of gallium arsenide clusters. Density functional theory (DFT) is a sufficient method in doing this. Its theory is discussed in the Chapter 2. The methodology of the simulation VASP which is utilized in this study is introduced in Chapter 3. Following this, Chapter 4 would be results and discussion. Figures and graphs of the electronic structures of gallium arsenide clusters are showed and the results are discussed and interpreted. Finally Chapter 5 which is the conclusion. Theories and results discussed in the previous chapters are summarized and concluded here. Furthermore, suggestion is given on how to make the simulation better and more complete.

CHAPTER 2

COMPUTATIONAL METHOD

Electronic structure and stability of gallium arsenide clusters were investigated in detail by several theoretical studies based on Hartree-Fock (HF) [21,22], density functional theory (DFT) [6,23], configuration interaction theory (CI) [24,25] and the ab initio molecular dynamics Car-Parrinello method [5]. For this research, gallium arsenide clusters Ga_xAs_y ($x+y \leq 15$) are investigated using the density functional theory. Density functional theory is the computational method used in the simulation tool. This chapter gives a basic understanding on the relevant theorem used, although it had been well developed for the simulation tool. The next chapter will describe the simulation tool itself.

2.1 Computational Materials Science (CMS)

Computational materials science (CMS) is an interdisciplinary research area of physics, chemistry and scientific computing [26]. It can bring a microscopic understanding of the interrelationship between structure, composition, and various materials properties through classical and quantum mechanical modeling. As discussed above, we are dealing with quantum theory when the structures are in

nano-scale. Therefore, solution of Schrödinger equation, which model molecules in mathematics, brings understanding of the properties of nanostructures. By using Schrödinger equation, one can implement the following tasks:

i. electronic structure determinations
ii. geometry optimizations
iii. electron and charge distributions
iv. frequency calculations
v. transition structures
vi. potential energy surfaces (PES)
vii. chemical reaction rate constants
viii. thermodynamic calculations e.g. heat of reactions, energy of activation

Theoretical techniques of CMS with regards to Schrödinger equation can be generally categorized into three methods: molecular mechanics, semi-empirical or empirical, and ab-initio methods.

Molecular mechanics is referred to the use of Newtonian mechanics to model molecular systems. It is a mathematical formalism which produces molecular geometries, energies and other features by adjusting bond lengths, bond angles and torsion angle to equilibrium values that are dependent on the hybridization of an atom and its bonding scheme. The potential energy of the system is calculated using force field. In molecular mechanics, a group of molecules is treated as a classical collection of balls and springs rather than a quantum collection of electron and nuclei. Hence, each atom is simulated as a single particle with assigned parameters as radius, polarizability, net charge, ‘spring’ length (bond length). These parameters are generally derived from experimental data or ab-initio calculations beforehand. In many cases, large molecular systems can be modelled successfully with molecular mechanics, avoiding quantum mechanical calculations entirely.

Semi-empirical is defined as 'partly from experiment'. Semi-empirical and empirical methods are based on the Hartree Fock formalism that is simplified using empirical data derived from experimental, to make approximations and consequently to improve performance. They are important in treating large molecules where the full Hartree Fock method without approximations is too costly. Electron correlation is included in this method with the use of empirical parameters. In this method, one of the approximations is that two-electron integrals involving two-center charge distributions are neglected or parameterized and only valence shell electrons are considered. The rationale behind this approximation is that the electrons involved in chemical bonding or other phenomena are those in the valence shell. Parameterization is done to correct the loss, that the results are fitted by a set of parameters, normally in such a way as to produce results that best agree with experimental data, but sometimes to agree with ab-initio results. Empirical tight binding (ETB), empirical pseudopotential method (EPM), and k · p approximation or its equivalent form of effective mass approximation (EMA) are those among semi-empirical electronic structure methods [27]. Semi-empirical calculations are faster than their ab-initio counterpart.

The next level is ab-initio method which means 'from the beginning' in Latin. As opposed to semi-empirical, ab-initio do not include any empirical or semi-empirical in their equation but being derived directly from theoretical principles without inclusion of experimental data. It could be also known as first principle. This does not imply that Schrödinger equation have to be solved exactly, but reasonable approximation to its solution is made by choosing a suitable method and a basis set that will implement that method in a reasonable way is selected. Usually the approximations made are mathematical approximations. The time-dependent, non-relativistic Schrödinger equation can be written as

$$H\psi(r_i, R_A) = E\psi(r_i, R_A) \quad , \tag{2.1}$$

where H is the Hamiltonian operator with the total energy E as eigenvalue and many-wavefunction $\psi(r_i, R_A)$ as eigenfunction with r_i is electron spatial coordinates and R_A

is nuclei spatial coordinates [28]. The Hamiltonian operator with N electrons and M nuclei in atomic unit ($m_e = e = \hbar = 1$) is given by

$$H = -\frac{1}{2}\sum_{i=1}^{N}\nabla_i^2 - \frac{1}{2}\sum_{A=1}^{M}\frac{1}{m_A}\nabla_A^2 - \sum_{i=1}^{N}\sum_{A=1}^{M}\frac{Z_A}{r_{iA}} + \sum_{i=1}^{N}\sum_{j>i}^{N}\frac{1}{r_{ij}} + \sum_{A=1}^{M}\sum_{B>A}^{M}\frac{Z_A Z_B}{R_{AB}} \quad . \qquad (2.2)$$

Indices i and j run over N electrons while A and B over the M nuclei. ∇^2 is the Laplacian operator acting on particle, m_A is the mass of nuclei A and Z_A is its nucleus charge, r_{ij} is the distance between particle i and j which is equal to $| r_i - r_j |$, and same to $r_{iA.}$ The first term in equation (2.2) is the operator for the kinetic energy of the electrons; the second term is the operator for the kinetic energy of the nuclei; the third term represents the coulomb attraction between electrons and nuclei; the fourth term represents the repulsion between electrons and the last term represents repulsion between nuclei [29]. The wavefunction ψ is then a function of $(3N+3M)$ spatial coordinates for a system containing N electrons and M nuclei. This is a very complicated problem that is impossible to be solved exactly. The first step in simplifying this problem is the Born Oppenheimer (BO) approximation. Since the nuclei are much heavier than electrons, they move more slowly. Hence, a good approximation can be made by considering the electrons in a molecule to be moving in the field of fixed nuclei [29]. As a result, the second term of equation (2.2) can be neglected and the last term can be considered to be a constant which has no effect on the operator eigenfunctions. Then the remaining terms are called the electronic Hamiltonian which is given by

$$H_{elec} = -\frac{1}{2}\sum_{i=1}^{N}\nabla_i^2 - \sum_{i=1}^{N}\sum_{A=1}^{M}\frac{Z_A}{r_{iA}} + \sum_{i=1}^{N}\sum_{j>i}^{N}\frac{1}{r_{ij}} \quad . \qquad (2.3)$$

Although BO simplifies the original Schrödinger, the electronic part is still a daunting task to be solved exactly for systems with more than a few electrons and further approximation must be introduced. One fundamental approach is the Hartree Fock (HF) scheme, in which the principal approximation is called the central field approximation which means the Coulombic electron-electron repulsion is not specifically taken into account. Only its net effect is included in the calculation. As a result, the energies from HF calculation are always greater than the exact energy and tend to a limiting value called Hartree Fock limit. Post-Hartree-Fock methods which

are used by many calculations, begin with a Hartree-Fock calculation and subsequently correct for electron-electron repulsion, referred to also as electronic correlation. Some of these methods are Møller-Plesset perturbation theory (MPn, where n is the order of correction), the Generalized Valence Bond (GVB) method, Multi-Configurations Self Consistent Field (MCSCF), Configuration Interaction (CI) and Coupled Cluster theory (CC). Other important formalism which treats the correlation energy is Density Functional Theory (DFT) which has become popular in last two decades. In this method, energy is expressed as a function of total electron density. DFT is selected as the method of electronic structure in this research. It will be explained in more detailed in the following. Another method of ab-initio is Quantum Monte Carlo (QMC) which avoids making the HF mistakes in the first place. QMC methods work with an explicitly correlated wave function and evaluate integrals numerically using a Monte Carlo integration. Although these calculations can be very time consuming, they are probably the most accurate methods known today. As these methods are pushed to the limit, they approach the exact solution of the non-relativistic Schrödinger equation. Relativistic and spin-orbit term should be included to obtain exact agreement with experiment.

In HF, each molecular orbital is expanded in terms of a set of basis functions which are normally centered on the atoms in the molecule, as given by LCAO equation. The basis functions collectively are the basis set. Ab-initio is a method of calculation involves a choice of method and a choice of basis set. It offers a level of accuracy one needs to understand most physical properties of various materials. However in comparison with semi-empirical or empirical method, the high degree of accuracy and reliability of ab-initio calculation is compensated by large computational demand. In this method, the total molecular energy can be evaluated as a function of the molecular geometry, or in other words the potential energy surface.

2.2 Density Functional Theory

Density Functional Theory (DFT) is among the most popular and versatile methods in condensed matter physics or computational physics as well as computational chemistry. It is a quantum mechanical method that is widely used to investigate the electronic structure of many-body systems, particularly molecules and condensed phases. The contribution of DFT was given a great assurance with the award of the 1998 Nobel Prize in Chemistry to Walter Kohn and John Pople. DFT has been applied most of all to systems of electrons like atoms, molecules, clusters, homogenous solids, surfaces and interfaces, quantum wells, quantum dots and others [30]. It includes a significant fraction of the electron correlation for about the same cost of doing a HF calculation. Strictly speaking, DFT is neither a HF method nor post-HF method. The wavefunctions for spin and spatial parts are constructed in a different way from those in HF and the induced orbitals are often referred to as 'Kohn-Sham' orbitals. Nonetheless, the same procedure of SCF is used as in HF theory.

The main objective of density functional theory is to replace the many-body electronic wavefunction with the electronic density as the basic quantity. The many body Schrodinger equation is similar to equation (2.1) but can be more explicitly shown by

$$H\,\psi(\vec{r}_1,\vec{r}_2,\cdots\vec{r}_N) = E\,\psi(\vec{r}_1,\vec{r}_2,\cdots\vec{r}_N) \tag{2.4}$$

The particle density which is the key variable in DFT is given by

$$n(\vec{r}) = N\int d^3r_2\int d^3r_3\cdots\int d^3r_N\,\psi^*(\vec{r}_1,\vec{r}_2,\cdots,\vec{r}_N)\psi(\vec{r}_1,\vec{r}_2,\cdots,\vec{r}_N) \tag{2.5}$$

The electron density only depends on 3 instead of 3N spatial coordinates, but still contains all the information needed to determine the Hamiltonian, for example number of electron N, the coordinate of nuclei R_A and the charge of nuclei Z_A. This is the advantage of electron density compared to wavefunction. N is simply given by the integral over $n(\vec{r})$:

$$\int n(\vec{r})d^3r = N \tag{2.6}$$

2.2.1 Development of Density Functional Theory

The very first attempt to use electron density $n(\vec{r})$ to calculate its total energy is the Thomas-Fermi theory formulated by Thomas and Fermi in 1927 [31,32]. They calculated the energy of an atom by representing its kinetic energy as a functional of the electron density, combining this with the classical expression for the nuclear-electron and electron-electron interactions. Thus, Thomas-Fermi model is the predecessor to density functional theory. However, Thomas-Fermi model is not very accurate since there is no exchange or correlation included, and also the Thomas-Fermi kinetic energy functional is only a crude approximation to the actual kinetic energy. Hohenberg-Kohn justified in 1964 the use of electron density as basic variable in determining total energy. They gave a firm theoretical footing to DFT with two remarkable powerful theorems. The first Hohenberg-Kohn theorem proved that the relation expressed in equation (2.5) can be reversed, in which the ground state wavefunction $\psi_o(\vec{r}_1,\vec{r}_2,\cdots\vec{r}_N)$ can be calculated by a given ground state density $n_o(\vec{r})$ with a unique functional as shown below :

$$\psi_o = \psi_o[n_o] \tag{2.7}$$

It shows that there exists the one-to-one mapping between ground state electron densities and external potentials. Therefore, ground state energy is given by

$$E_o = E[n_o] = \langle \psi_o[n_o] | H | \psi_o[n_o] \rangle \tag{2.8}$$

By substituting equation (2.3), we may represent the energy as:

$$E[n(\vec{r})] = \int n(\vec{r}) V_{ext}(\vec{r}) d^3r + \left(T_e[n(\vec{r})] + V_{e-e}[n(\vec{r})]\right) \tag{2.9}$$

where $V_{ext}(\vec{r})$ is equal to the interaction of the electrons with the nuclei $V_{N\text{-}e}$ and it is non-universal, while $F_{HK}[n] = T_e[n] + V_{e-e}[n]$ is the Hohenberg-Kohn functional which does not depend on external potential and is therefore universal. The minimization of the energy functional shown in equation (2.9) will yield ground state density n_o and thus all other ground state observables. The exact form of $F_{HK}[n]$ has not been found and thus approximation must be used for the variational principle that was introduced in the second Hohenberg-Kohn theorem. The variational problem of

minimizing the energy functional $E[n]$ can be solved by applying the Lagrangian method of underdetermined multipliers, which was done by Kohn-Sham.

2.2.2 Kohn-Sham Theory

In year 1965 which is a year after the Hohenberg-Kohn theorem was published, Kohn and Sham proposed a method to obtain an exact, single-particle like, description of a many body system by approximation of universal HK functional F_{HK}. Kohn and Sham separate F_{HK} into three parts so that $E[n(\vec{r})]$ becomes

$$F[n] = T_0[n] + J[n] + E_{XC}[n] \tag{2.10}$$

$$E[n(\vec{r})] = T_0[n(\vec{r})] + \frac{1}{2}\iint \frac{n(\vec{r})n(\vec{r}')}{|\vec{r}-\vec{r}'|} d^3r\, d^3r' + E_{XC}[n(\vec{r})] + \int n(\vec{r}) V_{ext}(\vec{r}) d^3r \tag{2.11}$$

where $T_0[n(\vec{r})]$ is the kinetic energy of the non-interacting electron gas with density $n(\vec{r})$, the second term is the Hartree potential which describes coulomb interaction between electrons, $E_{XC}[n(\vec{r})]$ is the exchange-correlation energy. $T_0[n]$ is calculated in terms of the $\phi_i(\vec{r})$'s

$$T_0[n(\vec{r})] = \sum_i \int \phi_i^*(\vec{r}) \left(-\frac{1}{2}\nabla^2 \right) \phi_i(\vec{r}) d^3r \tag{2.12}$$

Though $T_0[n]$ is not the exact kinetic energy, it is well defined and is treated exactly in this method. This eliminates some of the shortcomings of the Thomas-Fermi approximation to the Fermion system, for instances the lack of shell effects or absence of the bonding in molecules and solids. In equation (2.11), $E_{XC}[n(\vec{r})]$ is the only term can not be treated exactly and thus it is the only term concerned in the approximation of that equation. By applying variational principle, equation (2.11) can be written in terms of an effective potential, $V_{eff}(\vec{r})$ as follow:

$$\frac{\delta T_0[n(\vec{r})]}{\delta n(\vec{r})} + V_{eff}(\vec{r}) = \mu \tag{2.13}$$

where $$V_{eff}(\vec{r}) = V_{ext}(\vec{r}) + \int \frac{n(\vec{r}')}{|\vec{r} - \vec{r}'|} d^3 r' + \mu_{XC}[n(\vec{r})] \tag{2.14}$$

and $$\mu_{XC}[n(\vec{r})] = \frac{\delta E_{XC}[n(\vec{r})]}{\delta n(\vec{r})} \tag{2.15}$$

μ is the Lagrange multiplier related to the conservation of N and $V_{eff}(\vec{r})$ is called Kohn-Sham (KS) effective potential. If one consider a system that contains non-interacting electrons that is without any two-body interaction, moving in an external potential $V_{eff}(\vec{r})$ as defined in equation (2.14), then the same analysis will lead to the exactly same equation (2.13). Solution of equation (2.13) can be found by solving single-particle equation for the non-interacting particles (KS equation):

$$\left(-\frac{\nabla^2}{2} + V_{eff}(\vec{r}) \right) \phi_i(\vec{r}) = \varepsilon_i \phi_i(\vec{r}) \tag{2.16}$$

where ε_i is the Kohn-Sham eigenvalue which is the Lagrange multipliers corresponding to the orthonormality of the N single-particle states $\phi_i(\vec{r})$ referring to the variational condition under the orthonormality constraint $\langle \phi_i | \phi_j \rangle = \delta_{ij}$ which lead to the following equation:

$$\delta \left[E[n(\vec{r})] - \sum_{i,j} \varepsilon_{ij} \left(\langle \phi_i | \phi_j \rangle - \delta_{ij} \right) \right] = 0 \tag{2.17}$$

The density is constructed from a set of one-electron orbitals or called Kohn-Sham orbitals (non-interacting reference system):

$$n(\vec{r}) = \sum_i |\phi_i(\vec{r})|^2 \tag{2.18}$$

Since the Kohn-Sham potential $V_{eff}(\vec{r})$ depends upon the density $n(\vec{r})$, equation (2.14)-(2.16) must be solved self-consistently. This can be done by making a guess for the form of the density, then Schrödinger equation is solved to obtain a set of orbitals $\{\phi_i(\vec{r})\}$ from which a new density is constructed and the process repeated until the input and output densities are the same as depicted in Figure 2.1. Practically there is no problem of converging to the ground state minimum owing to the convex nature of density functional. From this solution, ground state energy and density can be determined. Total energy is then given by:

$$E = \sum_i \varepsilon_i - \frac{1}{2} \iint \frac{n(\vec{r}) n(\vec{r}')}{|\vec{r} - \vec{r}'|} d^3 r \, d^3 r' + E_{XC}[n(\vec{r})] - \int \mu_{XC}[n(\vec{r})] n(\vec{r}) d^3 r \tag{2.19}$$

where $$\sum_i \varepsilon_i = \sum_i \langle \phi_i | -\frac{\nabla^2}{2} + V_{eff}(\vec{r}) | \phi_i \rangle = T_0[n(\vec{r})] + \int V_{eff}(\vec{r})\, n(\vec{r})\, d^3 r \qquad (2.20)$$

In the above equation, $\sum_i \varepsilon_i$ is the non-interacting system energy which given by the sum of one-electron energies and when double-counting correlations is included which double-counts the Hartree energy and over-counts the exchange-correlation energy, induces the interacting system energy *E*. The solution of equation (2.13) and (2.15) is much simpler than that of the HF equation since the effective potential is local.

KS theory succeeds to transform N-body problem into N single-body problem with each coupled to Kohn-Sham effective potential. In contrary to HF, there is no physical meaning of these single-particle Kohn-Sham eigenvalues and orbitals but are merely mathematical tools that facilitate the determination of the true ground state energy and density. In HF theory, Koopman's theorem provide a physical interpretation of orbital energies ε_i such that the orbital energy is an approximation of the negative of the ionization energy associated with the removal of an electron from orbital ϕ_i which is given by $\varepsilon_i^{HF} = E^{HF}(n_i = 1) - E^{HF}(n_i = 0) = -IE(i)$. It explains that the ionization potentials and electron affinities are approximated by the negative of the HF occupied and virtual orbital eigenvalues respectively. It assumes no relaxation of the orbitals when occupation numbers are changed. This theorem is invalid for KS orbitals in which the total energy is a nonlinear functional of the density as derived from equation (2.16).

$$\frac{\delta E[n(\vec{r})]}{\delta n_i(\vec{r})} = \varepsilon_i \qquad , \qquad n_i(\vec{r}) = \phi_i^*(\vec{r})\, \phi_i(\vec{r}) \qquad (2.21)$$

The exception is the highest occupied KS eigenvalue for which it has been shown to be the negative of the first ionization potential. Also, DFT is only variational if the exact energy functional is used, yet HF theory is variational providing an upper bound to the exact energy.

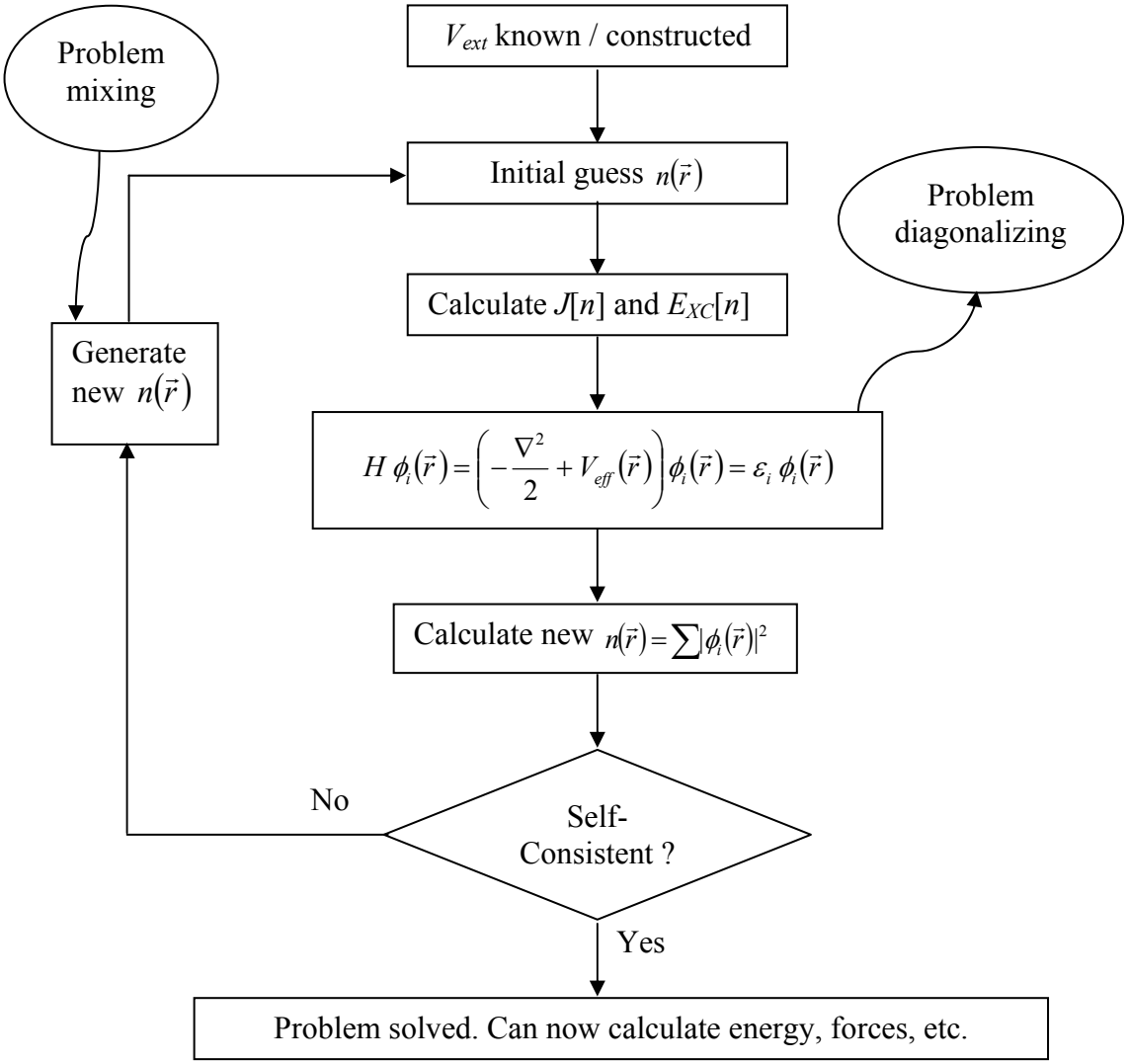

Figure 2.1: Schematic depicting self-consistent loop.

2.2.3 Self-Consistent Field (SCF)

A self-consistent field (SCF) procedure used to find approximate wave functions and energy levels in many electron atoms. This procedure was introduced by the English mathematician and physicist Douglas Hartree in 1928 and improved by the Soviet physicist Vladimir Fock in 1930 (by taking into account the Pauli exclusion principle). The initial wave functions can be taken to be hydrogenic atomic orbitals. The resulting equations can be solved numerically using a computer. The results of the Hartree-Fock theory are sufficiently accurate to show that electron density occurs in shells around atoms and can be used quantitatively to show chemical periodicity.

2.2.4 Non-Self Consistent Field

Recently there was an increased interest in the so called Harris-Foulkes (HF) functional. This functional is non- self consistent: The potential is constructed for some 'input' charge density, then the band-structure term is calculated for this fixed non- self consistent potential. Double counting corrections are calculated from the input charge density: the functional can be written as

$$E_{HF}[\rho_{in},\rho] = bandstructure\left(V_{in}^{H}+V_{in}^{xc}\right)+Tr\left[\left(-V_{in}^{H}/2-V_{in}^{xc}\right)\rho_{in}\right]+E^{\alpha c}[\rho_{in}+\rho_{c}] \quad (2.22)$$

It is interesting that the functional gives a good description of the binding-energies, equilibrium lattice constants, and bulk-modulus even for covalently bonded systems like Ge. In a test calculation we have found that the pair-correlation function of l-Sb calculated with the HF-function and the full Kohn-Sham functional differs only slightly. Nevertheless, we must point out that the computational gain in comparison

to a self consistent calculation is in many cases very small (for Sb less than 20%). The main reason why to use the HF functional is therefore to access and establish the accuracy of the HF-functional, a topic which is currently widely discussed within the community of solid state physicists. To our knowledge VASP is one of the few pseudopotential codes, which can access the validity of the HF-functional at a very basic level, for example without any additional restrictions like local basis-sets and others. Within VASP the band-structure energy is exactly evaluated using the same plane-wave basis-set and the same accuracy which is used for the self consistent calculation. The forces and the stress tensor are correct, insofar as they are an exact derivative of the Harris-Foulkes functional. During a MD or an ionic relaxation the charge density is correctly updated at each ionic step

2.2.5 Exchange-Correlation Functionals

The results so far are exact, provided that the exchange-correlation functional $E_{XC}[n(\vec{r})]$ is known. The problem of determining the functional form of the universal HK density functional F_{HK}, has now been transferred to the exchange-correlation functional of Kohn-Sham formalism, and therefore this term is not known exactly. Good approximation for $E_{XC}[n(\vec{r})]$ is still one of the challenge's aims in modern DFT.

2.2.5.1 Local Density Approximation for Exchange-Correlation Energy

The simplest approximation for exchange-correlation functional is local density approximation (LDA), which works well and most widely used. This approximation assumes that the density can be treated locally as a uniform electron gas which describes a system in which electrons move on uniform positive

background charge distribution such that overall charge neutrality is preserved. The exchange-correlation energy at each point in the system is the same as even if the inhomogeneity is large by approximating it locally with the density of homogeneous electron gas (see Figure 2.2). This approximation was firstly formulated by Kohn and Sham and holds for a slow varying density. Using this approximation, the exchange-correlation energy for a density is commonly written as

$$E_{XC}^{LDA}\left[n(\vec{r})\right] = \int n(\vec{r})\varepsilon_{XC}^{LDA}\left[n(\vec{r})\right]d^3r \tag{2.23}$$

where $\varepsilon_{XC}^{LDA}\left[n(\vec{r})\right]$ is the exchange-correlation energy density corresponding to a homogeneous electron gas with the local density $n(\vec{r})$. The energy is again can be separated into exchange and correlation contribution:

$$E_{XC}^{LDA}\left[n(\vec{r})\right] = \int n(\vec{r})\varepsilon_{X}^{LDA}\left[n(\vec{r})\right]d^3r + \int n(\vec{r})\varepsilon_{C}^{LDA}\left[n(\vec{r})\right]d^3r \tag{2.24}$$

The LDA exchange-correlation potential is yielded by the functional derivatives of equation (2.23):

$$\mu_{XC}^{LDA}(\vec{r}) = \frac{\delta E_{XC}^{LDA}\left[n(\vec{r})\right]}{\delta n(\vec{r})} = \varepsilon_{XC}^{LDA}\left[n(\vec{r})\right] + n(\vec{r})\frac{\delta \varepsilon_{XC}^{LDA}\left[n(\vec{r})\right]}{\delta n(\vec{r})} \tag{2.25}$$

The available exchange and correlation potential of LDA type are as follow:

- Dirac-Slater exchange [33].
- Vosko-Wilk-Nusair (VWN) correlation [34].
- Vosko-Wilk-Nusair (VWN) correlation within the random phase approximation (RPA) [34].
- Perdew and Zunger parametrization of the homogenous electron gas correlation energy, which is based on the quantum Monte Carlo calculations of Ceperley and Alder [35].

The exchange part of the energy per particle $\varepsilon_{X}^{LDA}\left[n(\vec{r})\right]$ is given by Dirac functional:

$$\varepsilon_{X}\left[n(\vec{r})\right] = -\frac{3}{4}\left(\frac{3}{\pi}n(\vec{r})\right)^{1/3} \tag{2.26}$$

Accurate results of correlation energy per particle $\varepsilon_{C}^{LDA}\left[n(\vec{r})\right]$ have been given by Quantum Monte Carlo (QMC) calculations of Ceperly and Alder [36] for homogenous electron gas of different densities. This is the most common correlation formula used. Other methods finding correlation is listed above. Perdew and Zunger proposed the formula:

$$\varepsilon_C^{PZ} = \begin{cases} A \ln r_s + B + C r_s \ln r_s + D r_s & r_s \le 1 \\ \gamma / \left(1 + \beta_1 \sqrt{r_s} + \beta_2 r_s\right) & r_s > 1 \end{cases} \quad (2.27)$$

where r_s is the Wigner-Seitz radius of each electron. For high-density ($r_s \le 1$), RPA is used to obtain the parameters for LDA. For intermediate regime of densities, the simplest approach to the correlation energy is an interpolation between the high- and the low limit-density. Another widely used VWN correlation is given as:

$$\frac{\varepsilon_C^{VWN}}{A} = ln\left(\frac{r_s}{F\left(\sqrt{r_s}\right)}\right) + \frac{2b}{\sqrt{4c-b^2}} tan^{-1}\left(\frac{\sqrt{4c-b^2}}{2\sqrt{r_s}+b}\right) - \frac{bx_0}{F(x_0)}\left[ln\left(\frac{\sqrt{r_s}-x_0}{F\left(\sqrt{r_s}\right)}\right) + \frac{2(b-2x_0)}{\sqrt{4c-b^2}} tan^{-1}\left(\frac{\sqrt{4c-b^2}}{\sqrt{r_s}+b}\right)\right] \quad (2.28)$$

F$(x) = x^2 + bx + c$ and other filling parameter, which varies for polarized and unpolarized conditions are obtained by the data of Ceperly and Alder.

Most of the Kohn-Sham calculations were carried out under the LDA which produces surprisingly accurate results which makes it widely used especially in solid state physics. In LDA, exact properties of exchange-correlation hole are maintained. The electron-electron interaction depends only the spherical average of exchange-correlation hole and this is reasonably well reproduced. The errors in exchange and correlation energy densities tend to cancel each other. Properties such as structure, vibrational frequencies, phase stability and elastic moduli are described reliably for many systems. However it tends to underpredict atomic ground state energies and ionisation energies, while overestimating binding energies (typically by 20-30%). Results obtained with the LDA usually become worse with the increasing inhomogeneity of the described system such as in atoms or molecules particularly. Nevertheless, the astonishing fact is that the LDA works as well as it does give the reduction of the energy functional to a simple local function of the density.

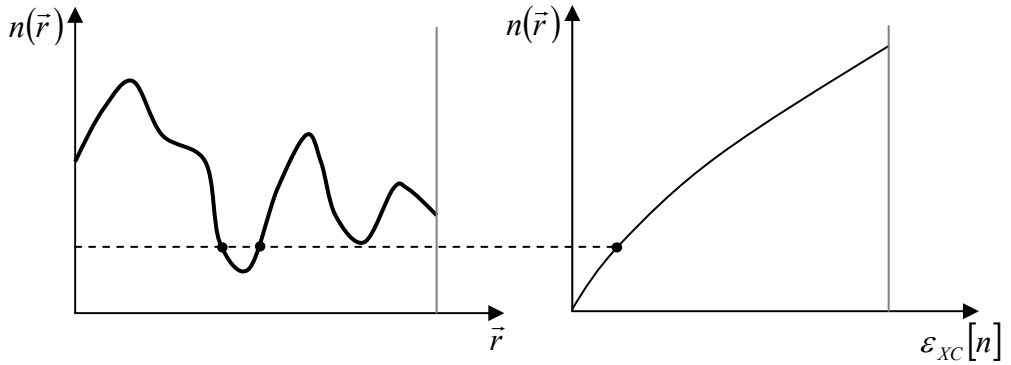

Figure 2.2: Schematic diagram depicting the energy density for inhomogeneous electron gas system (left hand panel) at any location can be assigned a value from the known density variation of the exchange-correlation energy density of the homogeneous electron gas (right hand panel).

2.2.5.2 Generalized Gradient Approximation (GGA)

As stated above, the LDA uses the exchange-correlation energy of the homogeneous electron gas at every point in the system regardless of the homogeneity of the real charge density. For nonuniform or inhomogeneous charge densities the exchange-correlation energy can deviate significantly from the homogeneous result. An improvement to this deviation is by considering the gradient of the charge density, which is utilized by Generalized Gradient Approximation (GGA). GGA was developed from gradient expansion approximation (GEA) proposed by Hohenberg and Kohn [37]. In comparison with LSDA, GGA tends to improve total energies, atomization energies, binding energies, bond length and angle [38], energy barriers and structural energy difference. Differ from the LDA which is local, GGA is semi-local functional. General semi-local approximation to the exchange-correlation energy as a functional of the density and its gradient to fulfill a maximum number of exact relations is given by:

$$E_{XC}^{GGA}\left[n^{\alpha},n^{\beta}\right]=\int f\left(n^{\alpha},n^{\beta},\nabla n^{\alpha},\nabla n^{\beta}\right)d^{3}r \qquad (2.29)$$

where f is the analytic function. There are two strategies for determining function f. The first one is known as non-empirical by adjusting f such that it satisfies all known properties of the exchange-correlation hole and energy (Perdew); and the second way is semiempirical by fitting f to a data-set containing exactly known binding energies

of atoms and molecules (Becke). Many GGA's are tailored for specific classes of problems, among those are: Langreth-Mehl 1983 (LM) [39,40], Perdew-Wang 1986 (PW86) [41,42], Becke-Perdew 1988 (BP) [43], Lee-Yang-Parr 1988 (LYP) [44], Perdew-Wang 1991 (PW91) [45,46], Perdew-Burke-Ernzernhof 1996 (PBE) [47,48], and Revised-Perdew-Burke-Ernzernhof 1999 (rPBE) [49].

One way to compare these GGA's (for spin-polarized system) is to define the exchange-correlation energy in terms of enhancement factor $F_X^{GGA}[r_s, s]$ [42] as:

$$E_{XC}^{GGA}[n^{\alpha}, n^{\beta}] = \int n(\vec{r})\varepsilon_X^{LDA}[n(\vec{r})]F[r_s(\vec{r}), \xi, s(\vec{r})]d^3r \tag{2.30}$$

where $\varepsilon_X^{LDA}[n(\vec{r})] = -3k_F/4\pi$ is the exchange energy per particle for a uniform gas of density n, which is defined by the LDA, s is a dimensionless measure of the gradient

$$s(\vec{r}) = \frac{|\nabla n(\vec{r})|}{2k_F(\vec{r})n(\vec{r})} \tag{2.31}$$

with the local Fermi wavevector defined as

$$k_F(\vec{r}) = [3\pi^2 n(\vec{r})]^{1/3} \tag{2.32}$$

and r_s is the local Wigner-Seitz radius,

$$r_s(\vec{r}) = \left[\frac{3}{4\pi n(\vec{r})}\right]^{1/3} \tag{2.33}$$

Plotting $F_X^{GGA}[r_s, s]$ against s for various r_s values allows an effective way of examining and comparing different GGA's

One GGA functional used predominantly in solid state physics is PW91. The PW91 exchange and correlation function was constructed by introducing real space cut-off the spurious long-range part of the density-gradient expansion for the exchange and correlation hole. It is one of the non-empirical constructions since it does not contain any free parameters fitted to experimental data but determined from exact quantum mechanical relations. In general GGA exchange energy can be written in the form similar to equation (2.33):

$$E_X^{GGA}[n, s] = \int n(\vec{r})\varepsilon_X^{GGA}[n(\vec{r}), s(\vec{r})]d^3r = \int n(\vec{r})\varepsilon_X^{LDA}[n(\vec{r})]F_X^{GGA}[s(\vec{r})]d^3r \tag{2.34}$$

$F_X^{GGA}[s]$ in the case of PW91 is given by:

$$F_X^{PW91}[s] = \frac{1 + 0.19645\ s\ sinh^{-1}(7.7956\,s) + \left(0.2743 - 0.15084\,e^{-100\,s^2}\right)s^2}{1 + 0.19645\ s\ sinh^{-1}(7.7956\,s) + 0.004\,s^4} \qquad (2.35)$$

which is an extension of a form given by Becke B88 [43], though it is tailored so that extra exact conditions are obeyed, for instances, the correct behaviour in the slowly varying (small *s*) limit, some scaling relations [50], and energy bounds [51]. $F_X^{GGA}[s]$ remains unchanged with different r_s values because there is no r_s dependence in the enhancement factor since the exchange energy scales linearly with uniform density scaling. GGA correlation energy can be written in the form:

$$E_C^{GGA}[n^\alpha, n^\beta] = \int n(\vec{r})\left[\varepsilon_C^{LDA}(r_s, \xi) + H(t, r_s, \xi)\right]d^3r \qquad (2.36)$$

where *t* is another dimensionless density gradient defined by:

$$t = \frac{|\nabla n(\vec{r})|}{2\,g\,k_S\,n(\vec{r})} \qquad (2.37)$$

with $k_s = [4k_F/\pi]^{1/2}$ is the TF screening wave vector and $g = \left[(1+\xi)^{2/3} + (1-\xi)^{2/3}\right]/2$ is a spin-scaling factor. For PW91, *H* is defined as:

$$\begin{aligned} H[t, r_s, \xi] = {} & g^3 \frac{\beta^2}{2\alpha} ln\left(1 + \frac{2\alpha}{\beta}\frac{t^2 + At^4}{1 + At^2 + A^2t^4}\right) \\ & + \nu\left[C_c(r_s) - C_c(0) - \frac{3}{7}C_x\right]g^3t^2e^{\left[-100\,g^4\left(k_s^2/k_F^2\right)t^2\right]} \end{aligned} \qquad (2.38)$$

where $A = (2\alpha/\beta)\left(\left[1/exp\left\{-2\alpha\varepsilon_C/\left(g^3\beta^2\right)\right\}\right] - 1\right)$; $\alpha = 0.09$; $\beta = \nu\, C_c(0) = 0.004235\ \nu \cong 0.066725$; $\nu = (16/\pi)(3\,\pi^2)^{1/3} = 15.7559$; C_x = -0.001667; $C_c(r_s) = C_{xc}(r_s) - C_x$; and $C_{xc}(r_s) = \frac{1}{1000}\frac{2.568 + 23.266r + 0.007389r^2}{1 + 8.723r + 0.472r^2 + 0.07389r^3}$.

PW91 incorporates some inhomogeneity effects while retaining many of the best features of LSDA. However, it has its own problem; for example, the parameters are not joined seamlessly giving rise to spurious wiggles in the exchange-correlation potential for small and large dimensionless density gradients, which can afflict the construction of GGA-based electron-ion pseudopotentials. The analytic function *f* fitted to the numerical results of the real-space cutoff is also complicated and nontransparent, and it has been found that known exact features of the exchange-correlation energy exist that are more important than those satisfied by the PW91. Hence, PBE which is the most popular GGA functional today has been constructed

to improved the deficiencies of PW91. PBE uses simple derivation of GGA functional in which its parameters are fundamental constants. The exchange enhancement factor of PBE is different from PW91 which is given by:

$$F_X^{PBE}(s) = 1 + \kappa - \frac{\kappa}{1 + \mu s^2 / \kappa} \tag{2.39}$$

where $\mu = \beta(\pi^2/3) = 0.21951$ and $\kappa = 0.804$ is related to the second-order gradient expansion. This form has the following properties [34,38]: (i) satisfies the uniform scaling condition, (ii) recovers the correct uniform electron gas limit because $F_x(0) = 1$, (iii) obeys the spin-scaling relationship, (iv) recovers the LSDA linear response limit for $s \to 0$ ($Fx(s) \to 1 + \mu s^2$) and (v) satifies the local Lieb-Oxford bound [51] $\varepsilon_X(r) \geq -1.479\ \rho(r)^{4/3}$, that is $F_X(s) \leq 1.804$, for all r, provided that $\kappa \leq 0.804$. The correlation energy is written similarly to equation (2.35) with H as:

$$H[t, r_s, \xi] = \left(\frac{e^2}{a_0}\right)\gamma g^3 \ln\left\{1 + \frac{\beta\gamma^2}{t}\left[\frac{1 + At^2}{1 + At^2 + A^2t^4}\right]\right\} \tag{2.40}$$

where $A = \frac{\beta}{\gamma}\left[exp\left\{-\varepsilon_C^{LDA}[n]/\left(\gamma g^3 e^2/a_0\right)\right\} - 1\right]^{-1}$; and $\gamma = (1 - ln\,2)/\pi^2 \cong 0.031091$.

Other parameters are same with those of PW91. The correlation correction term H of PBE satisfies the following properties [38,47]: (i) it tends to the correct second-order gradient expansion in the slowly varying (high-density) limit ($t \to 0$), (ii) it approaches minus of the uniform electron gas correlation $-\varepsilon_C^{LDA}$ for rapidly varying densities ($t \to \infty$), hence making the correlation energy to vanish results from the correlation hole sum rule $\int d^3u\, n(r, r+u) = 0$, for density at position $r+u$ of the correlation hole surrounding an electron at r, (iii) it cancels the logarithmic singularity of ε_C^{LDA} in the high-density limit, thus forcing the correlation energy to scale to a constant under uniform scaling of the density. PBE retains correct features of LSDA and combines them with the most energetically important features of gradient-correlation non-locality [47]. It neglect the correct but less important features of PW91 which are the correct second-order gradient coefficients for E_X and E_C in the slowly varying limit, and the correct nonuniform scaling of E_X in limits where the s tends to ∞.

2.2.6 DFT Choice of Electronic Structure

Since in the nano-size, the material properties depend to a large extent on quantum effects, it necessitates the importance of atomic scale computer simulations and requires that these simulations should include a quantum mechanical description of the electrons. The development of ab-initio DFT and its integration into user-friendly program has led to a revolution in atomic-scale computational modeling in the last two decades. These methods are today used transdisciplinarily for the investigation of metallic, minerals, semiconducting material and molecular systems, as well as nano-structured devices such as nano-structured surfaces and thin films, nano-wires and quantum-dots.

Therefore, DFT is a successful theory to electronic structure of atoms, molecules and solids. It has become the most popular method in quantum chemistry and physics, accounting for approximately 90% of all calculation today. It produces good energy and excellent structure while scaling favorably with electron number and hence it is feasible on larger systems compared to other methods. Besides, it offers notable balance between accuracy and computational cost in which it produces accurate results with relatively smaller basis sets in comparison with other method such as HF (see Table 2.1). The success of DFT is also due to its availability of increasingly accurate approximations to the exchange-correlation energy. It is able to give the quantitative understanding of materials properties from the fundamental laws of quantum mechanics. Other than these, DFT is very useful in order to understand the complicated observation of diversity such as the reaction of some materials, design new materials with desired properties, and study conditions that are impossible or expensive to be measured experimentally.

Table 2.1: Comparison of accuracy of various computation tools.

Method	Description	Accuracy
Molecular Mechanics (**MM**)	Atomistic, empirical potentials	Low
Austin Model 1 (**AM1**), Parameterized Model 3 (**PM3**)	HF with semi-empirical integrals	: :
Hartree Fock (**HF**)	Slater-determinant	:
2nd-order Møller-Plesset (**MP2**)	Simplest ab-initio correlation	:
Density Functional Theory (**DFT**)	Density based	:
Coupled-Cluster with Single and Double and Perturbative Triple excitations [**CCSD (T)**]	Harder ab-initio correlation	: :
Multi-Reference Configuration Interaction (**MRCI**)	Multi-reference	High

There are plenty of DFT codes for electronic structure calculation, for instances some of them are:

- VASP
- CASTEP
- Wien2K
- CPMD
- ABINIT
- FHImd
- Siesta

In this research, VASP is used as the dominant codes for calculating electronic structure of gallium arsenide clusters. Its introduction is given in the next chapter. Below is the list of some of the properties that can be calculated by DFT:

a) Total energy in the ground state, which is very useful quantity that can be used to get structures, heat of formation, adsorption energies, diffusion barriers, activation energies, elastic moduli, vibrational frequencies and others.

b) Forces on nuclei which can be obtained with Hellmann-Feynman Theorem [52] which is given by:

$$\vec{F}_I = -\frac{\partial E_0\left[\vec{R}\right]}{\partial \vec{R}_I} = Z_I \int_{\vec{r}} \frac{n(\vec{r})\left(\vec{r} - \vec{R}_I\right)}{|\vec{r} - \vec{R}_I|^3} d^3 r \qquad (2.41)$$

where $\vec{R}_I$ is the position of the nuclei the forces $\vec{F}_I$ acting on, and Z_I is its nucleus charge. The forces can be used to get equilibrium structures, transition states, vibrational frequanecies and others. It is also can be used in molecular dynamics to get the properties at finite temperature.

c) Eigenvalues
d) Vibrational frequencies
e) Density in the ground state
f) Magnetic properties (for example by using LSDA)
g) Ferroelectric properties (for example by using Berry's phase formulation)

2.3 Basis Set

As mentioned above, ab-initio involves the choice of method (e.g. DFT) and basis set. Basis set is a set of functions employed for representation of molecular orbitals, which are expanded as a linear combination of atomic orbitals (LCAO) with the coefficients to be determined as given by

$$\psi_i(\vec{r}) = \sum_{\mu=1}^{n} C_{\mu i}\phi_\mu(\vec{r}) \tag{2.42}$$

where ϕ_μ are elements of a complete set of functions. Typically, the basis functions are centered on the atoms, and so sometimes they are called atomic orbitals. Basis set were first developed by J. C. Slater. Thus, initially these atomic orbitals were typical Slater orbitals, which corresponding to a set of functions which decayed exponentially with distance from the nuclei. Later, it was realized that these Slater-type orbitals (STO) [53] could be in turn approximated as linear combinations of Gaussian orbitals instead, for the reason that it is easier to calculate overlap and other integrals with Gaussian basis functions [54,55], which led to huge computational savings. Today, there are hundreds of Gaussian-type orbital (GTO) basis sets. They are generally categorized into two. The first and the simplest is minimal basis sets which describes only the most basic aspects of the orbitals. Examples for these basis

sets are STO-2G, STO-3G and STO-6G, where the number before G represents the number of GTOs combined to approximate the STO. Minimal basis sets can still be used in part for other types of basis sets which are called split valence and double-zeta basis sets, which are the results of scaling the orbital to different size by splitting the minimal basis set. A few examples of common split-valence basis sets are 3-21G, 4-31G and 6-31G. The second category is extended basis sets which have much more detailed description derived from a set of mathematical functions designed to give maximum flexibility to the molecular orbitals, which subject to the costs of the calculation. The basis sets can be added with any suitable function. The important additions are polarization functions (denoted by * at the end of basis set name, e.g. 3-21G*) and diffusion functions (denoted by sign +, e.g. 3-21+g). More extensions are for instances triple valence and triple zeta basis sets. All these basis sets are of the type of localized basis sets.

2.3.1 Plane Wave Basis Sets

In addition to the localized basis set, another basis sets available for quantum chemical or physics simulations are plane wave (PW) basis sets, which are of non-localized basis set. PW basis set offers a number of advantages, including the simplicity of the basis functions, which make no preconceptions regarding the form of the solution, basis set superposition error (BSSE) is removed as all functions in the basis are mutually orthogonal, suitability for all atomic species with the same basis set, and the ability of calculate the forces on atoms efficiently due to the correction terms are not needed.

On the reason that most of the material properties of solids are determined by the valence electrons, the representation of the valence states is more important than the representation of the core states for the calculations on solids and surfaces. Therefore, pseudopotential (PP) [56] is an approximation that removes the core

electrons (see Figure 2.3 and 2.4) and thus reducing the wavefunctions need to be calculated. The use of pseudopotentials and the pseudo-valence wave functions allow the expansion of the valence wave functions in a PW basis set. In general the representation of an arbitrary orbital in terms of a PW basis set would require a continuous, and thus infinite, basis set. Nonetheless, the imposition of periodic boundary conditions allows the use of Bloch's Theorem whereby the $\tilde{\psi}_{n.\vec{k}}$ of the system with a band index *n* and wavevector $\vec{k}$, can be written as

$$\begin{aligned} \tilde{\psi}_{n,\vec{k}}(\vec{r}) &= e^{i\,k\cdot\vec{r}}\; f_{n.\vec{k}}(\vec{r}) \\ &= \frac{1}{\Omega^{1/2}} \sum_{\vec{G}} c_{\vec{G}n\vec{k}}\; exp\left[i\left(\vec{k}+\vec{G}\right)\cdot\vec{r}\right] \end{aligned} \tag{2.43}$$

where $f_{n.\vec{k}}(\vec{r}) = \frac{1}{\Omega^{1/2}} \sum_{\vec{G}} c_{\vec{G}n\vec{k}}\; e^{i\,\vec{G}\cdot r}$ is the expansion of the valence wave with Ω is the volume of the unit cell. The sum is over all reciprocal lattice vectors $\vec{G}$, and the wavevector $\vec{k}$ lies within the first Brillouin zone. A given one-electron state (basis set) for any point $\vec{k}$ can be expanded in a discrete but infinite number of plane waves. . In practice, the set of plane waves is restricted to a sphere in reciprocal space most conveniently represented in terms of a cut-off energy, E_{cut}, such that for all values of $\vec{G}$ used in the expansion is given by:

$$\frac{\hbar^2 |\vec{k}+\vec{G}|^2}{2m} \;\leq\; E_{cut} \tag{2.44}$$

The variation of a single parameter, E_{cut} may ensure the convergence of the calculation with respect to basis set. Therefore, the calculated properties often show extreme sensitivity to tiny changes in basis set and no systematic scheme for convergence is available. This is a significant advantage of PW over other basis set choices.

Bulk solid which exhibits translational symmetry possesses the natural condition of periodic boundary. In the case of isolated molecule, periodic boundary conditions must be introduced artificially by a supercell model (see Figure 2.3). In this model, there is an adequate amount of vacuum region around the molecules such that the periodic array of molecules has a large separation. By this, the results will be

those for an isolated molecule. The electron density $n(\vec{r})$ and energy are given by averaging the results for all values of $\vec{k}$ in the first Brillouin zone (BZ),

$$n(\vec{r}) = \frac{1}{V_{BZ}} \int_{1st\,BZ} \tilde{n}_{\vec{k}}(\vec{r}) d^3k \tag{2.45}$$

where

$$\tilde{n}_k(\vec{r}) = \sum_{i=1}^{N} |\tilde{\psi}_{n,\vec{k}}(\vec{r})|^2 \tag{2.46}$$

and

$$E = \frac{1}{V_{BZ}} \int_{1st\,BZ} E(\vec{k}) d^3k \tag{2.47}$$

In an infinite system, these integrals are replaced by weighted sums over a discrete set of **k**-points which must be selected carefully to ensure convergence of the results. Nevertheless an isolated molecule will exhibit no dispersion where there will be no variation of E and $n(\vec{r})$ with **k**. Therefore, isolated molecule calculations need only a single **k**-point.

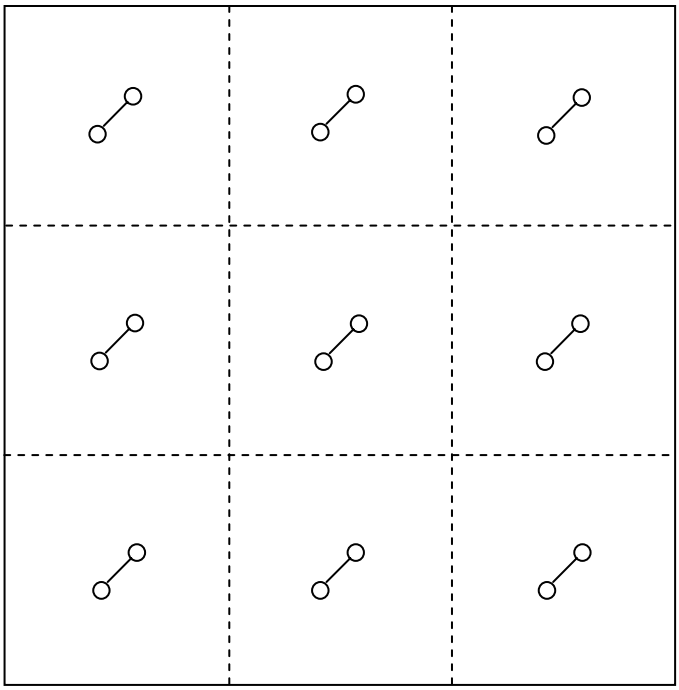

Figure 2.3: Schematic illustrating the a supercell model for a isolated molecule. The dashed line depicts the boundaries of the supercell.

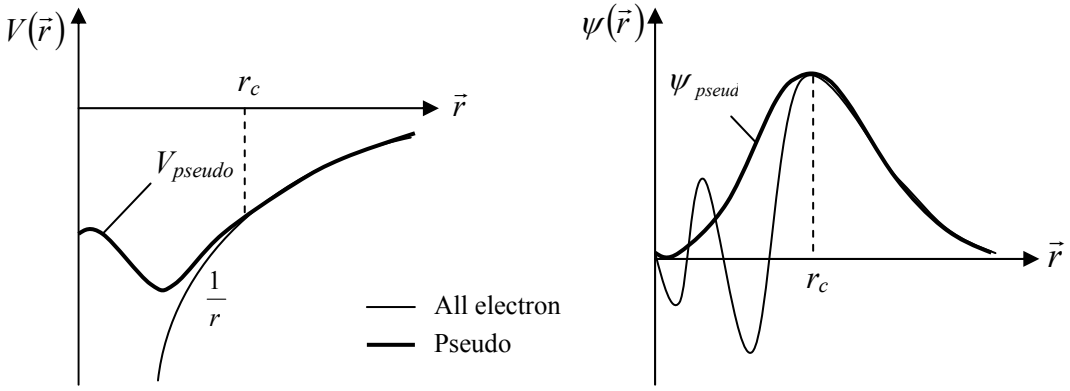

Figure 2.4: Schematic representation of a psedopotential (left) and a pseudowavefunction (right) along with all-electron potential and wavefunction. The radius at which all-electron and pseudofunction values match and identical is r_c. the pseudofunctions are smooth inside the core region.

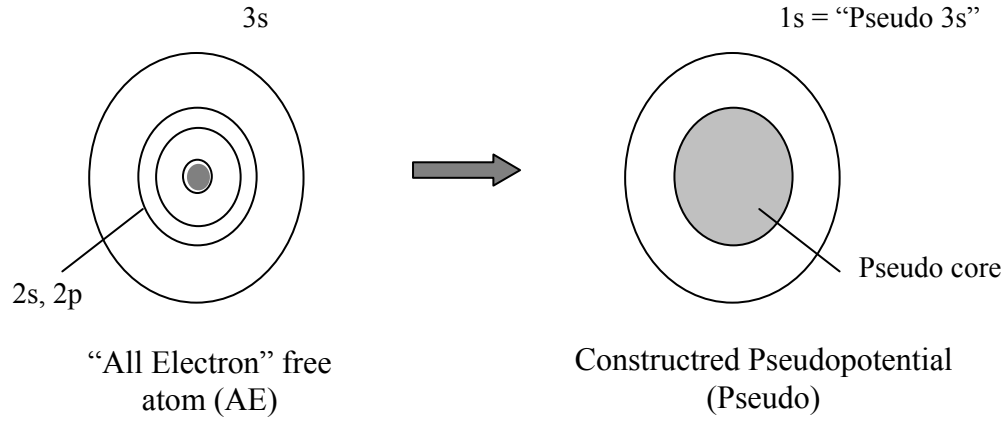

Figure 2.5: Schematic depicting principle of pseudopotential, of which core electrons are neglected.

2.3.2 Projected Augmented Wave (PAW) –Pseudopotentials (PP) in Plane Wave Basis

Owing to the number of plane waves would exceed any practical limit and lead to slow convergence, pseudopotentials (PP) instead of exact potentials need to be applied. There are plenty of PP approximations such as norm-conserving PP (NC-PP), ultrasoft PP (US-PP) and projected augmented wave (PAW) potentials. All these three methods have a common that they are presently frozen core methods in which the core electrons are pre-calculated in an atomic environment and kept frozen in the course of the remaining calculations (see Figure 2.6). Among those, PAW method which is developed by Blöch [57], is a very powerful tool for performing electronic structure calculation within the framework of DFT, combining some of the best features of PP and all-electron approaches [58]. In PAW, the all-electron wave function is decomposed into three terms as depicted in Figure 3.7:

$$\left|\psi_{n,\vec{k}}\right\rangle = \left|\widetilde{\psi}_{n,\vec{k}}\right\rangle - \sum_{lm\varepsilon}^{site}\left|\widetilde{\phi}_{lm\varepsilon}\right\rangle c_{lm\varepsilon} + \sum_{lm\varepsilon}^{site}\left|\phi_{lm\varepsilon}\right\rangle c_{lm\varepsilon} \tag{2.48}$$

where

$$c_{lm\varepsilon} = \left\langle \widetilde{p}_{lm\varepsilon}\left|\widetilde{\psi}_{n,\vec{k}}\right.\right\rangle \tag{2.49}$$

where $\widetilde{p}_{lm\varepsilon}$ is the projector function, $\phi_{lm\varepsilon}$ is the partial wave, lm is an index for the angular and magnetic quantum numbers and ε refers to a particular reference energy. The first term on the right side of equation (2.47) is the pseudowavefunction given by equation (2.42) in PW expansion; the second term is the pseudowavefunction represented on FFT-grid, on-site terms on atom-centered radial grids; while the third term is the exact (or all-electron) onsite terms on radial grids. The decomposition is also holds for charge density, kinetic energy, exchange-correlation energy and Hartree energy. For instance, charge density $n(\vec{r})$ can be represented by:

$$\begin{aligned} n(\vec{r}) &= \widetilde{n}(\vec{r}) - \widetilde{n}^1(\vec{r}) + n^1(\vec{r}) \\ &= \sum_{n,\vec{k}} f_{n,\vec{k}}\left|\widetilde{\psi}_{n,\vec{k}}(\vec{r})\right|^2 - \sum_{n,\vec{k},i,j} f_{n,\vec{k}}\left\langle\widetilde{\psi}_{n,\vec{k}}\left|\widetilde{p}_i\right.\right\rangle\left\langle\widetilde{p}_j\left|\widetilde{\psi}_{n,\vec{k}}\right.\right\rangle\left\{\left[\widetilde{\phi}_i(\vec{r})^*\,\widetilde{\phi}_j(\vec{r})\right] + \left[\phi_i(\vec{r})^*\,\phi_j(\vec{r})\right]\right\} \end{aligned} \tag{2.50}$$

where $f_{n,\vec{k}}$ denotes the occupancy factor weighted by the fractional BZ sampling volume, $i = lm\varepsilon$, $\widetilde{n}^1$ is the pseudo-density at one site, and n^1 is the compensation density at site. Whilst kinetic energy can be represented by:

$$E_{kin} = \widetilde{E} - \widetilde{E}^1 + E^1$$
$$= \sum_{n,\vec{k}} f_{n,\vec{k}} \left\langle \widetilde{\psi}_{n,\vec{k}} \right| -\Delta \left| \widetilde{\psi}_{n,\vec{k}} \right\rangle - \sum_{site\,(i,j)} \sum \rho_{ij} \left\langle \widetilde{\phi}_i \right| -\Delta \left| \widetilde{\phi}_j \right\rangle + \sum_{site\,(i,j)} \sum \rho_{ij} \left\langle \phi_i \right| -\Delta \left| \phi_j \right\rangle \quad (2.51)$$

where $\rho_{ij} = \sum_{n,\vec{k}} f_{n,\vec{k}}\, c_i^* c_j$ is an on-site density matrix.

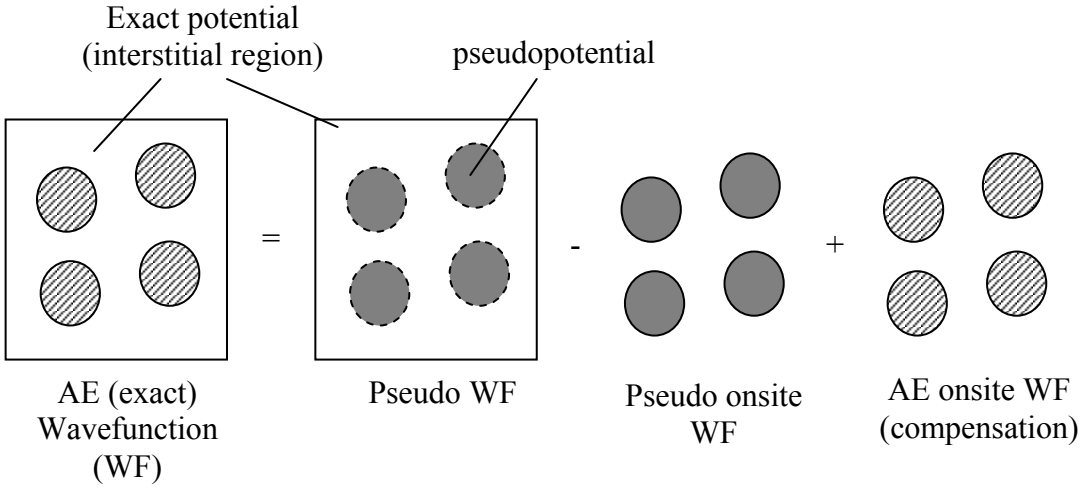

Figure 2.6: Schematic depicting the decomposition of exact wavefunction (and energy) into three terms.

For KS orbitals expanded in a plane-wave basis set, atomic pseudopotentials are employed, by which a local contribution E_{loc} and a angular momentum dependent non-local contribution E_{nonloc} contributes to external energy or electron-ion (ion = nucleus + core electrons) interaction energy, E_{ext} which can be represented by

$$E_{ext} = E_{loc} + E_{nonloc} \quad (2.52)$$

with
$$E_{loc} = \sum_{I=1}^{N} \int V_{loc,I}^{ion} \left(\vec{r} - \vec{R}_I\right) n(\vec{r})\, d^3 r \quad (2.53)$$

where V_{loc}^{ion} is the local ionic pseudopotential with $\vec{R}_I$ is the Cartesian position of the *I*th ion, and local pseudopotential energy contains the electron-ion Coulomb interaction.

CHAPTER 3

METHODOLOGY

In this research, VASP is used as the simulation tools for electronic structures of the gallium arsenide clusters. Introduction and the calculation process of VASP are discussed in this chapter.

3.1 Introduction to VASP

VASP which stands for Vienna Ab-Initio Software Package is initially written by Mike Payne at MIT. It has the same roots as the CASTEP/CETEP code but branched from this root at a very early stage [59]. The CASTEP version upon which VASP is based only supported local pseudopotentials and a Car-Parrinello type steepest descent algorithm. In 1989, VASP code had been brought by Jürgen Hafner to Vienna, Austria and continued its development at the Institut für Materialphysik of Universität Wien. The completion of the code had important contribution from Jürgen Furthmüller who joined the group in Jan 1993 and Georg Kresse who complete the parallelization in Jan 1997.

VASP is a versatile package for performing ab-initio quantum mechanical molecular dynamics (MD) using pseudopotentials and a plane wave basis set. The

approach implemented in VASP is based on a finite-temperature LDA with the free energy as variational quantity and an exact evaluation of instantaneous electronic ground state at each MD-step. VASP uses efficient matrix diagonalization schemes and an efficient Pulay/Broyden charge density mixing. All the problems occurring in the original Car-Parrinello method based on the simultaneous integration of electronic and ionic equations of motion, is avoided in these techniques. The interaction between ions and electrons is described by ultra-soft Vanderbilt pseudopotentials (US-PP) or by the projector-augmented wave (PAW) [57,60] method, in which both of them allow for a considerable reduction of the number of plane-waves per atom for transition metals and first row elements. Forces and stress can be easily calculated with VASP and used to relax atoms into their instantaneous ground state. Besides pure LDA for exchange-correlation functional, the gradient corrected functionals that are implemented in VASP to account for non-locality in exchange and correlation are: LM, PB, PW91, PBE, RPBE. Below is a short summary of some highlights of the VASP code [59]:

a) Owing to use of PAW and US-PP method, the size of the basis-set can be kept very small even for transition metal and first row elements like C and O. Generally not more than 100 plane waves (PW) per atom are required to describe bulk materials, in most cases even 50 PW per atom will be sufficient for a reliable description.
b) In any PW program, the execution time scales like N^3 for some parts of the code, where N is the number of valence electrons in the system. In the VASP, the pre-factors for the cubic parts are almost negligible leading to an efficient scaling with respect to system size. This is possible by evaluating the non-local contributions to the potentials in real space and by keeping the number of orthogonalisations small. For system with roughly 2000 electronic bands, the N^3 part becomes comparable to other parts. Therefore we expect VASP to be useful for systems with up to 4000 valence electrons.
c) VASP uses a rather “traditional” and “old-fashioned” self-consistency cycle to calculate the electronic ground state. The combination of this scheme with efficient numerical methods leads to an efficient, robust and fast scheme for evaluating the self-consistent solution of the Kohn-Sham functional. The implemented iterative matrix diagonalisation schemes

(RMM-DIIS, and blocked Davidson) are probably among the fastest scheme currently available.

d) VASP includes a full featured symmetry code which determines the symmetry of arbitrary configurations automatically.

e) The symmetry code is also used to set up the Monkhorst Pack special points (*k*-points) allowing an efficient calculation of bulk materials, symmetric clusters. The integration of the band-structure energy over the Brillouin zone is performed with smearing or tetrahedron methods. For the tetrahedron method, Bloch corrections, which remove the quadratic error of the linear tetrahedron method, can be used resulting in a fast convergence speed with respect to the number of special points.

f) VASP runs equally well on super-scalar processors, vector computers and parallel computers.

3.1.1 Software Packages Needed by VASP

VASP is a Fortran 90 program which is UNIX based. It requires a few packages in order to successfully execute the simulation. The packages with brief descriptions are listed as below:

i.) Fast Fourier Transform (FFT)

FFT is an efficient algorithm to compute the Discrete Fourier Transform and its reverse. FFTs are of great importance to a wide variety of applications, including solving partial differential equations and algorithms for quickly multiplying integers. In multiplications involving complex numbers, it is simply a method of laying out the computation which is much faster for large values of N, where N is the number of samples in the sequence. FFT works by using the divide and conquer approach, to break up the original N point sample into two (N / 2) sequences in order to make a series of smaller problem which is easier to be solved. For instance, FFTs approach only require 1 multiplication and 2 additions by breaking it down into a series of 2

point samples of which the recombination of the points is minimal, whereas the Discrete Fourier Transform needs $(N-1)^2$ complex multiplication and $N(N-1)$ complex addition.

ii.) BLAS

Basic Linear Algebra Subprograms (BLAS) are routines that provide standard building blocks for performing basic linear algebra operations such as vector and matrix multiplication. The Level 1 BLAS perform scalar, vector and vector-vector operations, the Level 2 BLAS perform matrix-vector operations, and the Level 3 BLAS perform matrix-matrix operations. They are commonly used in the development of high quality linear algebra software such as LAPACK (Linear Algebra PACKage) owing to its efficiency, portability and wide availability. Another package is ATLAS (Automatically Tuned Linear Algebra Software) which can automatically generate optimized BLAS library. It provides a full implementation of the BLAS application programming interfaces (APIs) as well as some additional functions from LAPACK. In addition, Intel Math Kernel Library (Intel® MKL) is also a package comprised of BLAS and LAPACK which is specifically support Intel processors.

iii.) MPI

For parallelization, VASP utilizes Message Passing Interface (MPI). Message passing is a method by which data from one processor's memory is copied to the memory of another processor. Hence, MPI is a language-independent computer communications descriptive API, with defined semantics, and with flexible interpretations. It was designed for high performance on both massively parallel machines and on workstation clusters. Simply stated, the goal of the MPI is to provide a widely used standard for writing message passing programs with high performance or scalability and high portability. MPICH (or MPICH2) and LAM/MPI are the examples of the implementation of the MPI.

3.2 Files Used by VASP

Table 3.1 listed the input and out files used by VASP. Basically, four important input files are INCAR, POTCAR, KPOINTS, and POSCAR, which are indispensable in the execution of VASP.

Table 3.1: A relatively large number of input and output files of VASP.

File	Input / Output File
INCAR	In
KPOINTS	In
POTCAR	In
POSCAR	In
stout	Out
IBZKPT	Out
CONTCAR	Out
CHGCAR	In / Out
CHG	Out
OUTCAR	Out
WAVECAR	In / Out
DOSCAR	Out
PCDAT	Out
OSZICAR	Out
EIGENVAL	Out
TMPCAR	In / Out
XDATCAR	Out
LOCPOT	Out
ELFCAR	Out
PROOUT	Out
PROCAR	Out

3.2.1 INCAR File

INCAR is the central input file of VASP. It determines ‘what to do and how to do it’, and contains a relatively large number of parameters. Most of these parameters have convenient defaults and any of the default values should not be changed without the awareness of their meaning. Some decisive parameters have to be set for specific calculations for instances geometry optimization and local density of states calculation. Therefore, understanding the parameters of INCAR helps manipulating the desired calculation well.

3.2.2 POTCAR File

The POTCAR file contains the pseudopotential for each atomic species used in the calculation. If the number of species is larger than one, simply combines the POTCAR files of each species into one. The first pseudopotential will correspond to the first species in the POSCAR and INCAR files, and so on. The POTCAR file also contains information about the atoms like their mass, their valence, the energy of the reference configuration for which the pseudopotential was created and others. In addition, it also contains a default energy cutoff and therefore it is not necessary to specify it in the INCAR file. The default value will be overwritten if a different value is specified in INCAR file. There are two types of pseudopotentials supplied by VASP, which are PAW and US-PP. Generally, the PAW potentials are more accurate than the US-PP. There are two reasons for this: first, the radial cutoffs (core radii) are smaller than the radii used for the US-PP, and second the PAW potentials reconstruct the exact valence wavefunction with all nodes in the core region. Since the core radii of the PAW potentials are smaller, the required energy cutoffs and basis sets are also somewhat larger. Most of the PAW potentials were optimized to work at a cutoff of 250-300 eV. Pseudopotential that is used in this research is PAW for GGA (PBE).

3.2.3 POSCAR File

This file contains the lattice geometry and the ionic positions, optionally also stating velocities and predictor-corrector coordinates for a Molecular Dynamic (MD) run. After the lattice geometry, number of atom per atomic species is given in the order consistent with the POTCAR and INCAR file. The atomic positions are provided either in Cartesian coordinates or in direct coordinates which is respectively fractional coordinates. In direct mode, the positions are given by

$$\vec{R} = x_1\vec{a}_1 + x_2\vec{a}_2 + x_3\vec{a}_3 \quad , \tag{3.1}$$

where $\vec{a}_{1\ldots3}$ are the three basis vectors and $x_{1\ldots3}$ are the supplied values. In the Cartesian mode the positions are scaled by a factor *s*, which is the lattice constant used to scale all lattice vectors besides atomic coordinates, as given by:

$$\vec{R} = s\begin{pmatrix} x_1 \\ x_2 \\ x_3 \end{pmatrix} \quad . \tag{3.2}$$

In order to be recognized, “Cartesian” (or ‘C’, ‘c’, ‘K’ or ‘k’) is written before the Cartesian atomic position, and any other character or “Direct” will switch to direct mode.

3.2.4 KPOINTS File

The file KPOINTS must contain the *k*-point coordinates and weights or the mesh size for creating the *k*-point grid. There are a few formats to create KPOINTS file:

i.) Entering all *k*-points explicitly with Cartesian or reciprocal coordinates. In the reciprocal mode, the *k*-points are given by

$$\vec{k} = x_1\vec{b}_1 + x_2\vec{b}_2 + x_3\vec{b}_3 \quad , \tag{3.3}$$

where $\vec{b}_{1...3}$ are the three reciprocal basis vector and $x_{1...3}$ are the supplied value. In the Cartesian input format the *k*-points are given by:

$$\vec{k} = \frac{2\pi}{a}(x_1, x_2, x_3) \quad . \tag{3.4}$$

Table 3.2 list the input required in order to specify the high symmetry *k*-points and Figure 3.1 shows the example of important *k* point on the BZ of a face-centered cubic (fcc) crystal.

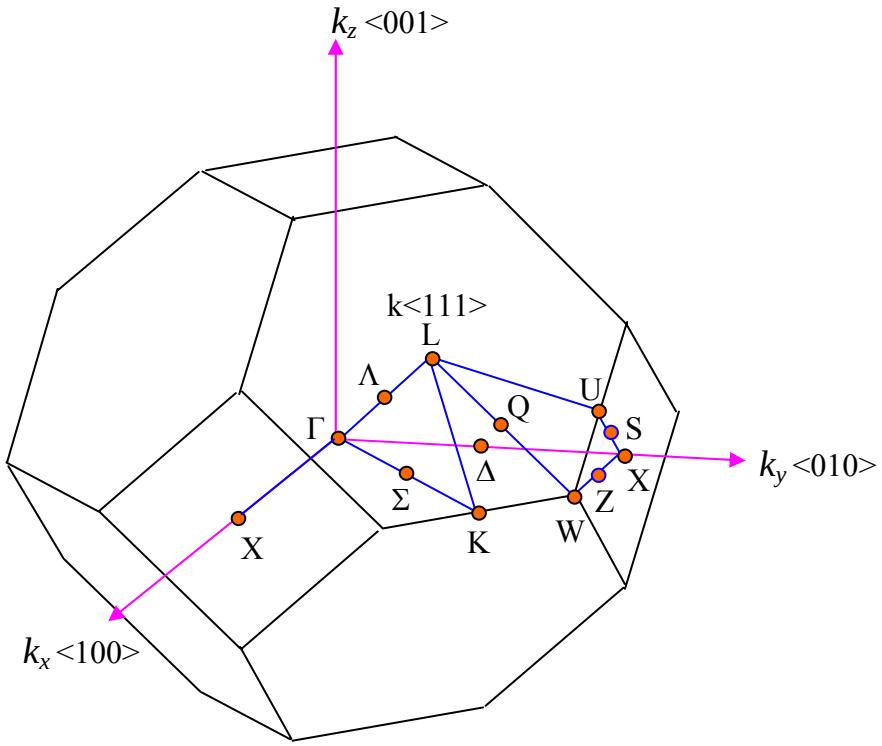

Figure 3.1: The First Brillouin zone of a fcc lattice, with high symmetry *k*-points and direction of planes marked. The zone center is Γ. Note that this is also the Wigner-Seitz cell of a body-centered cubic (bcc) lattice in real space.

Table 3.2: Coordinates of high symmetry *k*-points in Cartesian and reciprocal mode.

Point	Cartesian coordinates (unit of 2π/a)	Reciprocal coordinates
W	(½ 0 1)	(½ ¾ ¼)
K	(¾ ¾ 0)	(⅜ ⅜ ¾)
L	(½ ½ ½)	(½ ½ ½)
Γ	(0 0 0)	(0 0 0)
X	(0 0 1)	(½ ½ 0)

ii.) Strings of *k*-points for bandstructure calculation that connecting specific points of BZ, for example strings connecting Γ – X – W – Γ.

iii.) Automatic k-mesh generation which requires only the input of subdivisions of the BZ in each direction and the origin for the k-mesh. The k-mesh is generated according to the Monkhorst-Pack scheme [61]. This essentially means that the sampling *k*-points are distributed homogeneously in the BZ, with rows or columns of *k*-points running parallel to the reciprocal lattice vectors that span the BZ. The construction rule of Monkhorst-Pack is

$$\vec{k}_{ijk} = u_i \vec{b}_1 + u_j \vec{b}_2 + u_k \vec{b}_3 \tag{3.5}$$

where $$u_i = \frac{2r - N_i - 1}{2N_i} \quad , \quad r = 1,2,\ldots,N_i \quad , \tag{3.6}$$

$\vec{b}_{1\ldots3}$ are the reciprocal lattice vectors, and N_i is the numbers of the subdivisions that determines the number of *k*-points in *i*-direction. There are two modes which are original Monkhorst-Pack, in which the k-mesh will be shifted off Γ for even divisions to get a mesh which is centered symmetrically around Γ, and Gamma mode which generates Monkhorst-Pack type meshes with the origin being at the Γ point. All symmetry operations of Bravais lattice are applied to all *k*-points and the irreducible *k*-points (or Irreducible Brillouin Zone, IBZ) are then extracted.

3.3 Algorithm Used in VASP

Most of the algorithms implemented in VASP use an iterative matrix-diagonalization scheme. The used algorithms are based on the conjugate gradient scheme, block Davidson scheme, or a residual minimization scheme-direct inversion and the iterative subspace (RMM-DIIS). An efficient Broyden/Pulay mixing scheme is utilized for the mixing of the charge density. The typical flow-chart of VASP calculating KS ground state is shown in Figure 3.2. Input charge-density n_{in} and wavefunctions $\{\phi_n \ , n = 1,\ldots,N_b\}$, are independent quantities. At startup, charge-

density is by default taken as the superposition of atomic pseudo charge densities, while wavefunctions by default is set up by filling wavefunction arrays with random numbers. Within each self-consistency loop the charge density is used to set up the Hamiltonian and the wavefunctions are then optimized iteratively so that they get closer to the exact wavefunctions of this Hamiltonian. From the optimized wavefunctions, a new charge density is calculated which is then mixed with the old input-charge density. Figure 3.2 shows the flow chart of the algorithm and a more detailed explanation is given in the next paragraph.

From the input charge densities, the local part of the Kohn-Sham Hamiltonian ($H = T + V_{loc}^{sc} + V_{nonloc}^{sc}$) which is given by

$$V_{loc}^{sc} = V_{loc}^{ion} + V_H[n_{in}] + \mu_{XC}[n_{in}] \tag{3.7}$$

and the corresponding double counting corrections

$$E_{d.c.}[n_{in}] = -\frac{1}{2}E_H[n_{in}] + E_{XC}[n_{in}] - \int \mu_{XC}(\vec{r})n_{in}(\vec{r})d^3r \tag{3.8}$$

are evaluated. For US-PP, the non-local part of the PP depends also on the local potential and must be calculated accordingly. In the next step the N_b trial wavefunctions are improved using iterative method and the new eigenenergies are used to calculate a new Fermi energy and new partial occupancies. The total free energy for the current iteration is calculated as the sum of the bandstructure energy, the entropy term and double counting corrections (see equation 3.9).

$$F = \sum_n f_n \varepsilon_n - \sum_n \sigma S\left(\frac{\varepsilon_n - \mu}{\sigma}\right) + E_{d.c.}[n_{in}] \quad , \tag{3.9}$$

where $f_n = 1$ for occupied bands and $f_n = 0$ for unoccupied bands, ε_n is bandstructure energy, σ is a parameter to control the smearing of the occupation function f_n, μ is the Fermi energy, and $S(f_n)$ is the entropy term. The calculated energy conceptually corresponds to the energy evaluated from the Harris-Foulkes functional, which is non-self-consistent (in contrast to the KS functional) and the Harris Foulkes functional (defined in equation (3.9)) requires the calculation of the bandstructure energy for a fixed charge density n_{in}. In VASP, it is easy to evaluate this energy by keeping the initial charge density fixed and iterating the eigenvectors only until they are converged.

To obtain the exact KS-ground-state energy selfconsistency with respect to the input charge density requires that the charge density residual vector $R[n_{in}]$ given by

$$R[n_{in}] = n_{out} - n_{in} \tag{3.10}$$

is zero, where the output charge density n_{out} is calculated from the wavefunctions with the relation of $n_{out}(\vec{r}) = \sum_n f_n |\phi_n(\vec{r})|^2$. The residual vector $R[n_{in}]$ allows calculating a new charge density n_{in} for the next selfconsistency loop. In principle it is necessary to evaluate the eigenfunctions ϕ_n exactly for each new input charge density making n_{out} and the residual vector R functionals of the input charge density n_{in} only. However, even in conjunction with complex Broyden like mixing techniques, it turns out that this is not necessary if the final wavefunctions of the previous mixing iteration are used as new initial trial wavefunctions. In such case a few steps in the iterative matrix diagonalization are sufficient to obtain a reliable result for the charge density residual vector R.

The conjugate gradient (CG) and the residual minimization (RMM) scheme do not recalculate the exact KS eigenfunctions but an arbitrary linear combination of the lowest eigenfunctions of a number of bands. Thus, it is in addition necessary to diagonalize the Hamiltonian in the subspace spanned by the trial wavefunctions, and to transform the wavefunctions accordingly as shown below.

$$\begin{aligned} \langle \phi_j | \mathbf{H} | \phi_i \rangle &= H_{ij} \\ H_{ij} U_{jk} &= \varepsilon_k U_{ik} \\ \phi_j &\leftarrow U_{jk} \phi_k \end{aligned} \tag{3.11}$$

This is called subspace diagonalization and can be performed either before or after CG or RMM scheme, in which the first choice is preferable in the self-consistent calculations.

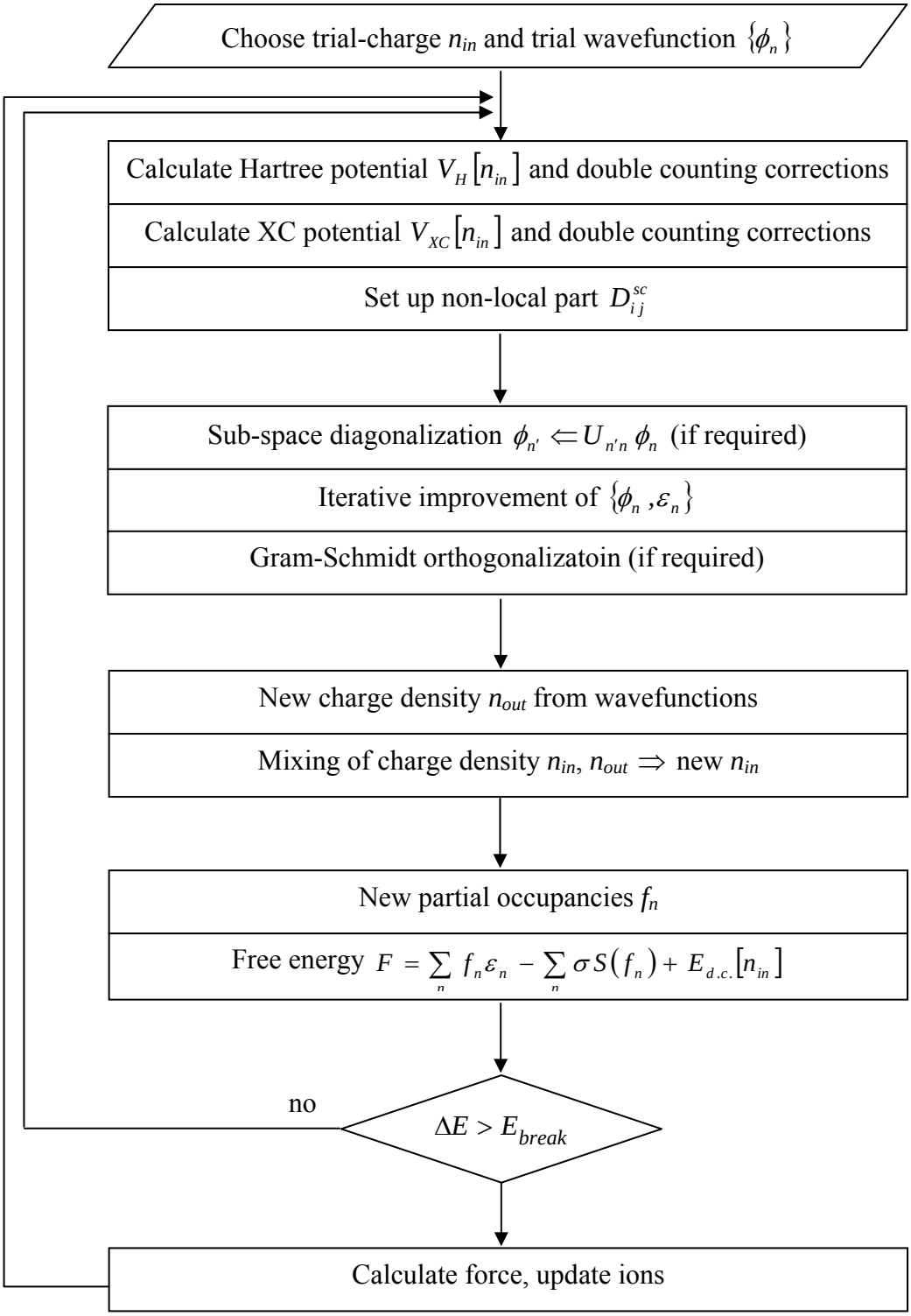

Figure 3.2: Flow chart of iterative methods for the diagonalization of the KS-Hamiltonian in conjunction with an iterative improvement (mixing techniques) of the charge density for the calculation of KS-ground-state.

Gram-Schmidt is a orthogonalization method which is only required for the RMM scheme and it is performed after the scheme. In general all iterative algorithms work very similar, where the core quantity is the residual vector:

$$\left|R_n\right\rangle = \left(\mathbf{H} - \varepsilon_n\right)\left|\phi_n\right\rangle \qquad , \qquad \varepsilon_n = \left\langle\phi_n\right|\mathbf{H}\left|\phi_n\right\rangle \tag{3.12}$$

The residual vector is added to the wavefunction ϕ_n, and the algorithms differ in the way this is exactly done.

3.3.1 Conjugate Gradient Algorithm

The conjugate gradient algorithm selects the successive direction vectors as a conjugate version of the successive gradients obtained as the method progresses. Thus, the directions are not specified beforehand, but rather are determined sequentially at each step of the iteration. At step *k* one evaluates the current negative gradient vector and adds to it a linear combination of the previous direction vectors to obtain a new conjugate direction vector along which to move. There are three primary advantages to this method of direction selection. First, unless the solution is attained in less than *n* steps, the gradient is always nonzero and linearly independent of all previous direction vectors. Indeed, as the corollary states, the gradient g_k is orthogonal to the subspace β_k generated by d_0, d_1, …..,d_{k+1}. If the solution is reached before *n* steps are taken, the gradient vanishes and the process terminates.

Second, a more important advantage of the conjugate gradient method is the especially simple formula that is used to determine the new direction vector. This simplicity makes the method only slightly more complicated than steepest descent. Third, because the directions are based on the gradients, the process makes good uniform progress toward the solution at every step. This is in contrast to the situation for arbitrary sequences of conjugate directions in which progress may be slight until

the final few steps. Although for the pure quadratic problem uniform progress is of no great importance, it is important for generalizations to non quadratic problems.

1. $g_0 \leftarrow Qx_0 + b$

2. $d_0 \leftarrow -g_0$

3. **for** $k = 0,\ldots\ldots,n-1$ **do**

a) $\alpha_k \leftarrow -\dfrac{g_k^T d_k}{d_k^T Q d_k}$

b) $x_{k+1} \leftarrow x_k + \alpha_k d_k$

c) $_{gk+1} \leftarrow Qx_{k+1} + b$

d) $\beta k \leftarrow \dfrac{g_{k+1}^T Q d_k}{d_k^T Q d_k}$

e) $d_{k+1} \leftarrow -g_{k+1} + \beta_k d_k$

4. **return**. x_n

Step 3b when $k = 0$ is a steepest descent. Each subsequent step moves in a direction that modifies the opposite of the current gradient by a factor of the previous direction. Step 3a – 3e gives us the Q-orthogonality of the descent vector $d_0,\ldots\ldots,d_{n-1}$.

3.3.2 Block Davidson Algorithms

Davidson [59] has devised methods that are now widely applied to electronic structure problems. There are a number of variations that cannot be covered here. A primary point is that the Davidson approach is closely related to the Lanczos algorithm, but adapted to be more efficient for problems in which the operator is diagonally dominant. This is often the case in electronic structure problems for example plane wave algorithms.

The flavor of the Davidson methods can be illustrated by defining the diagonal part of the Hamiltonian matrix as $D_{mm'} = H_{mm}\delta_{mm'}$ and rewriting the eigenvalue problem $H\psi = \varepsilon\psi$ as

$$(H - D)\psi = (\varepsilon I - D)\psi \tag{3.13}$$

or

$$\psi = (\varepsilon I - D)^{-1}(H - D)\psi \tag{3.14}$$

Here I is the unit matrix, inversion of $I - D$ is trivial, and $H - D$ involves only off-diagonal elements. The latter equation is very similar to perturbation theory and suggests iterative procedures that converge rapidly if the diagonal part of the Hamiltonian is dominant. An algorithm has been suggested by Lenthe and Pulay [91] that involves three vectors at each step of the iteration.

3.3.3 Residual Minimization Scheme-Direct Inversion In The Iterative Subspace (RMM-DIIS)

The approaches described up to now (and the minimization methods described below) converge to the lowest state with no problems because the ground state is an absolute minimum. In order to find higher states, they must ensure orthogonality, either implicitly as in the Lanczos methods or by explicit orthogonalization. The residual minimization method (RMM) proposed by Pulay [92] avoids this requirement and converges to the state in the spectrum with eigenvalue closest to the trial eigenvalue ε because it minimizes the norm of a "residual vector" instead of the energy.

Since the approach of Pulay minimizes the residual in the full Krylov iterative space generated by previous iterations, the method is known as RMM-DIIS for "residual minimization method by direct inversion in the iterative subspace". The general idea is

$$\psi^{n+1} = c_o \psi^o + \sum_{j=1}^{n+1} c_j \delta\psi^j \tag{3.15}$$

where the entire set of c_j is chosen to minimize the norm of the residual R^{n+1}. (Pre-conditioning can also be applied at each step [57] to speed the convergence). The c_j coefficients can be obtained by diagonalizing the Hamiltonian in the iterative subspace $\left(\psi^o, \psi^1, \psi^2 ..... \psi^n\right)$, which is a miniscule operation since the number of vectors is at most 10 or so. The time-consuming step is the operation $\mathrm{H}\psi$, which is a matrix operation requiring, in general, $O\left(N_b^2\right)$ operations for each eigenvector ψ, where N_b is the size of the basis.

3.4 Simulation Process

Generally, the simulation process in this research contains the steps shown in Figure 3.3 and this flow chart is applied to all of the structures in order to obtain the electronic structures. Each step of the process will be discussed in the next sections. The discussion of the methods provided in the following is not specific to any of the simulated structures but is universal and generally discussed.

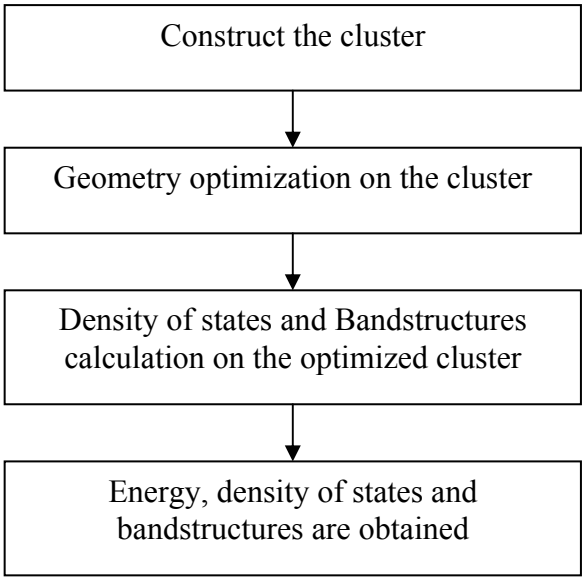

Figure 3.3: Flow chart of the electronic structure simulation process of gallium arsenide clusters.

3.4.1 Construction of the Clusters

Construction of a structure is done by specifying the Cartesian or direct coordinate of each atom of the structure in the POSCAR file. As discussed in the Section 2.2.1, due to the boundary conditions in VASP which are periodic in all three dimensions, supercell method is used for isolated structure calculations. The supercell is a simple cubic cell with large lattice length in order to create sufficient vacuum region for the isolated structure. The purpose is to eliminate the interaction between isolated clusters across the cell boundary in the periodic array and to make sure the results will be those for the isolated cluster. The structure of the cluster is built in the middle of the supercell. The supercell size is at least three times larger than the lattice constant of solid gallium arsenide. The distance between two isolated clusters is made about 2-3 times the size of the clusters to make sure the intermolecular interaction is negligible. In this research, the minimum lattice length of the supercell is taken to be 17 Å for the smallest clusters as three to six atoms clusters. Example is shown below with gallium arsenide cluster of 4 atoms. The

largest distance between atoms is taken (2.816 Å) and lattice length of 17 Å is built so that the distance between clusters is more than 10 Å, which is more than 3 times the individual cluster size. The lattice length increases as the number of atom of the cluster increases.

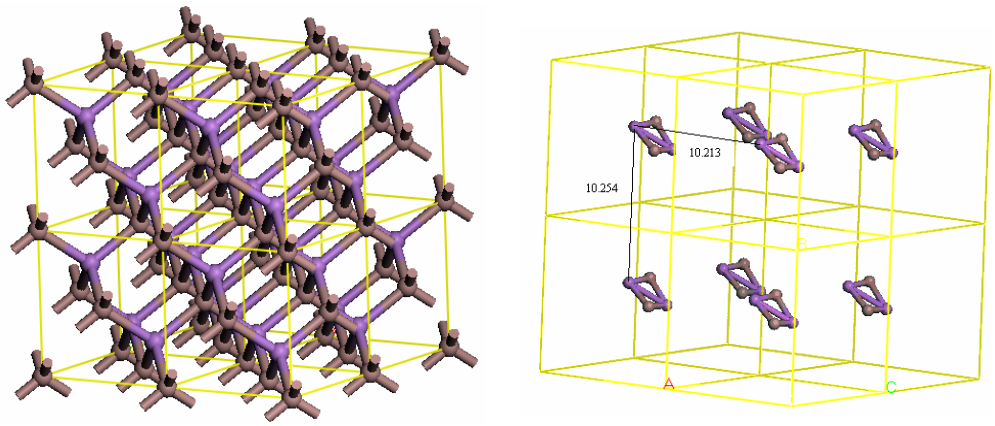

(a) (b)

Figure 3.4: (a) Bulk gallium arsenide with its unit cells repeated in 3 dimensions. (b) supercells with Ga_2As_2 cluster in the center and the distance between clusters is large. The ● show the Ga atoms and ● show the As atoms.

3.4.2 Geometry Optimization

Geometry optimization is used to find the minima on the potential energy surface with these minimum energy structures representing equilibrium structures. When we first construct a raw cluster structure, the ion positions and bond lengths are not accurate and the structure is not in a stable condition. Thus geometry optimization is needed to be accomplished before any other calculation of the relevant structure. Force is a crucial element in the geometry optimization and it is relatively simple to be calculated by using plane wave basis set. The forces on a nucleus I with position R_I can be conveniently described as $\vec{\mathbf{F}}_I = \partial F / \partial \vec{R}_I$, which contains Pulay as well as Hellmann-Feymann contributions as shown in equation (2.40). F is the free energy which depends on the wavefunction ϕ_n , the partial occupancies f_n, expansion coefficients C_{nq} and the ionic position R_I. This force can

then be used to find the ground state position of the atoms. The forces can be used to calculate a molecular dynamics trajectory. As the atoms move to new position, the electronic wavefunctions must also change. As the forces point to the minimum in the energy variation where the forces vanish, the atoms move toward an equilibrium structure. Thus, geometry optimization is also referred to as energy minimization.

In VASP, geometry optimization can be done with a few algorithms such as standard ab-initio molecular dynamics (MD), RMM-DIIS implementation of quasi-Newton, conjugate gradient (CG) and damped molecular dynamics. MD is a algorithm that performs the energy minimization into global minimum whereas all other algorithms are destined for relaxations into a local energy minimum. Damped MD is often useful for very bad initial guess structure while RMM-DIIS is usually the best choice that is close to the local minimum but fails badly if the initial positions are a bad guess. Therefore for difficult relaxation problems, CG is recommended because it possesses the most reliable backup routines.

In this research, the geometry of the clusters has been determined by static relaxation using CG minimization and exact Hellmann-Feynman forces. For small clusters (n = 2 – 6), the most stable geometry is found from the many possible configurations with varying coordinates. When the size of the clusters is getting larger, the number of topologically distinct structures which is called isomers increases very rapidly with the number of atoms, n. Therefore, for larger clusters (n > 6) dynamical simulated annealing (SA) of the cluster structure was performed in addition. SA runs can be very helpful for an automatic determination of favorable structural models and it can avoid unfavorable local minima in the energy surface. The elevated temperatures strategy used in SA allows an efficient sampling of the potential energy surface [62]. Final structural refinement using the static CG approach for local minimization is performed after the system is cooled down to the best configurations. The following sections describe the parameters for CG and SA algorithms in the INCAR file.

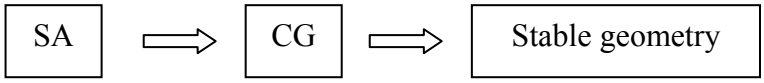

Figure 3.5: Algorithm of geometry optimization used for large clusters.

3.4.2.1 INCAR for Conjugate Gradient Geometry Optimization

Other than the default parameters specified in the POTCAR file, the following parameters is written in the INCAR file to overwrite those in the POTCAR (see Figure 3.6). Phrases after "!" briefly describe the flags respectively. The key of switching to CG algorithm is by setting IBRION = 2 and POTIM = 0.1 determine the scaling constant for the forces. The simulation is started with wavefunctions initialized according to flag INIWAV (default = 1 :fill wavefunction array with random numbers) and superposition of atomic charge densities is taken with ICHARGE = 2. High energy cutoff and precision are set to ensure the accuracy of the results. For cluster or isolated molecule with large supercell, Gaussian smearing is adopted and the width of the smearing is set to a significantly small value, of which 0.001 is set in this research. During the geometry optimization, the shape and volume of the supercell is kept constant and only the internal ions are relaxed (ISIF = 2), in the meanwhile force and stress tensor are calculated. The total energies and equilibrium geometries will converge to within the chosen precision (EDIFF and EDIFFG). EDIFF specifies the global break condition for the electronic self-consistency loop. The relaxation of the electronic degrees of freedom will be stopped if the total or free energy and the eigenvalues change between two steps are both smaller than EDIFF. Whereas EDIFFG defines the break conditions for the ionic relaxation loop. For negative value, the relaxation will stop if all forces are smaller than | EDIFFG | (in unit of eV/Å). Sixty numbers of ionic steps is set and more steps should be added if convergence can not be reached.

```
SYSTEM = Gallium arsenide cluster

## Start parameter for this Run:
  ISTART    = 0                    ! job     : 0-new  1-cont  2-samecut
  ICHARGE = 2              ! charge: 1-file  2-atom  10-const
  PREC        = HIGH

## Electronic Relaxation
  ENCUT = 350 eV
  EDIFF = 0.1E-0.7       ! stopping-criterion for ELM

## Ionic Relaxation
   IBRION = 2                ! ionic relax: 0-MD  1-qausi-New  2-CG
   ISIF = 2                  ! stress and relaxation
        EDIFFG = -0.01            ! stopping-criterion for IOM
        NSW = 60                  ! number of steps for IOM
        POTIM = 0.1               ! time-step for ionic-motion

## DOS related values
   ISMEAR = 0                ! -4-tet  -1-fermi  0-gaussian
   SIGMA = 0.001             ! broadening in eV
```

Figure 3.6: Parameters for CG algorithm in INCAR file.

In the first step of CG algorithm, ions are changed along the direction of the steepest descent which is the direction of the calculated forces and stress tensor. The CG method requires a line minimization which is performed in several steps as below:

1. First a trial step into the search direction (scaled gradients) is done with the length of the trial step controlled by the POTIM parameter. Then the energy and the forces are recalculated.
2. The approximate minimum of the total energy is calculated from a cubic or quadratic interpolation using energies and forces at $\vec{x}_0$ and $\vec{x}_1$ (see Figure 3.7), taking into account the change of the total energy and the change of the forces, then a corrector step to the approximate minimum is performed.
3. After the corrector step the forces and energy are recalculated and it is checked whether the forces contain a significant component parallel to the

previous search direction. If this is the case, the line minimization is improved by further corrector steps using a variant of Brent's algorithms.

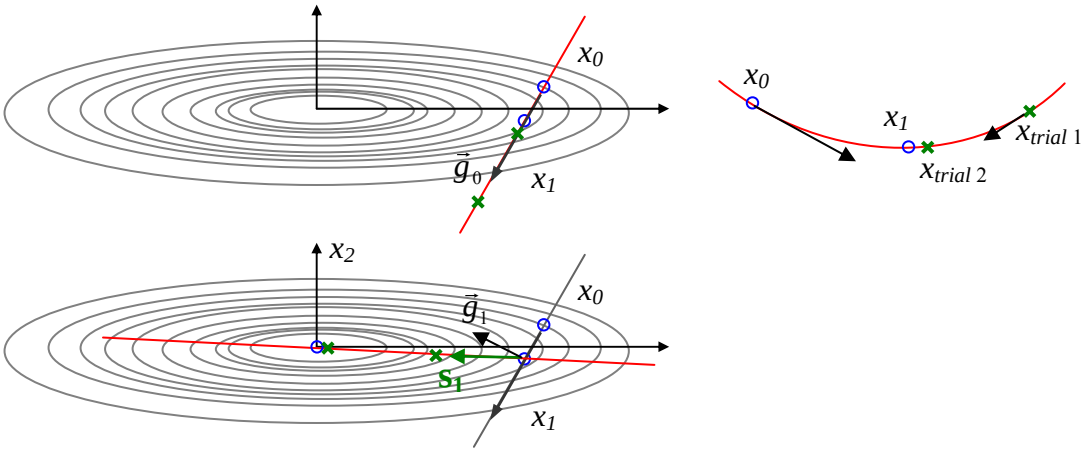

Figure 3.7: Conjugate gradient techniques: (top) Steepest descent step from $\vec{x}_0$ search for minimum along $\vec{g}_0$ by performing several trial steps to $\vec{x}_1$. (below) New gradient $\vec{g}_0 = \vec{g}(\vec{x}_1)$ is determined and $\vec{s}_1$ (green arrow) is conjugated. For 2D functions the gradient now points directly to the minimum. Minimization along search direction $\vec{s}_1$ is continued.

3.4.2.2 INCAR for Simulate Annealing

Simulated annealing (SA) is a generic probabilistic meta-algorithm for the global optimization problem for locating a good approximation to the global optimum of a given function in a large search space. It is a generalization of a Monte Carlo method for examining the equations of state and frozen states of n-body systems [63]. This technique involves heating and controlled cooling of a material to increase the size of its crystals and reduce their defects. The heat causes the atoms to become loose from their initial positions and wander randomly through states of higher energy whereas the slow cooling provides more chances of finding configurations with lower internal energy than the initial one. SA's major advantage over other methods is an ability to avoid becoming trapped at local minima.

Because of the SA is a dynamic process that involves temperatures, there are a few parameters are to be included in the INCAR file as shown in Figure 4.8.

```
SYSTEM = Gallium arsenide cluster

## Start parameter for this Run:
      ISTART    = 0              ! job     : 0-new  1-cont  2-samecut
      ICHARGE = 2                ! charge: 1-file  2-atom  10-const

## Electronic Relaxation
      ENCUT = 350 eV
      IALGO = 48                  ! RMM-DIIS algorithm for electrons
      LREAL = .FALSE             ! evaluate projection operators in rec. space
      NELMIN = 4                  ! do a minimum of four electronic steps
      MAXMIX = 50               ! keep dielectric function btwn ionic movemen

## Ionic Relaxation
      IBRION = 0                   ! ionic relax: 0-MD  1-qausi-New  2-CG
      NSW = 600                    ! number of steps for IOM
      POTIM = 3.00                 ! time-step for ionic-motion
      NBLOCK = 1                   ! inner block
      SMASS = -1.00                ! Nose mass-parameter (am)
      TEBEG = 1700                 ! temperature
      TEEND = 0
```

Figure 3.8: Parameters for SA algorithm in INCAR file.

Same as CG process, the energy cutoff of 350eV is used in the SA algorithm. IBRION = 0 denotes that the MD algorithm is combined in the SA process. RMM-DIIS algorithm is set for electrons in order to reduce the number of orthonormalization steps and speed up the calculation. The projection operators are evaluated in reciprocal space (LREAL = FALSE) and at least 4 electronic iterations per ionic step is required for MD runs. MAXMIX specifies the maximum number of vectors stored in the Broyden/Pulay mixer or in other words it corresponds to the maximal rank of the approximation of the charge dielectric function build up by the mixer. It should be set roughly three times the number of iterations in the first ionic step. In the process of simulated annealing, the initial temperature is set to a very high temperature. This temperature is set to 1700 K which is a bit higher than the

melting point of gallium arsenide (1511 K). While these are indeed indicators of a transition from solid to liquid, the temperature at which this happen in a MD simulation is invariably higher than the melting temperature. In fact, the melting point is by definition the temperature at which the solid and the liquid phase coexist (they have the same free energy). However, lacking a liquid seed from where the liquid could nucleate and grow, overheating above melting commonly occurs. In this region the system is in a thermodynamically metastable state, nevertheless it appears stable within the simulation time. An overheated bulk crystal breaks down when its *mechanical instability point* is reached. This point may correspond to the vanishing of one of the shear moduli of the material or to similar instabilities, and is typically larger than melting temperature by an amount of the order of 20-30%. If the initial annealing temperature is too low, the search space is limited and the search becomes trapped in a local region. If the initial temperature is too high, the algorithm spends a lot of time "boiling around" and wasting CPU time. The idea is to initially have a high percentage of moves that are accepted.

The temperature reaches zero at the end after 600 numbers of ionic steps. 3 fs time step is set for the ionic motion. The decrement of the temperature is controlled by the option SMASS. In this case the velocities of the MD are scaled by each NBLOCK step to the temperature produced from the formalism TEMP = TEBEG + (TEEND – TEBEG) × NSTEP / NSW, where NSTEP is the current step (starting from 1).

Figure 3.9 is the flowchart illustrating the algorithm of SA. There are two major processes that take place in the simulated annealing algorithm. First, for each temperature, the simulated annealing algorithm runs through a number of cycles. The number of cycles is predetermined by the programmer. As a cycle runs, the inputs are randomized. The randomization process takes the previous input values and the current temperature as inputs. The input values are then randomized according to the temperature. A higher temperature will result in more randomization; a lower temperature will result in less randomization.

Once the specified number of training cycles have been completed, the temperature can be lowered. Once the temperature is lowered, it is determined whether or not the temperature has reached the lowest temperature allowed. If the temperature is not lower than the lowest temperature allowed, then the temperature is lowered and another cycle of randomizations will take place. If the temperature is lower than the lowest temperature allowed, the simulated annealing algorithm terminates.

At the core of the simulated annealing algorithm is the randomization of the input values. This randomization is ultimately what causes simulated annealing to alter the input values that the algorithm is seeking to minimize. The randomization process must often be customized for different problems.

By analogy with this physical process, each step of the SA algorithm replaces the current solution by a random "nearby" solution, chosen with a probability that depends on the difference between the corresponding function values and on a global parameter, which is temperature that gradually decreases during the process. The dependency is such that the current solution changes almost randomly when the temperature is large, but increasingly move downhill to lower kinetic energy as the temperature goes to zero. This optimization process does not only proceed uniformly downhill, but is allowed to make occasional uphill moves. The allowance for moving uphill saves the method from becoming stuck at local minima.

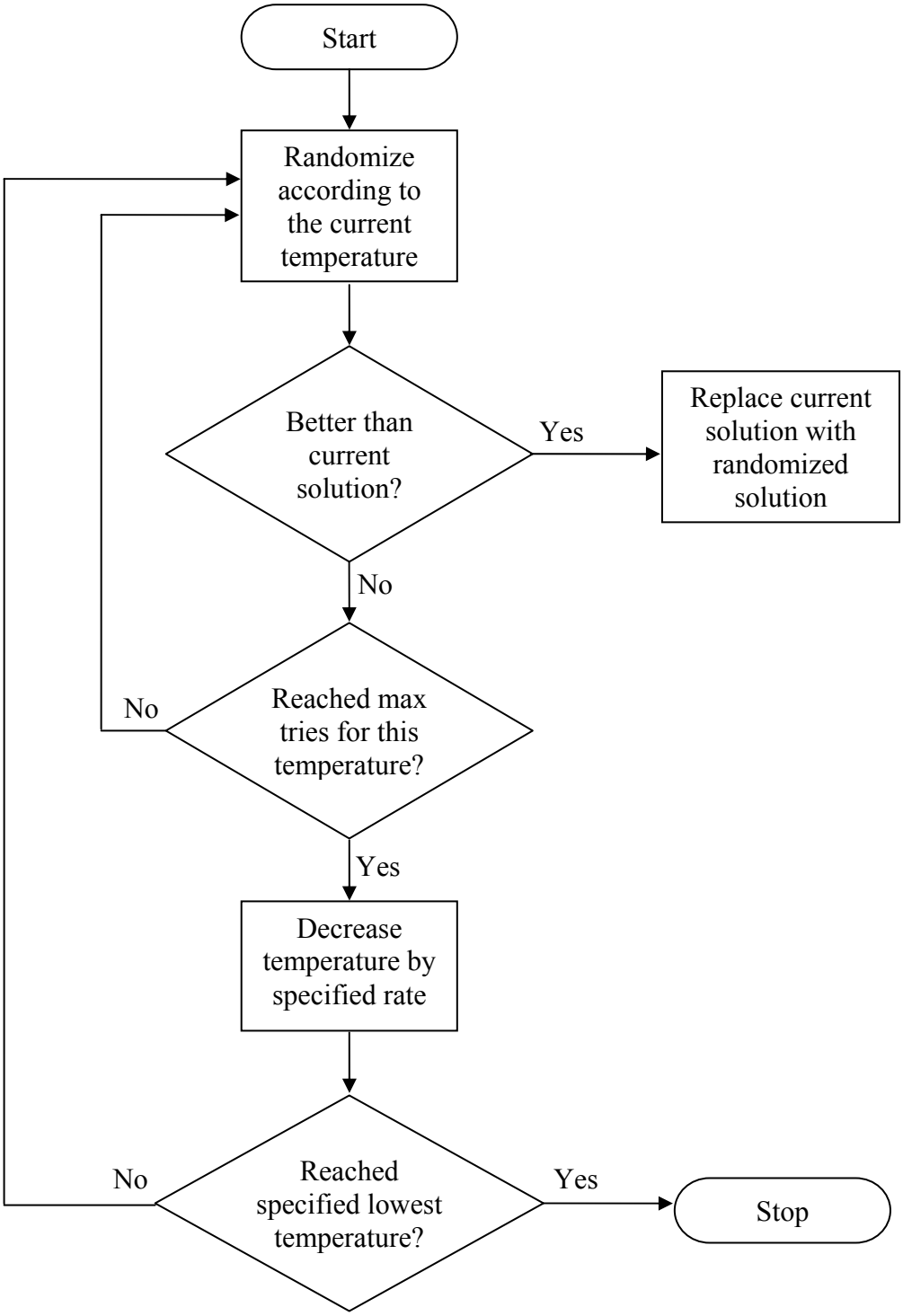

Figure 3.9: Flowchart illustrating the algorithm of SA.

3.4.2.3 KPOINTS for Geometry Optimization

As discussed in section 2.2.1, only single *k*-point is needed for isolated molecule. Therefore, gamma point is used for the geometry optimization of the isolated clusters in this research and the KPOINTS file for such case is shown in Figure 3.10.

```
Monkhorst Pack          ! comment
  0                     ! Automatic generation
  Monkhorst Pack          ! M=Monkhorst-Pack
  1     1     1         ! grid
  0     0     0         ! shift
```

Figure 3.10: Parameters for geometry optimization in KPOINTS file.

The KPOINTS file is written in the Monkhorst-Pack scheme as discussed in the section 3.2.4. The automatic generated k-mesh will be created and given in the file IBZKPT. The fourth line of the KPOINTS gives a gamma point with the coordinate (0 0 0) and the weight 1.0.

3.4.3 Electronic Structures Calculations

After the geometry optimization is performed and the stable geometry is obtained, electronic structure calculations are then done by using the final structure generated. The usual way to calculate DOS and bandstructure is the following: first charge density using a few *k*-points (gamma point for the case of isolated clusters) in a static self-consistent run is performed; the next step is to perform a non-

selfconsistent calculation using the charge density file, CHGCAR from this self-consistent run. This is the only way to calculate the bandstructure, because for bandstructure calculation the supplied *k*-points form usually no regular three-dimensional grid and therefore a self-consistent calculation for it is meaningless.

3.4.3.1 INCAR for Self-Consistent Run

```
SYSTEM = Gallium arsenide cluster

## Start parameter for this Run:
     ISTART    = 0              ! job     : 0-new  1-cont  2-samecut
     ICHARGE = 2                ! charge: 1-file  2-atom  10-const

## Electronic Relaxation
     ENCUT = 350 eV

## Ionic Relaxation
     IBRION = -1                ! ionic relax: 0-MD  1-quasi-New  2-CG

## DOS related value
     ISMEAR = 0                 ! -4-tet  -1-fermi  0-gaussian
     SIGMA = 0.001              ! broadening in eV
```

Figure 3.11: Parameters for self-consistent run in INCAR file.

Figure 3.11 shows the INCAR file parameters for self-consistent run. Value 2 for ICHARGE instructs the calculation to calculate the charge density in a self-consistent run. Same energy cutoff, Gaussian smearing and small smearing width as those for geometry optimization is used. IBRION = -1 denotes that there is no ionic update which means ions are not moved. The POSCAR file for this calculation is copied from the CONTCAR file of the previous geometry optimization run. KPOINTS file is also similar with the one used in geometry optimization which contains only gamma point.

3.4.3.2 INCAR for Non-Selfconsistent Run

```
   SYSTEM = Gallium arsenide cluster

## Start parameter for this Run:
        ISTART    = 0            ! job     : 0-new  1-cont  2-samecut
        ICHARGE = 11             ! charge: 1-file  2-atom  10-const

## Electronic Relaxation
        ENCUT = 350 eV
        NELMDL = -5              ! of ELM steps

## Ionic Relaxation
        IBRION = -1              ! ionic relax: 0-MD  1-quasi-New  2-CG

## DOS related value
        ISMEAR = 0               ! -4-tet  -1-fermi  0-gaussian
        SIGMA = 0.1              ! broadening in eV
```

Figure 3.12: Parameters for non-selfconsistent run in INCAR file.

Figure 3.12 shows the parameters used for non-selfconsistent run. Now, value 11 of ICHARGE determines the calculation to be non-selfconsistent. This is the value to obtain the eigenvalues (for bandstructure plots) or the DOS for a given charge density read from CHGCAR and the charge density will be kept constant during the whole run. Therefore, CHGCAR file is first copied from the self-consistent run before this calculation is started. NELMDL gives the number of non-selfconsistent steps at the beginning. This is set for the case where the self-consistent convergence is bad and thus choosing a ‘delay’ for starting the charge density update is essential. Negative value results in a delay only for the start-configuration.

3.4.3.3 KPOINTS for Non-selfconsistent and Bandstructure

The *k*-points used for bandstructrue is different from the previous run and its KPOINTS file contains strings of *k*-points as shown in Figure 3.13.

```
k-points for bandstructure L-G-X-U  K-G
     10                ! 10 intersections
Line-mode
Reciprocal
     0.500   0.500   0.500        ! L
     0.000   0.000   0.000        ! gamma

     0.000   0.000   0.000        ! gamma
     0.000   0.500   0.500        ! X

     0.000   0.500   0.500        ! X
     0.250   0.625   0.625        ! U

     0.375   0.750   0.375        ! K
     0.000   0.000   0.000        ! gamma
```

Figure 3.13: Parameters for non-selfconsistent run in KPOINTS file.

The strings of *k*-points connect the specific points of L-G-X-U and K-G of the Brillouin zone (refer Figure 3.1). The coordinates of the *k*-points are given in reciprocal mode. Value 10 in the second line instructs VASP to generate 10 *k*-points between the first and second supplied points, 10 *k*-points between the third and the fourth, and so on. The bandstructure is then plotted according to these specific *k*-points.

CHAPTER 4

RESULTS AND DISCUSSION

4.1 Simulation of Bulk Gallium Arsenide and Gallium Arsenide Dimer

As a first step, bulk gallium arsenide is calculated by using VASP for the purpose of comparison with the clusters as well as for accuracy assurance. In addition, dimmer is an excellent test system. If a pseudopotential has passed dimer and bulk calculation, one can be quite confident that the pseudopotential posseses excellent transferability. Bulk gallium arsenide is constructed according to its zinc blende structure that is in F43m space group, which follows face-centered-cubic (fcc) bravais lattice.

The geometry optimization gives the structure with lattice constant 5.632 Å. This is close to the experimental lattice constant 5.653 Å [64]. For Ga_1As_1 dimer, the approach is same as those for the clusters, which is using supercell method. The result shows the bond length of the Ga_1As_1 is 2.580 Å, which is also in good agreement to the experimental results of 2.53 Å ± 0.02 Å [12]. Density of state

(DOS) and bandstructure is further calculated for bulk gallium arsenide. The DOS and bandstructure are corresponding to each other and from both graph, the obtained bandgap value (direct bandgap) is 0.354 eV. This is lower than the experimental value 1.424 eV. It has been claimed that the reason lies the ground state emphasis of DFT and thus it underestimated the bandgap value [65]. The presence of a discontinuity in the true DFT exchange-correlation functional derivative is also the reason leading to the bandgap underestimation.

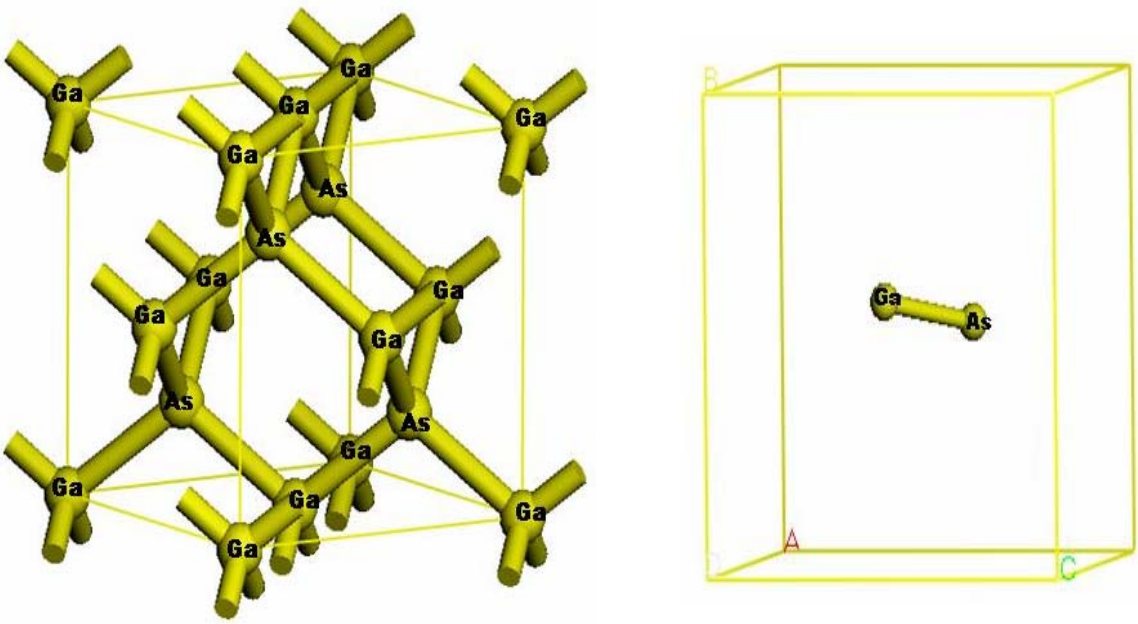

Figure 4.1: Structure of zinc blende bulk GaAs (Left). Structure of Ga_1As_1 dimer (Right).

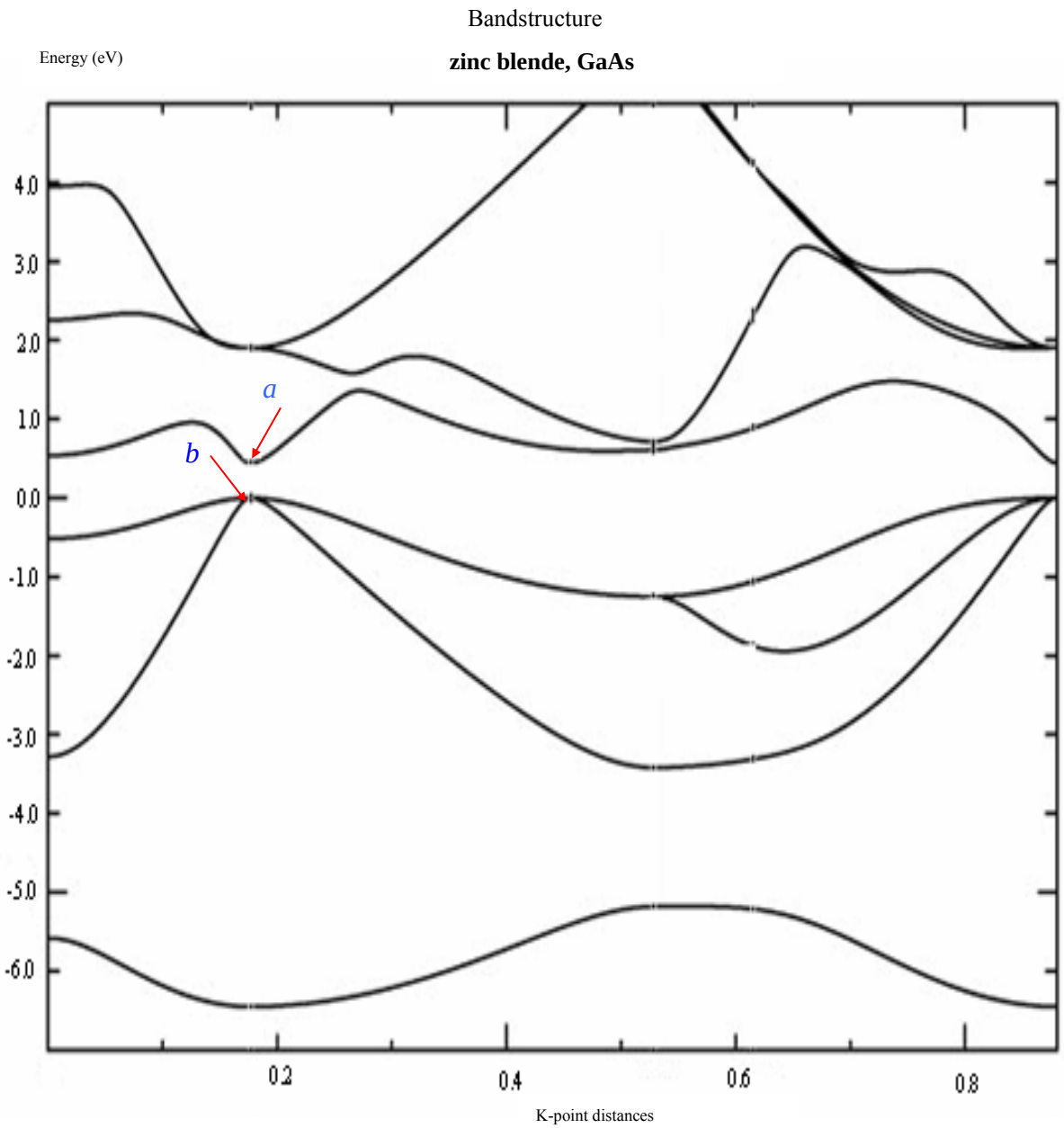

Figure 4.2: Bandstructure of bulk GaAs. Point *a* represents highest energy of valence band (band or area below *a*) while point *b* represents the lowest energy of the conduction band (band or area after *b*). Both bandstructure and DOS are corresponding to each other.

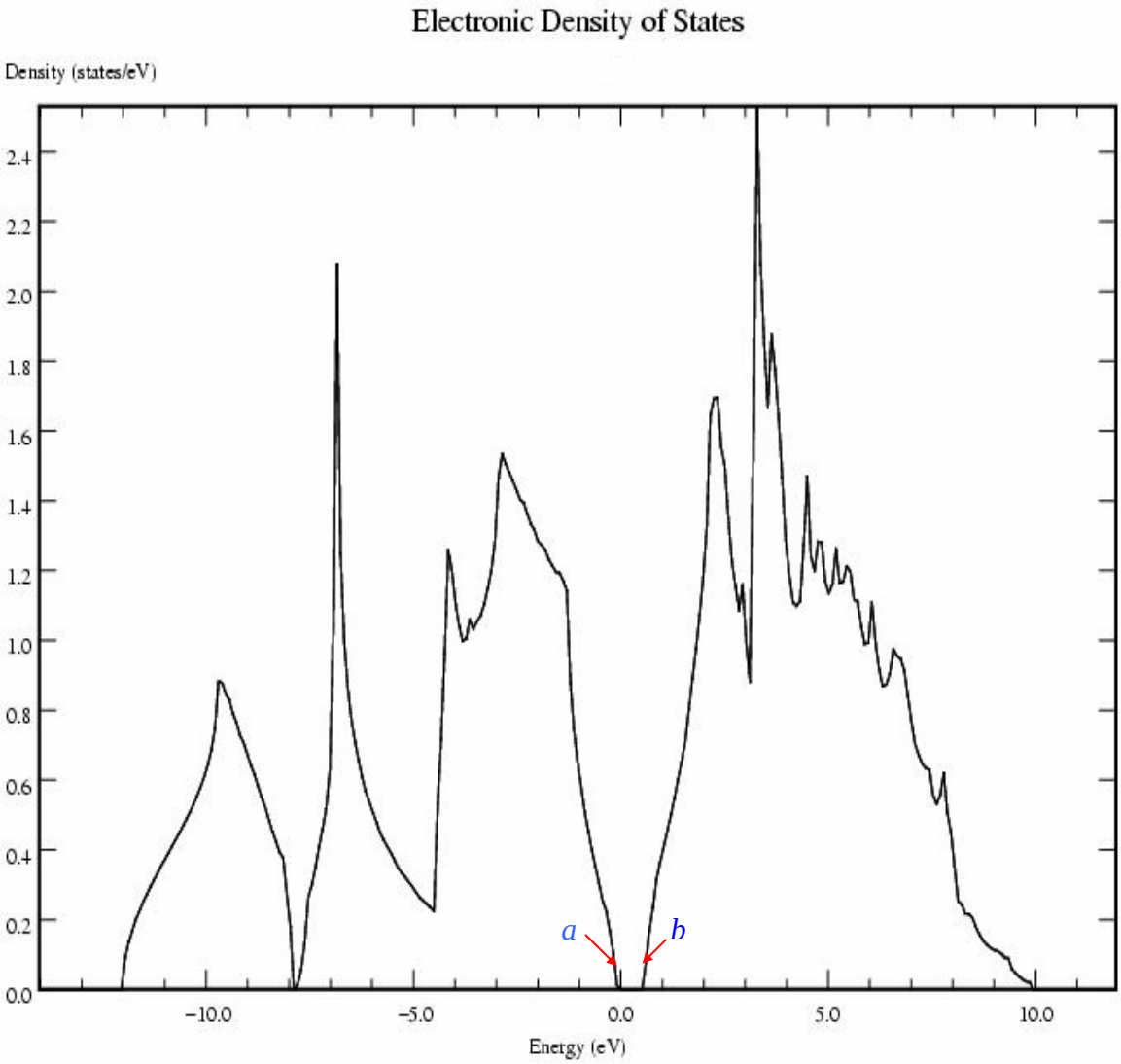

Figure 4.3: DOS of bulk GaAs. Point *a* represents highest energy of valence band (band or area below *a*) while point *b* represents the lowest energy of the conduction band (band or area after *b*). Both bandstructure and DOS are corresponding to each other.

4.2 The Effect of Size on the Electronic Structures of Gallium Arsenide Clusters

In order to compare the results for variable size, the gallium arsenide clusters are simulated by clusters with different number of gallium arsenide atom. The size would rather to be termed as the number of atoms. A bare cluster has a large number of dangling bonds on its surface, which shows strong chemical reactivity and induces an unstable condition for the cluster.

During the geometry optimization, the surface will reconstruct and eliminate dangling bonds to minimize the surface potential and consequently lead to a stable structure. Therefore, in order to maintain the regular tetrahedron bonding configuration, the cluster is terminated or passivated by hydrogen. With the presence of hydrogen atoms on the dangling bonds of the clusters, the surface tension is significantly reduced and thus has a function of stabilization.

The clusters were built from arrangement corresponding to the bulk gallium arsenide fragment. Geometry optimization was performed with conjugate gradient process and only internal parameters (atoms' position and distance) change without fluctuation of the supercell's size. Four hydrogenated gallium arsenide clusters were compared, which are $Ga_4As_4H_{12}$, $Ga_5As_6H_{16}$, $Ga_7As_6H_{16}$ and $Ga_7As_6H_{19}$.

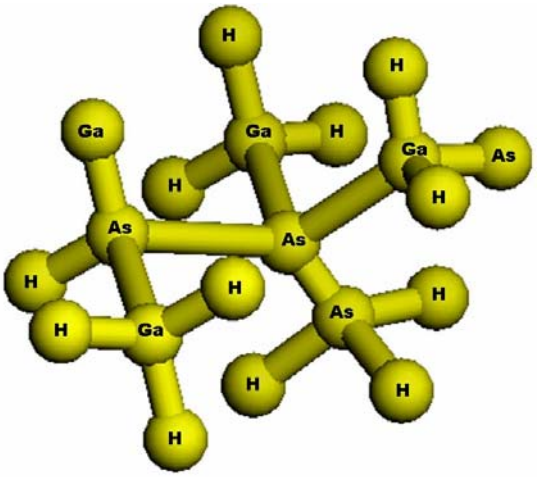

$Ga_4As_4H_{12}$

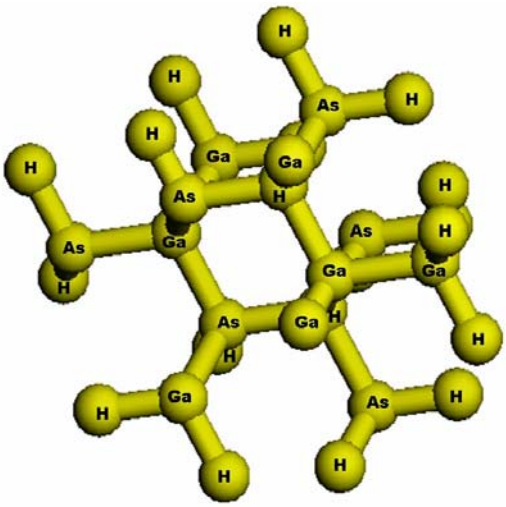

$Ga_5As_6H_{16}$

$Ga_7As_6H_{16}$

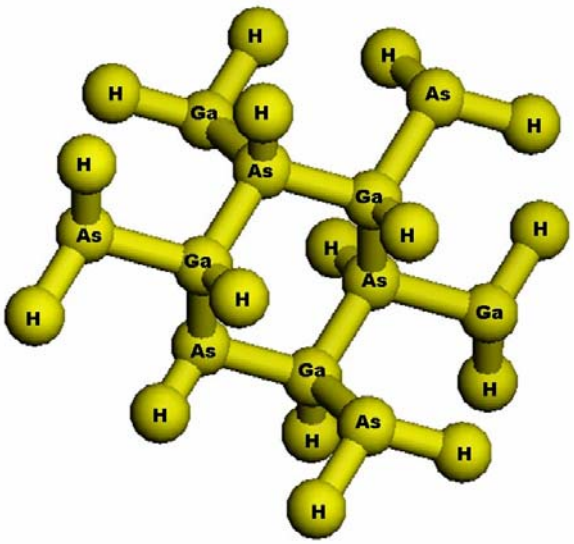

$Ga_7As_6H_{19}$

Figure 4.4: Ball and stick for hydrogenated gallium arsenide clusters, $Ga_xAs_yH_z$

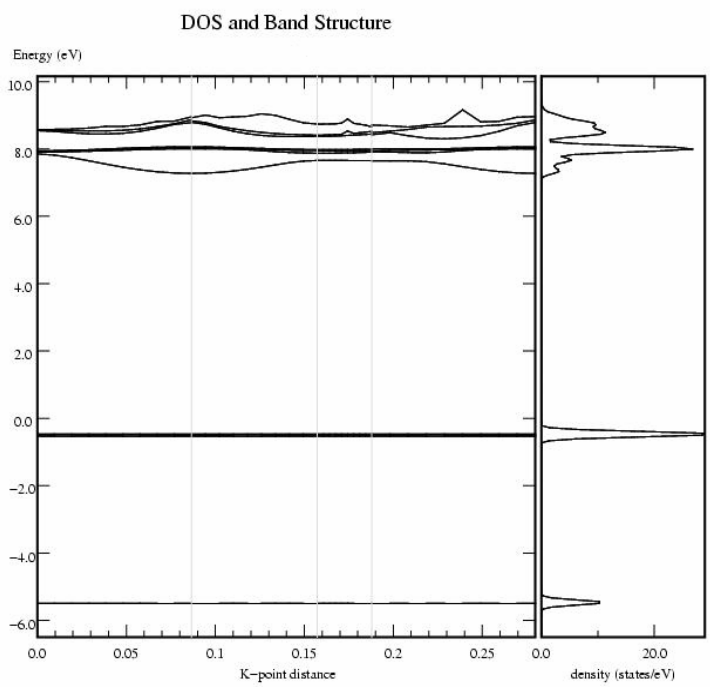

$Ga_4As_4H_{12}$

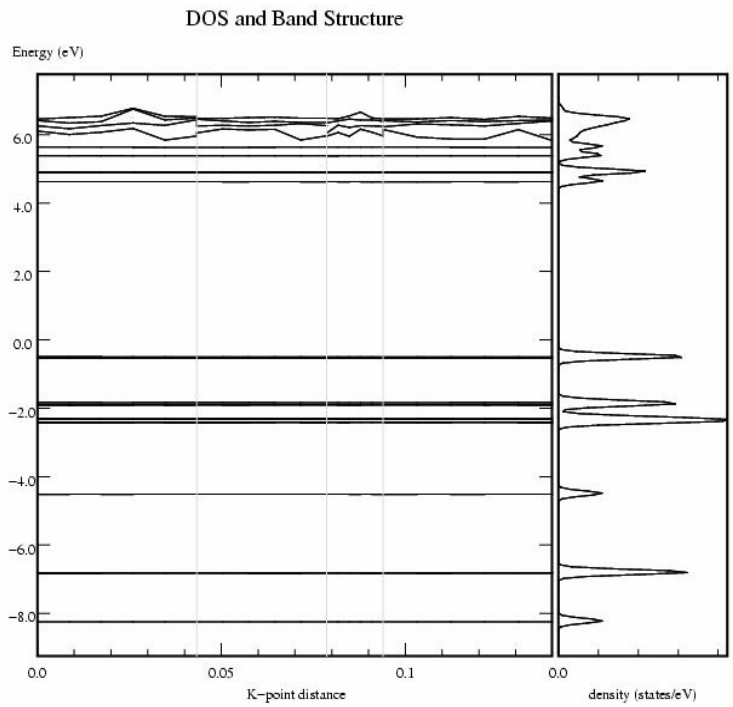

$Ga_5As_6H_{16}$

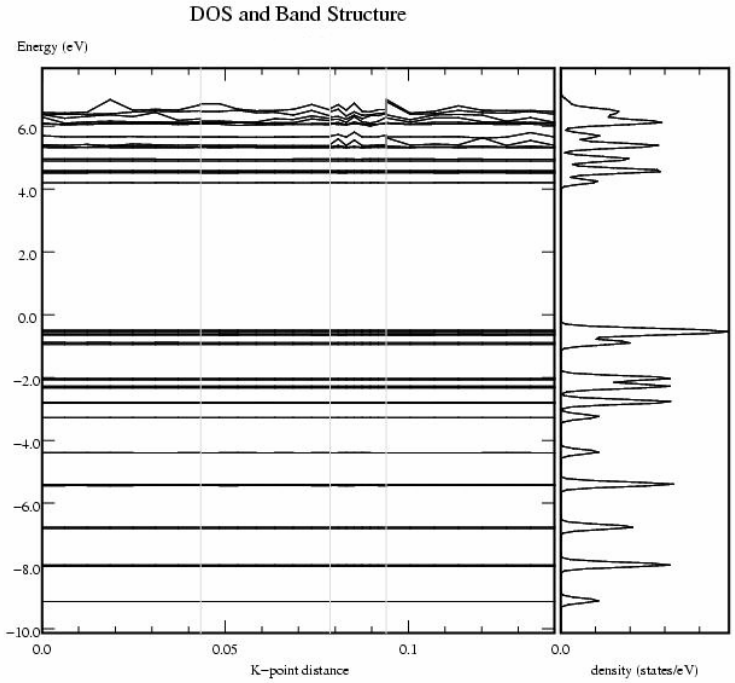

$Ga_7As_6H_{16}$

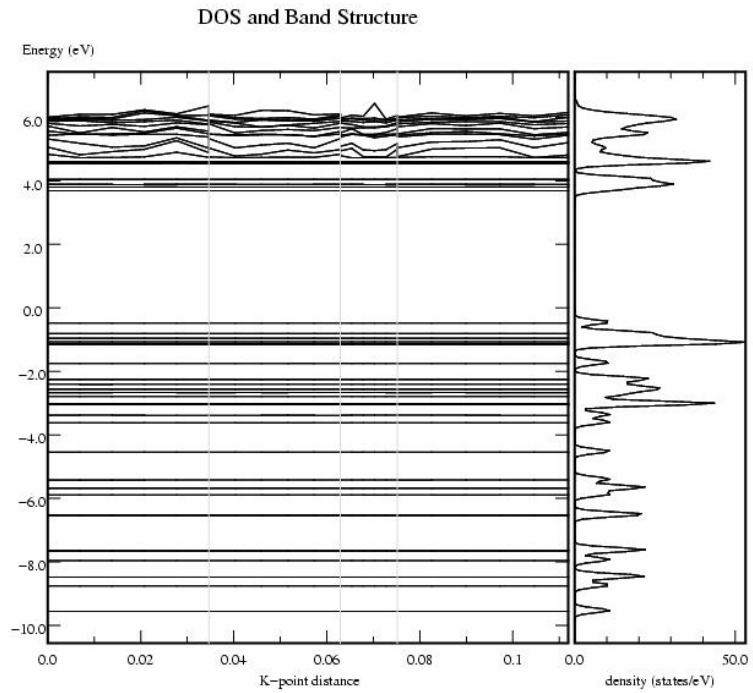

$Ga_7As_6H_{19}$

Figure 4.5: Bandstructure and DOS of hydrogenated gallium arsenide clusters, $Ga_xAs_yH_z$.

The following list the bandgap energy of each cluster obtained from the bandstructures in Figure 4.5.

Table 4.1: Bandgap energy for each of the cluster. Values in the brackets are the bandgap (eV) from Asok K. Ray et.al [87].

Total Number Of Atoms In The Clusters	$Ga_xAs_yH_z$	HOMO (eV)	LUMO (eV)	Bandgap (eV)
20	$Ga_4As_4H_{12}$	-8.20	-0.86	7.34 (7.462)
27	$Ga_5As_6H_{16}$	-6.01	-1.59	4.42 (4.584)
29	$Ga_7As_6H_{16}$	-5.23	-1.65	3.58 (3.698)
32	$Ga_7As_6H_{19}$	-3.89	-1.97	1.92 (2.057)

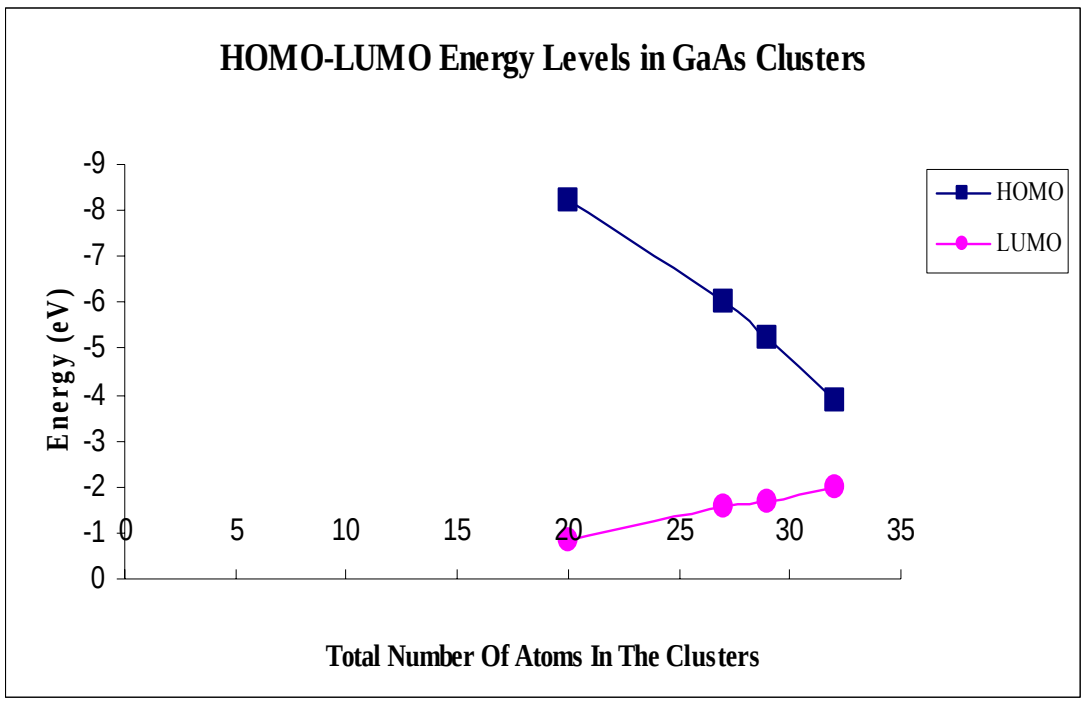

Figure 4.6: Band shift related to the cluster size. The upper line is HOMO energy value while lower line is LUMO energy value.

The surface atoms of hydrogenated gallium arsenide clusters do not give any new surface geometry formation other than that existing in the clusters as shown in the Figure 4.3. However, the clusters have encountered contraction where the bonds are shortened compare to their initial structures. For these four hydrogenated gallium arsenide clusters, the bond lengths of Ga-As are in the range of 2.413 Å to 2.448 Å, which is approaching the Ga-As bond length of bulk gallium arsenide 2.448 Å [66].

Table 4.1 shows the highest occupied molecular orbital (HOMO) energy, lowest unoccupied molecular orbital (LUMO) energy and the bandgap of each $Ga_xAs_yH_z$. The bandgap was obtained by the difference between HOMO energy and LUMO energy ($E_{LUMO} - E_{HOMO}$). Therefore, the bandgap can also be referred to as HOMO – LUMO gap. From the bandstructure spectra shown above, the energy levels have been subtracted the Fermi energy so that the Fermi level defines as zero energy. As a result, the HOMO and LUMO energy levels in the Figure 4.5 are different from the values listed in Table 4.1. Therefore, in the bandstructure spectra, HOMO is the first energy level under zero which is Fermi level whereas LUMO is the first energy level above the Fermi level.

From the graph above, it is obvious that the HOMO-LUMO gap decreases as the number of atoms increases. In other words, the HOMO-LUMO gap is inversely proportional to the size of the clusters. Figure 4.6 also shows the size related LUMO-band shifts in the nanoclusters which are consistent with HOMO-band shifts. The bandgap is getting narrower as the cluster size increases. This is consistent with the theoretical trend for the bandgap for various sizes of quantum dots as a result of the quantum confinement effects in the bandgap of gallium arsenide nanostructures, which can be depicted by the quantum confinement dictum:“the bandgap increases as the size decreases”.

The HOMO-LUMO band-shift results in the red-shifting of the bandgap. From Figure 4.5, it is clear that the correlation between the bandgap and the number of atom is not linear. This indicates that the bandgap also depends on other factors which among them are the symmetry of the cluster and the specific transition involved. The important implication of Figure 4.6 is the relation between the cluster size and the bandgap as discussed above. Theoretical bandgaps of the four clusters ($Ga_4As_4H_{12}$, $Ga_5As_6H_{16}$, $Ga_7As_6H_{16}$ and $Ga_7As_6H_{19}$) are shown in the bracket in Table 4.1. As discussed earlier, the calculated bandgaps are underestimated compared to the theoretical data.

In comparison, it is obvious that the bandgap for each of the cluster is much larger than the bandgap of bulk gallium arsenide since cluster is much smaller than the bohr radius of bulk gallium arsenide is 12nm [67]. For bulk gallium arsenide, there are optical activities due to direct bandgap.

Therefore, for hydrogenated gallium arsenide cluster, the light emission can be controlled by altering the size of the cluster which results in different color of light. As a result, it can be observed that the DOS of cluster is different from the one of bulk. The DOS is not continuous but is in discrete form.

Hence, it is referred to as discrete energy spectrum instead of DOS. In conjunction with the DOS changing, bandstructure has also become a straight vertical line in consistent with the discrete spectrum, which is a result of single-point calculation. Although the calculated values are not in good agreement with the experimental values (since bandgap is underestimated by DFT), the results show

qualitative trends and relativity of the electronic properties of gallium arsenide nanostructures.

4.3 The Effect of Shape on the Electronic Structures of Gallium Arsenide Clusters

In this section, the shape effect to the electronic structures of gallium arsenide clusters is discussed. Unlike the hydrogenated gallium arsenide clusters studied previously, gallium arsenide clusters used for the study of shape effect are bare clusters without any passivation with other elements.

After the energy minimization algorithm; conjugate gradient (CG) and simulated annealing (SA) the ground state structures for Ga_xAs_y ($x+y\leq15$) as shown in Figure 4.7 were obtained. From an overall view, it could be observed that the structures of the optimized bare gallium arsenide clusters are different from each other and they have their own geometries. These optimized geometrical structures will be discussed in the next section and the discussion of electronic structures will be made next.

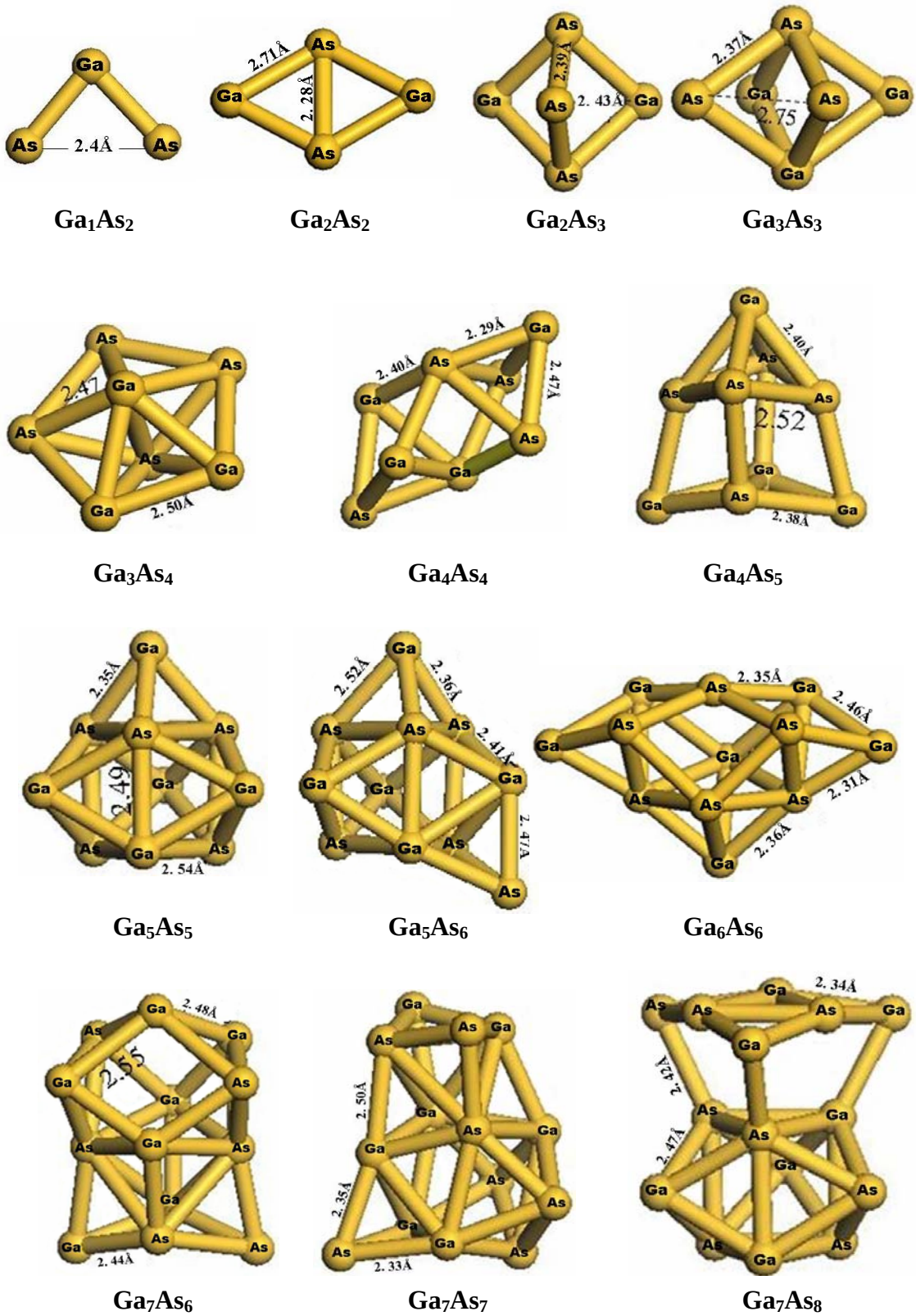

Ga_1As_2 **Ga_2As_2** **Ga_2As_3** **Ga_3As_3**

Ga_3As_4 **Ga_4As_4** **Ga_4As_5**

Ga_5As_5 **Ga_5As_6** **Ga_6As_6**

Ga_7As_6 **Ga_7As_7** **Ga_7As_8**

Figure 4.7 : Lowest energy geometries for the Ga_xAs_y ($x + y \leq 15$)

4.3.1 Optimized Geometry Structure

Table 4.2: The configurations and point group for each of the gallium arsenide clusters, Ga_xAs_y

Ga_xAs_y	Configurations
Ga_1As_2	Triangle
Ga_2As_2	Planar rhombus
Ga_2As_3	Trigonal bipyramid
Ga_3As_3	Tetragonal bipyramid
Ga_3As_4	Pentagonal bipyramid
Ga_4As_4	Bicapped octahedral
Ga_4As_5	Capped Rhombic
Ga_5As_5	Tetracapped trigonal prism
Ga_5As_6	Capped trigonal prism
Ga_6As_6	Hexacapped trigonal prism
Ga_7As_6	Tricapped trigonal prisma additional rhombus capped on edge the prism
Ga_7As_7	Two distorted rhombus with five atoms ring
Ga_7As_8	Tricapped trigonal antiprism

The ground state geometry structure of each gallium arsenide clusters, Ga_xAs_y ($x + y \leq 15$) is discussed in the following:

1. Ga_1As_1

   In section 4.1, the ground state structure of Ga_1As_1 was shown with a bond length of 2.580 Å which is close the experimental result is 2.53 Å ± 0.02 Å [12] .

2. Ga_1As_2

   The equilibrium geometries of the trimers Ga_1As_2 are shown in Figure 4.7. The equilibrium geomerties are bent. The clusters have a ground state $^2B_2$ within the point group symmetry C_{2v}. In Ga_1As_2 the bond angle is 56.3^o . The small bond angle in Ga_1As_2 is due to the short As-As bond (2.4 Å).

3. Ga_2As_2

   The ground state of Ga_2As_2 is the ^1A_g state and is in the form of a planar rhombus in D_{2h} symmetry. The values for the Ga-As bond length is 2.71 Å but for the As-As bond length our value of 2.28 Å is in good agreement with the value of other researchers [7,8,68,69].

4. Ga_2As_3

   The ground state of Ga_2As_3 is $^2A_2^{''}$ in D_{3h} symmetry. The equilibrium geometry is a trigonal bipyramid composed of a 3-arsenic basal ring and 2 apical gallium atoms. The As-As bond length is 2.62 Å, compared to 2.39 Å for the As_3 cluster in its ground state in an equilateral triangle form. The

rather loose bonding between the basal arsenic atoms in the Ga_2As_3 bipyramid is compensated by the strong bonds between the basal arsenic atoms and the apical gallium atoms.

5. Ga_3As_3

   Ga_3As_3 has a similar structure to Ga_2As_3, which is tetragonal bipyramid structure in the point group of D_{4h}. The As-As bond length is 2.37 Å and the distance of unbonded atoms at the pyramid square base is 2.75 Å. The two apex atoms having coordination number (bonds) of 4 are holding the square together and they are 2.71 Å apart.

6. Ga_3As_4

   The most stable geometries of the Ga_3As_4 were obtained by relaxing pentagonal bipyramids in C_s symmetry. The optimized bond lengths within the plane of pentagon have a value of 2.50 Å. The apex atoms have five equivalent bonds to the atoms in the pentagon plane with the length of 2.47 Å, which is a very unusual geometrical arrangement. This is an almost close-packed compressed structure with the apex atoms only 2.52 Å apart.

7. Ga_4As_4

   Ground state of Ga_4As_4 has a distorted bicapped octahedral structure with the point group of C_s. As the name of the structure, Ga_4As_4 has two octahedron capping two opposite faces.

8. Ga_4As_5

   Ga_4As_5 has a ground state structure of capped stack rhombic with the point group of C_{2v}. This structure can be viewed as two stacked distorted rhombic with an additional atom capped on top.

9. Ga_5As_5

   A tetracapped trigonal prism (C_{3v}) ground state structure was obtained for Ga_5As_5. This structure contains a 9 atom gallium arsenide clusters subunit where there are three rectangular faces are capped together forming a 9-atom of tricapped trigonal prism (TTP) structure with D_{3h} point group. One atom is capped on top of the triangular faces of the TTP to give this Ga_5As_5 structure with overall C_{3v} symmetry.

10. Ga_5As_6

    For $x + y = 11$, C_s structure was obtained as the ground state structure, which is also a capped trigonal prism. This structure is similar to the C_{3v} structure of Ga_5As_5 but with one additional atom capped at one prism face.

11. Ga_6As_6

    Ground state structure obtained for Ga_6As_6 is a hexacapped trigonal prism with C_{2v} symmetry. This is a structure where two capping atoms are added to the ground state of Ga_5As_5.

12. Ga_7As_6

    The most stable structure for 13 atoms GaAs cluster is C_{2v} which can be described as a distorted tricapped trigonal prism with an additional rhombus capped on one edge of the prism.

13. Ga_7As_7

    The ground state structure obtained in this research for Ga7As7 is of C_s symmetry. This structure exhibits stacking sequence of two distorted rhombus, one five atoms ring and an atom on top.

14. Ga_7As_8

    A TTP fused with a tricapped trigonal antiprism on top is found for Ga_7As_8 as a stable structure. This structure is in the symmetry point group of C_{3v}.

It is very obvious that the tetrahedral bond structure of bulk gallium arsenide is broken and the stable structures of the clusters have entirely new geometries and symmetries. The atoms bond in such ways to get the favorable lowest energy geometries. It could be observed that almost all the structures have their atoms on the surface and the atoms are bonded. Scanning each of the clusters, it can be seen that each cluster can be made from the previous cluster by attaching a gallium arsenide atom at an appropriate bonding site. These bonding sites are typically face- or edge-capped sites.

For instance, Ga_2As_2 can be constructed from triangular Ga_1As_2 by adding a Ga atom along an edge to obtain a planar rhombus. If a third edge cap is added and the structure twisted slightly to make all caps equivalent, the trigonal bipyramid of Ga_2As_3 can be yielded. The ground state of Ga_3As_3 can be derived from Ga_2As_3 by

adding an atom along the triangular edges and form a square. Similar to Ga_3As_4 forming the pentagon from the square by adding an atom. For $2 \leq x + y \leq 7$, the clusters can be constructed by edge-capping. For $x + y \geq 10$, the Ga_xAs_y clusters are developed from TTP and face-capping growth mode is preferred. For example Ga_5As_5 is made by capping an atom on the triangular face. Ga_5As_6, Ga_6As_6 and Ga_7As_8 have obvious TTP structure inside with more atoms is inserted around them.

Ground state structures of Ga_1As_2 – Ga_2As_2 discussed above agree well with others' theoretical structures [4,6,8,9,10,24,70,71,72,73,74,75,76,77] which had been confirmed experimentally. The experimental results obtained by infrared and raman spectra [78] are in good agreement with the ab-initio calculated vibrational frequencies, including their relative intensities. As the cluster size increases, it becomes more difficult to find its lowest-energy structure theoretically as the number of possible geometries increases exponentially. For instances, distorted tricapped octahedron (C_s) and distorted TTP (C_{2v}(II)) [5] has been proposed as stable structures for Ga_4As_5, tetracapped octahedron (T_d) for Ga_5As_5 [6], another capping trigonal prism isomer (C_{2v}) for Ga_5As_6 [79], and more isomers for Ga_6As_6,Ga_7As_6,Ga_7As_7 and Ga_7As_8 [9].

4.3.2 Electronic Structure

Figure 4.8 – 4.21 shows the DOS and bandstructure of the corresponding 14 ground state gallium arsenide cluster structures shown in Figure 4.7. DOS and bandstructure are displayed together since they are related as discussed in the section above. Binding energy and electron affinity of each of the clusters were also studied.

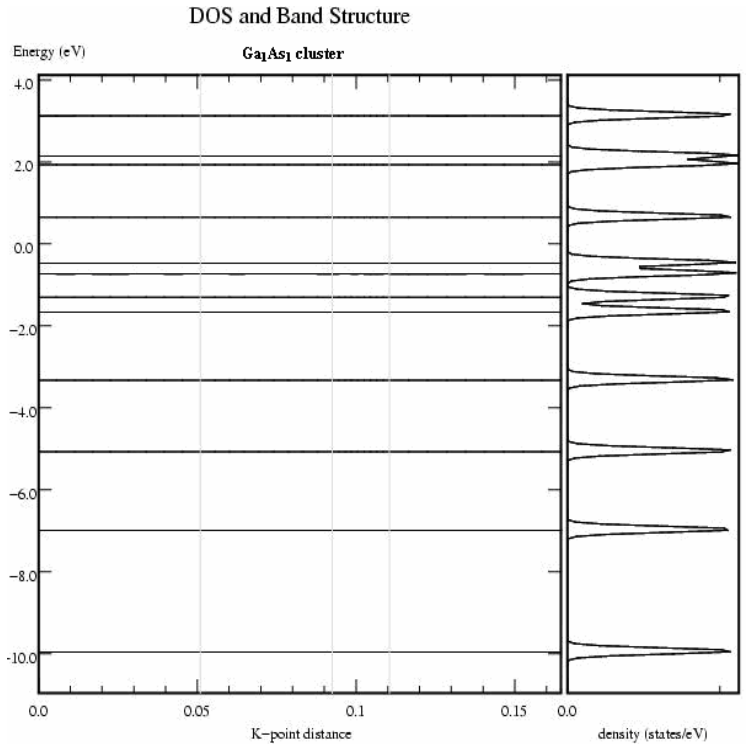

Figure 4.8: DOS and bandstructure of Ga_1As_1 cluster

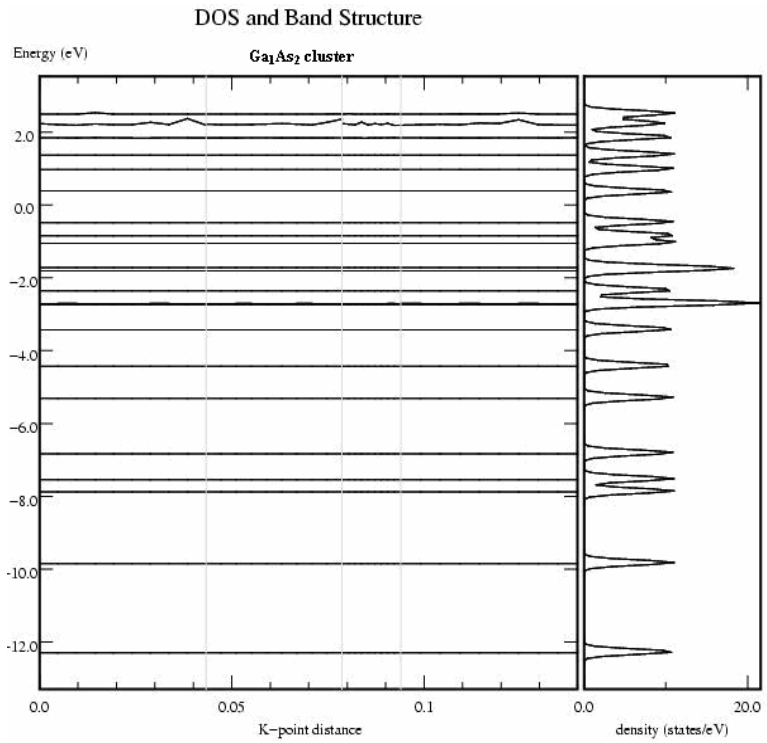

Figure 4.9: DOS and bandstructure of Ga_1As_2 cluster

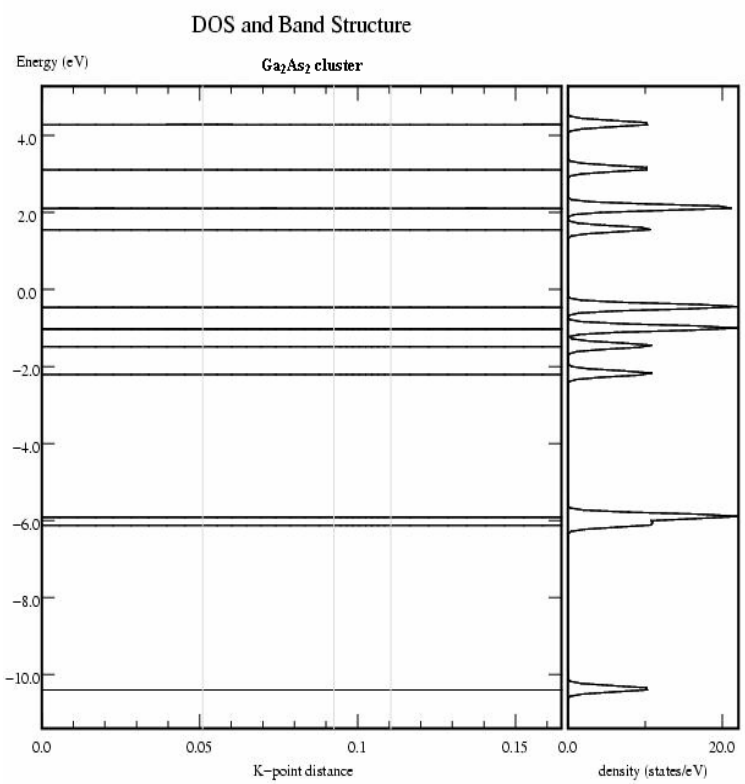

Figure 4.10: DOS and bandstructure of Ga_2As_2 cluster

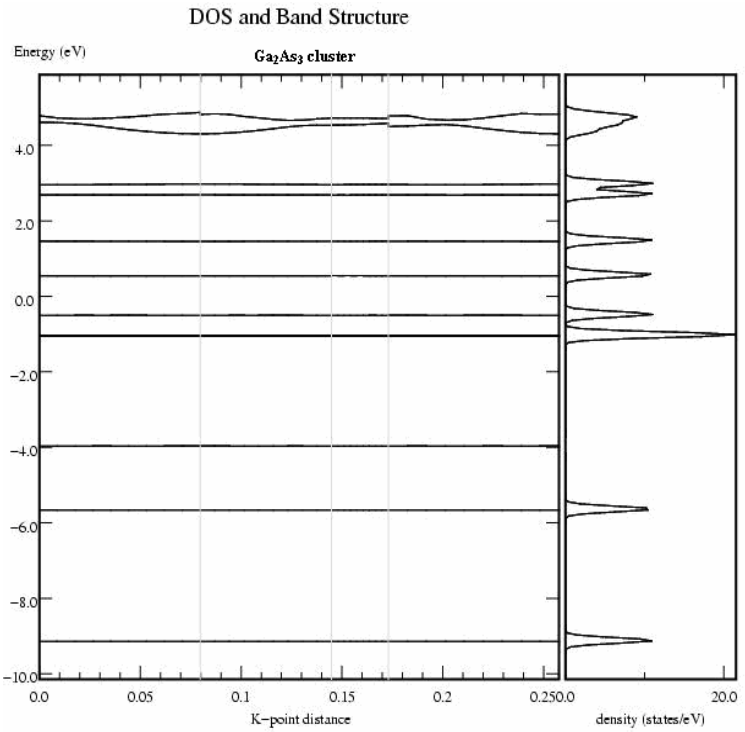

Figure 4.11: DOS and bandstructure of Ga_2As_3 cluster

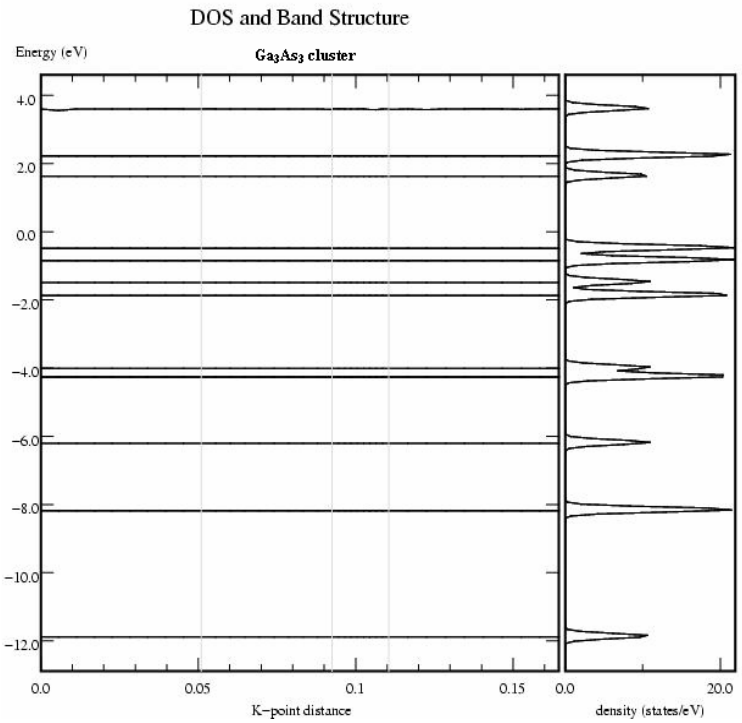

Figure 4.12: DOS and bandstructure of Ga_3As_3 cluster

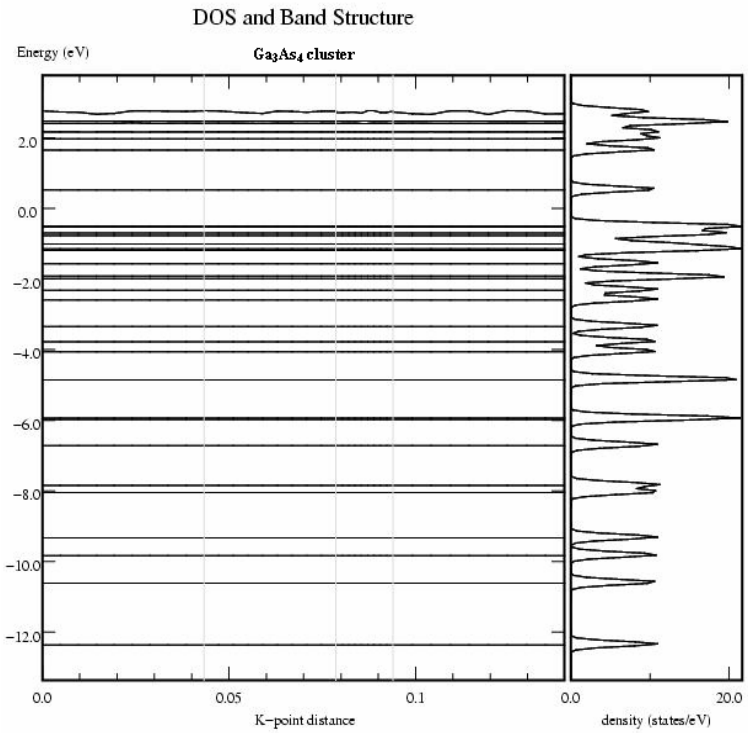

Figure 4.13: DOS and bandstructure of Ga_3As_4 cluster

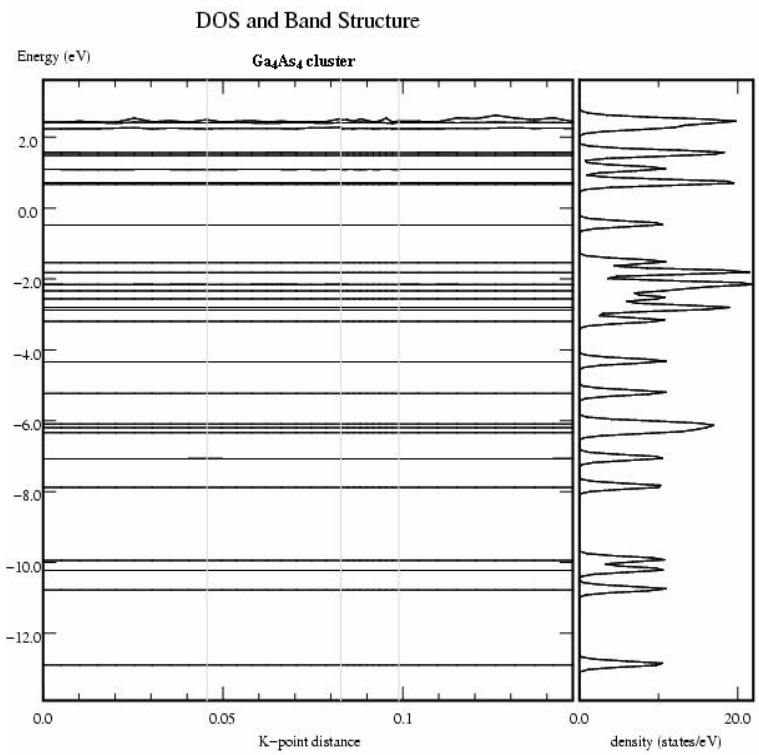

Figure 4.14: DOS and bandstructure of Ga_4As_4 cluster

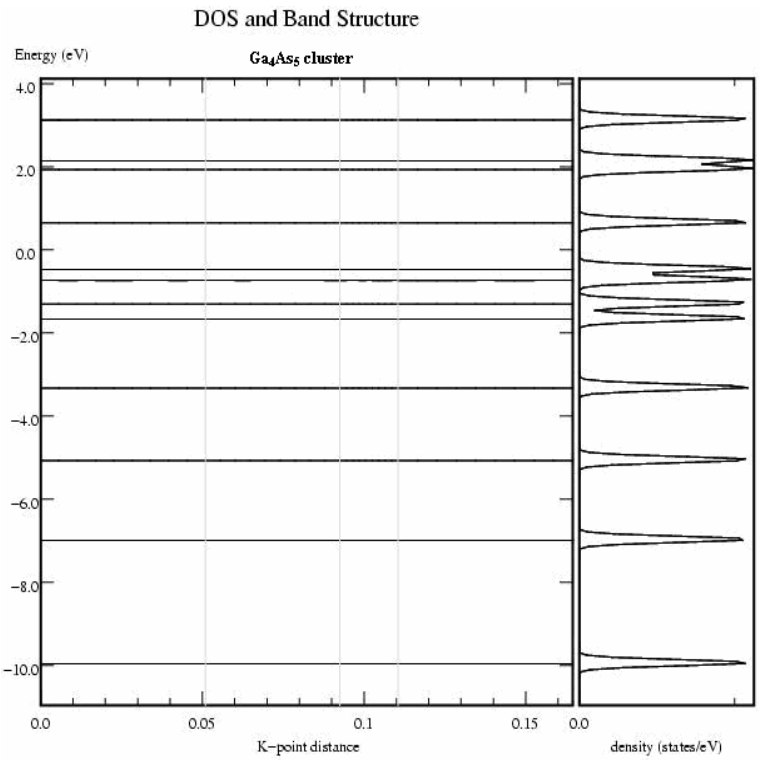

Figure 4.15: DOS and bandstructure of Ga_4As_5 cluster

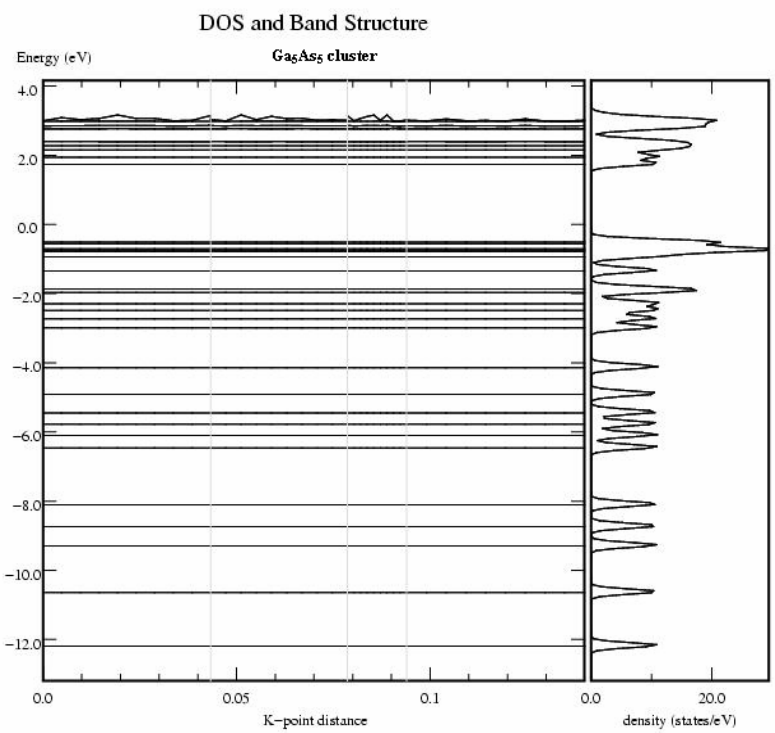

Figure 4.16: DOS and bandstructure of Ga_5As_5 cluster

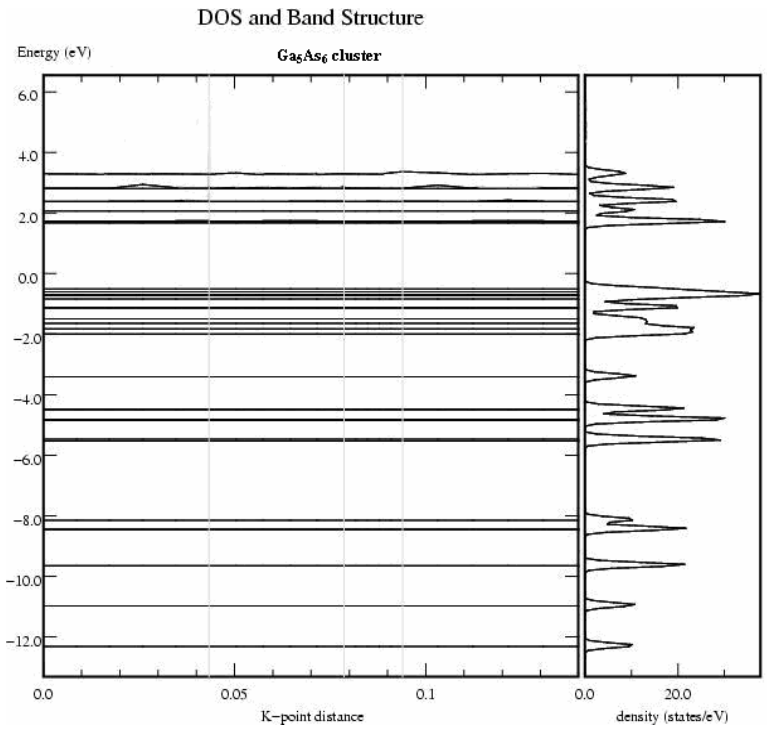

Figure 4.17: DOS and bandstructure of Ga_5As_6 cluster

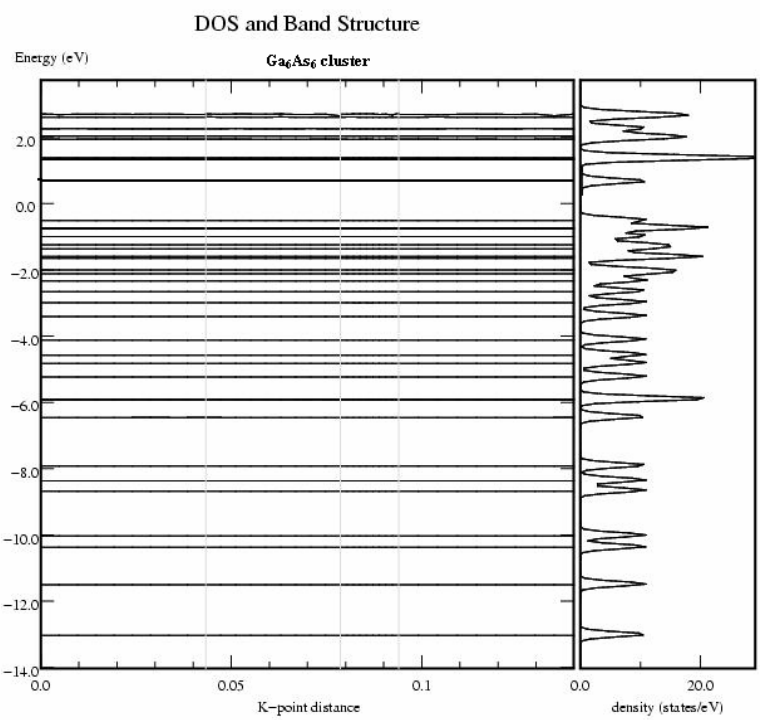

Figure 4.18: DOS and bandstructure of Ga_6As_6 cluster

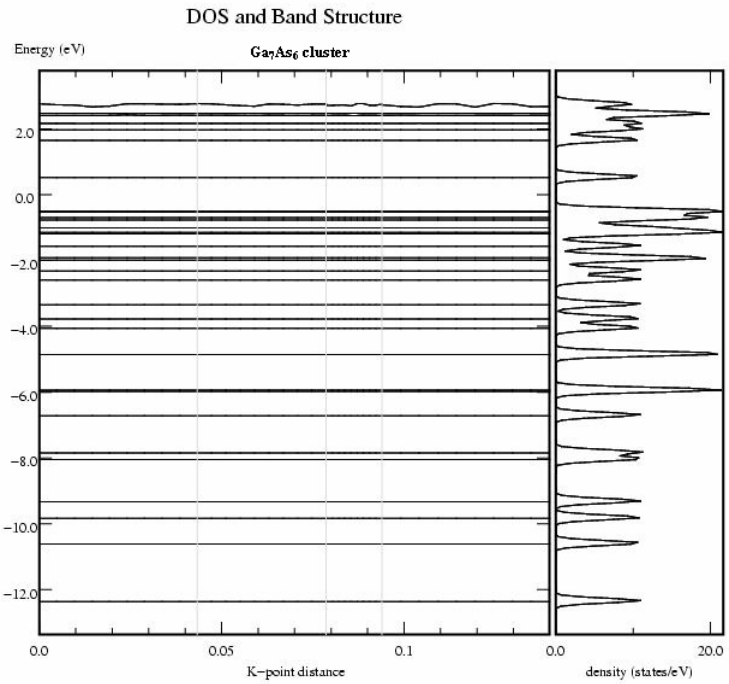

Figure 4.19: DOS and bandstructure of Ga_7As_6 cluster

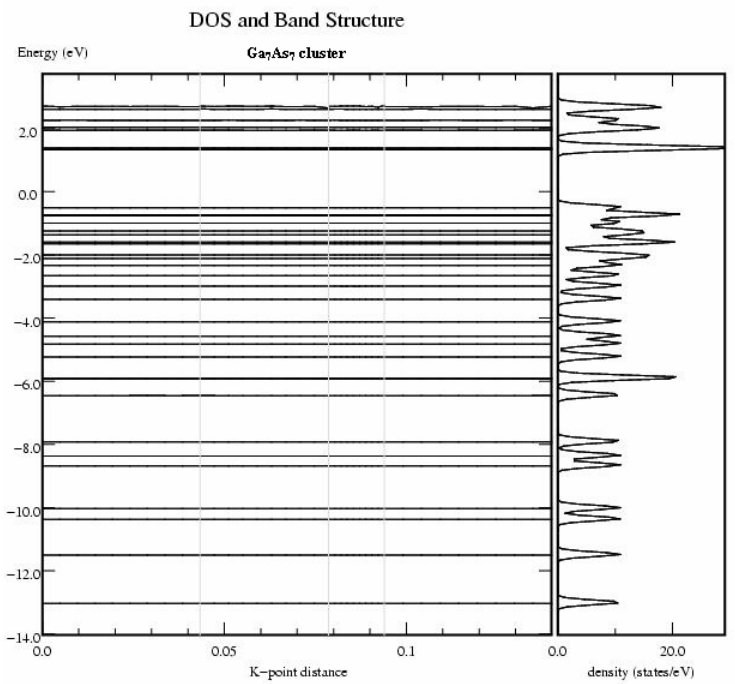

Figure 4.20: DOS and bandstructure of Ga_7As_7 cluster

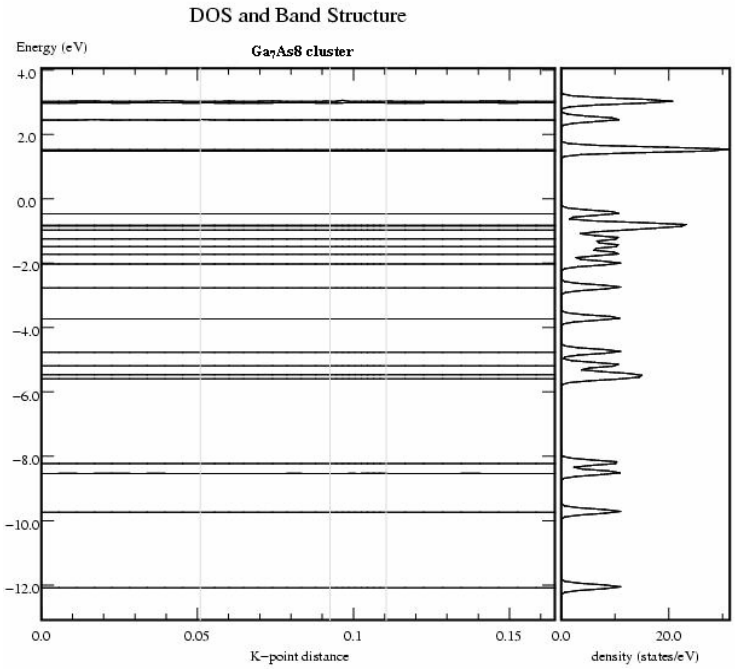

Figure 4.21: DOS and bandstructure of Ga_7As_8 cluster

Table 4.3: Energy level (HOMO and LUMO) as well as bandgap value of each Ga_xAs_y clusters, ($x + y \leq 15$)

Ga_xAs_y	HOMO (eV)	LUMO (eV)	Bandgap (eV)
Ga_1As_1	-4.329	-3.949	0.38
Ga_1As_2	-4.473	-4.063	0.41
Ga_2As_2	-4.356	-3.196	1.16
Ga_2As_3	-4.783	-3.693	1.09
Ga_3As_3	-4.325	-2.395	1.93
Ga_3As_4	-4.294	-3.834	0.46
Ga_4As_4	-4.392	-3.272	1.12
Ga_4As_5	-4.211	-3.801	0.41
Ga_5As_5	-4.584	-2.854	1.73
Ga_5As_6	-4.205	-3.365	0.84
Ga_6As_6	-4.117	-3.067	1.05
Ga_7As_6	-4.287	-3.307	0.98
Ga_7As_7	-4.311	-3.141	1.17
Ga_7As_8	-4.195	-3.235	0.96

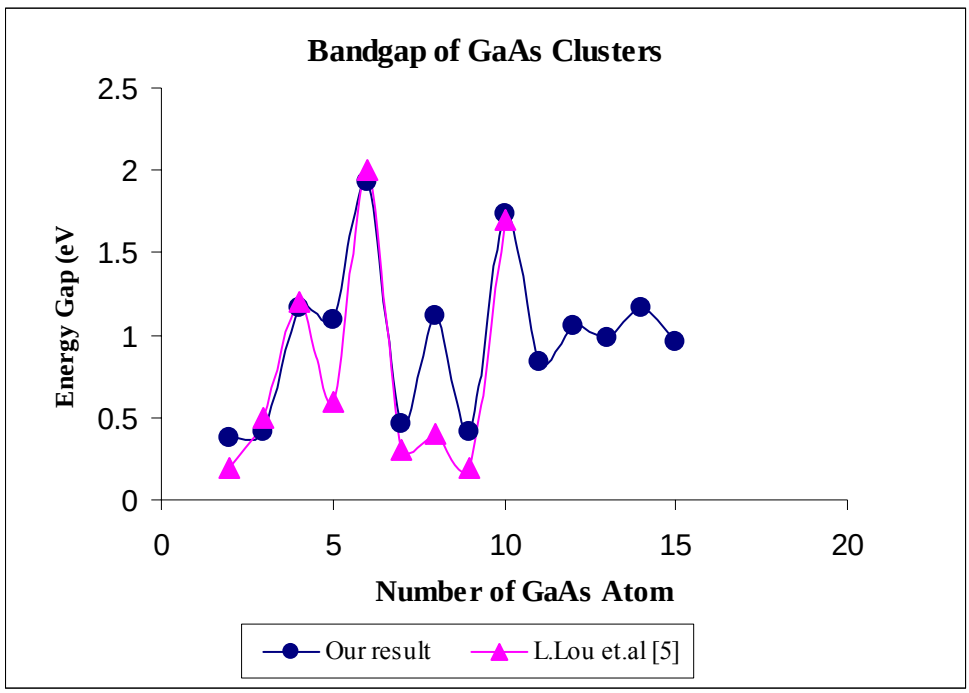

Figure 4.22: Graph of bandgap versus number of GaAs atom in the cluster and comparison between other researcher's results [5].

Table 4.4: Binding energy per atom of each gallium arsenide cluster, Ga_xAs_y ($x + y \leq 15$). The binding energies are not corrected with zero potential energies. Reseacher's data are from reference *a*[5], *b*[6] , *c*[12], *d*[10], *e*[80] and *f* [9].

Ga_xAs_y	Binding Energy Per Atom (eV/atom)	Researcher's Data (eV/atom)
Ga_1As_1	1.87	1.08^a, 2.46^b, 2.06 ± 0.05^c, 2.206^d
Ga_1As_2	2.14	1.93^a, 2.31^b, 0.767^d
Ga_2As_2	2.25	2.22^a, 2.38^b, 0.572^d
Ga_2As_3	2.28	2.40^a, 2.87^b, 0.387^d, 2.95^f
Ga_3As_3	2.31	2.43^a, 2.56^b, 0.367^d, 2.233^e, 3.29^f
Ga_3As_4	2.37	2.43^a, 2.52^b, 0.334^d
Ga_4As_4	2.45	2.54^a, 2.55^b, 0.673^d, 2.379^e, 3.35^f
Ga_4As_5	2.48	2.54^a, 2.63^b
Ga_5As_5	2.59	2.65^a, 2.71^b, 2.373^e, 3.58^f
Ga_5As_6	2.61	2.393^e, 3.59^f
Ga_6As_6	2.69	
Ga_7As_6	2.70	
Ga_7As_7	2.73	2.574^e
Ga_7As_8	2.78	

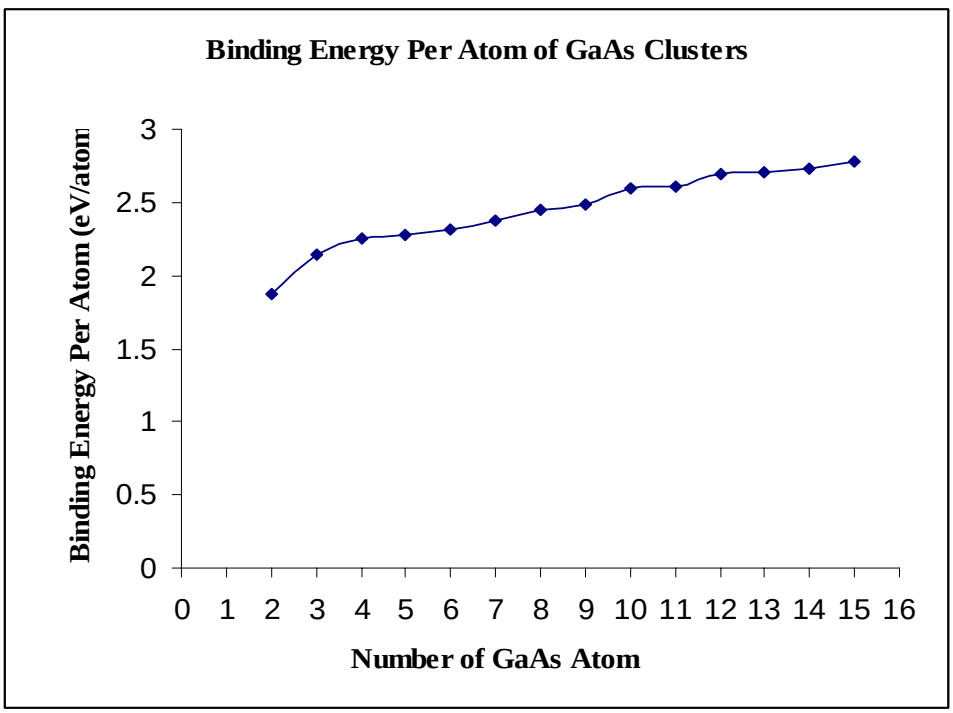

Figure 4.23: Graph of binding energy per atom of GaAs clusters.

Table 4.5: Second-difference energies and electron affinity of each gallium arsenide cluster, Ga_xAs_y ($x + y \leq 15$). Researcher's data are from reference *a*[5], *b*[6], *c*[10] and *d*[9].

Ga_xAs_y	Second-difference Energies (eV)	Electron Affinity (eV)	
		Calculation	Researcher's Data
Ga_1As_1	0.56	1.85	1.9^a, 1.9^b, 1.24^c
Ga_1As_2	-0.04	2.17	2.1^a, 1.9^b, 1.31^c
Ga_2As_2	0.28	1.63	1.8^a, 1.7^b, 1.40^c, 1.7^d
Ga_2As_3	-0.11	2.41	2.7^a, 2.5^b, 1.83^c
Ga_3As_3	0.03	1.72	1.6^a, 1.5^b, 0.81^c, 1.8^d
Ga_3As_4	-1.32	2.69	2.9^a, 2.5^b, 2.71^c
Ga_4As_4	1.57	2.27	2.8^a, 2.4^b, 1.46^c, 3.3^d
Ga_4As_5	-1.65	3.24	3.5^a, 3.1^b
Ga_5As_5	0.96	2.37	2.4^a, 2.0^b, 2.2^d
Ga_5As_6	-0.46	2.56	
Ga_6As_6	0.51	2.13	2.1^d
Ga_7As_6	-0.27	2.33	
Ga_7As_7	0.22	2.21	
Ga_7As_8	-0.58	2.71	

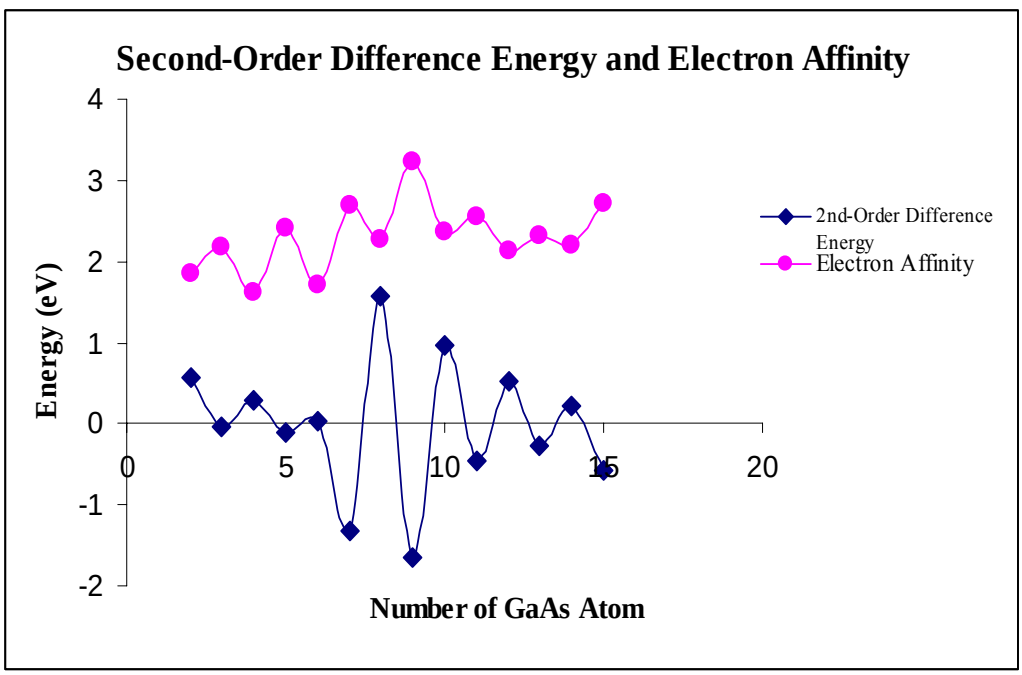

Figure 4.24: Graph of second-difference energies and electron affinity of each Ga_xAs_y ($x + y \leq 15$) corresponding to the table above.

Figure 4.8 – 4.21 shows the bandstructure and energy spectrum of each of the gallium arsenide cluster from number of atoms 2 to 15. Obviously similar to the $Ga_xAs_yH_z$ discussed previously, the energy levels of each cluster are discrete depicting the effect of size and quantum confinement. The corresponding HOMO and LUMO energy levels as well as the band gap resulted from the HOMO-LUMO difference is listed in Table 4.3.

The bandgaps of those optimized gallium arsenide clusters do not have a trend as those for the hydrogenated gallium arsenide clusters, as shown in Figure 4.22. Instead, they have uneven bandgap values and the data point is up and down. Ga_2As_2, Ga_2As_3, Ga_3As_3, Ga_4As_4, Ga_5As_5, Ga_6As_6 and Ga_7As_7 a have very large bandgap values which are above 1.0 eV. Ga_1As_1 has the lowest bandgap among all the clusters. Nevertheless, this smallest bandgap is still larger than the bulk gallium arsenide bandgap (0.354 eV obtained in this research), indicating the effects of quantum confinement in the small clusters. These bandgap values have a good agreement with other researchers' result. As shown in Figure 4.22, the bandgap values calculated in this research are very close to the results obtained by L. Lou et.al [5].

Figure 4.23 shows the graph of the binding energies per atom of all clusters. The energy values shown are not zero-point energy (ZPE) corrected. Binding energy depicts the energy required to remove an atom from the cluster. Binding energy per atom is given in terms of the energies of the free gallium arsenide atom and the cluster:

$$E_B = (nE_{Ga\text{-}atom} + nE_{As\text{-}atom}) - (E_{cluster}) \qquad (4.1)$$

Where E(Ga), E(As) and E(cluster) are the energies of an isolated Ga atom, a As atom and the cluster, respectively. An agreement is found between the calculated and the theoretical binding energy as shown in Table 4.4. The binding energy per atom rose rapidly from Ga_1As_1 to Ga_1As_2 and the slope gradually decreases until it is nearly horizontal. The size dependence of binding energy is the consequence of the cluster growth patterns. The very small clusters ($x + y \geq 2$-7) tend to have compact polyhedral geometries, which allow them to maximize their binding energy effectively [81]. It has been shown that intermediate size clusters ($x + y \geq 8$-15) grow as elongated structures. From Table 4.4 shows that the binding energy per atom increase as the size of the clusters increases. It is due to the fact that constituent atoms in larger clusters have more neighbors resulting in strong interactions.

Binding energy graph can be used to study the magic sizes of the clusters. However, the phenomenon is not obvious and hardly noticeable from the binding energy graph (Figure 4.23). A better way to show the relative local stability of the gallium arsenide cluster is through the use of the second-order difference binding energy ($^2\Delta_{x+y}$) as a function of cluster size as shown in Figure 4.11. This energy is obtained by:

$$^2\Delta_{x+y} = E_{(x+y)+1} + E_{(x+y)-1} - 2E_{(x+y)} \tag{4.2}$$

Notable peaks were observed for Ga_xAs_y clusters with Ga_1As_1, Ga_2As_2, Ga_3As_3, Ga_4As_4, Ga_5As_5, Ga_6As_6 and Ga_7As_7 indicating that they are relatively more stable in comparison with clusters of [(x+y)+1] and [(x+y)-1] atoms. If the highest occupied electronic subshell is filled in a cluster of (x + y) atoms, and the next available subshell is separated by a sizable energy gap, the cluster energy will jump from $E_{(x+y)}$ to $E_{(x+y)+1}$, which gives rise to peak indicating the cluster of size n is very stable. This result has proved the validity of the cluster stability obtained from binding energy graph.

Another method to determine the relative stability is through electron affinity. Electron affinity is a measure of the energy change when an electron is added to a neutral atom to form a negative ion. Thus it is calculated by:

$$EA = E_N - E_{N+1} = E_{(\text{neutral})} - E_{(\text{anion})} = E(\text{Ga}_x\text{As}_y) - \text{E}(Ga_xAs_y^-) \quad (4.3)$$

where N is the number of electrons of the system or cluster. The electron affinity calculated here is vertical electron affinity which is equal to the energy difference of the cluster Ga_xAs_y and its anion $Ga_xAs_y^-$ in the equilibrium geometry of the Ga_xAs_y. The result shows smaller electron affinities are yielded for Ga_1As_1, Ga_2As_2, Ga_3As_3, Ga_4As_4, Ga_5As_5, Ga_6As_6 and Ga_7As_7. Conversely, Ga_1As_2, Ga_2As_3, Ga_3As_4, Ga_4As_5, Ga_5As_6, Ga_7As_6 and Ga_7As_8 have larger electron affinities than their adjacent clusters.

This result is in opposite trend with the second-order difference energies. The higher peaks for the second-order difference energies are those lower peaks for the electron affinities (Ga_1As_1, Ga_2As_2, Ga_3As_3, Ga_4As_4, Ga_5As_5, Ga_6As_6 and Ga_7As_7). The gallium arsenide clusters with smaller electron affinities are more stable than their neighbors. The Ga_xAs_y clusters have shown that the electronic affinity (EA) of gallium arsenide clusters with the number of atoms (x + y); the even-numbered clusters tend to have smaller EA and the odd-numbered clusters have larger EA [82].

The vertical electron affinity is in correspondence with the LUMO energy level. Referring to Table 4.5, it can be observed that the clusters with higher LUMO energy level have smaller vertical electron affinity and vice versa. Those with higher LUMO are the highly stable clusters. Ga_1As_2, Ga_2As_3, and Ga_3As_4 and Ga_4As_5 have lower LUMO level and therefore its vertical electron affinity is higher. Adiabatic electron affinity [10] which is the energy difference of Ga_xAs_y and its corresponding

anion, $Ga_xAs_y^-$ had given a much smaller electron affinity value for Ga_1As_2 and Ga_2As_3. Gallium Arsenide cluster with 5 atoms, Ga_2As_3 has lower adiabatic electron affinity than Ga_3As_4 which has additional bonding in its anion contributing to a fairly high electron affinity [10]. Most photoelectron spectroscopy corresponds to the adiabatic electron affinity. Nonetheless, vertical electron affinity yielded in this research gave a good stability trend for gallium arsenide clusters. The goal here is to understand the trends in the electron affinities as a function of the size of the clusters.

From the graphs, it can be concluded that the stable clusters obtained are Ga_1As_1, Ga_2As_2, Ga_3As_3, Ga_4As_4, Ga_5As_5, Ga_6As_6 and Ga_7As_7. Stability of Ga_3As_3 is more obvious in the electron affinity graph than in the second-order difference graph. These stability studies contribute to the "magic number" of the gallium arsenide cluster where the highly stable clusters are the magic clusters.

The bandgap of the gallium arsenide clusters can be related with their stability discussed above. It can be noted that the clusters with large bandgap have high stability. This is especially obvious for Ga_xAs_y with Ga_2As_2, Ga_3As_3, Ga_4As_4, Ga_5As_5, Ga_6As_6 and Ga_7As_7, for which these are the magic clusters. However, this is not the case for Ga_1As_1 and Ga_2As_3, where Ga_1As_1 which is more stable has comparative lower bandgap and while larger bandgap for Ga_2As_3 which are less stable. Therefore, the relation between the stability and bandgap can be applied for clusters with the number of atom after 5. The interpretation could be made such that the ground state stability was derived by having significant bonding which splits the HOMO and LUMO as much as possible. An ambiguous relation can also be made with the geometries of the gallium arsenide clusters. From Figure 4.7, it could be observed that Ga_xAs_y with Ga_2As_3, Ga_3As_3, Ga_3As_4, Ga_5As_5 and Ga_6As_6 have more compact, nearly spherical and higher symmetrical geometries. Ga_1As_2 and Ga_2As_2 for which their structures are more open and flat have small bandgap.

4.4 Effect of Hydrogen and Reconstructed Surface to Electronic Structures

The results of hydrogenated and stable ground state gallium arsenide clusters could be compared as in Table 4.6. The bandgap values for pristine gallium arsenide clusters similar to those in Figure 4.3 with hydrogen atoms eliminated and without optimization, were also included in the table. Only gallium arsenide clusters Ga_xAs_y with (x +y) = 8, 11 and 13 were taken for comparison.

Table 4.6: Bandgap (eV) comparison of bare non-optimized tetrahedral GaAs clusters, hydrogenated GaAs clusters and surface reconstructed GaAs clusters.

Number of atom, x, y, and z	Bandgap (eV)		
	Ga_xAs_y (non-optimized)	$Ga_xAs_yH_z$	Ga_xAs_y (surface reconstructed)
(x = 4), (y = 4), (z = 12)	0.48	7.34	0.92
(x = 5), (y = 6), (z = 16)	0.65	4.42	1.23
(x = 7), (y = 6), (z = 16)	0.31	3.58	0.98
(x = 7), (y = 6), (z = 19)	0.31	1.92	0.98

The bandgap values for 3 types of gallium arsenide cluster show obvious difference between each other, where hydrogenated gallium clusters have the largest bandgap followed by optimized gallium clusters and lastly non-optimized gallium arsenide clusters. For unpassivated and non-optmized gallium clusters having tetrahedron bonding as bulk gallium , the bandgaps were found to be very small that they are even smaller than the bandgap of bulk gallium arsenide (0.354 eV). These clusters tend to be metallic. This phenomenon is due to the surface state of the unpassivated gallium arsenide clusters that have dangling bonds at the surface. It is a consequence of the missing neighbors at the surface. Each dangling bond contributes a partially filled surface state and these states are located in the energy gap around the Fermi level. This has been well demonstrated for the surface of bulk gallium

arsenide using a number of methods including high resolution electron energy loss spectroscopy [83,84] and photoemission [85], which show that surface states mostly fill the bandgap of the unpassivated gallium arsenide surface. Therefore, it results in a much smaller bandgap.

When the clusters with non-relaxed surface atoms and very low average coordination numbers, as described above is relaxed and optimized, dissimilar geometries are likely to be produced, in which the tetrahedron bonds symmetry of bulk gallium arsenide have been broken. The surface atoms (dangling bonds) contributing surface tension provide a large driving force to form more compact structures provided the resulting strain energy is not too high.

Therefore the dangling atoms reconstructed by creating bonds with other atoms and this leads to a stable configurations with large portion of atoms are on the surface. The dangling bonds and thus the surface states near the Fermi level are significantly reduced via the reconstruction. New states appear due to the geometry reconstruction at the outer shell and generally the occupied states shift toward more negative side while the virtual (unoccupied) states shift towards more positive side. As a result, the clusters have larger bandgap compared to the pristine cluster with high density of dangling bonds. However, the reconstruction does not eliminate the dangling bonds completely. Hence, the reconstructed gallium arsenide surface still contains a large amount of dangling bonds and shows chemical reactivity which is somewhat smaller compared to the bulk. This is the reason of the random energy gap values which is independent of the cluster size.

The results for gallium arsenide clusters passivated with hydrogen are entirely different from the two types of bare clusters discussed previously. The passivated gallium arsenide clusters do not show low energy transitions associated

with surface states but show much broader bandgaps just as expected for particles in this extremely small size range. The dangling bonds on the surface which exist in the bare cluster have now been eliminated or passivated by hydrogen atoms which complete the four coordination number of gallium arsenide atoms. The surface atoms do not give any new surface geometry formation and retain their original shape. Since all the dangling bonds of the surface atoms are passivated, no surface state is introduced within the energy gap.

The bandgap depends only on the size effect, rather than on the surface effect. The dependence of electronic structure variations on the size effect has important consequences especially on the optical properties which are controllable with size. The bandgap increases as the size decreases, implying that radiation or emission from quantum dot "blue-shifted" reflecting the fact that electron must fall a greater distance in terms of energy (from conduction band to valence band) and thus produce radiation of a shorter wavelength. The size-dependent emission frequency gives rise to a very important development of optical devices in which the output wavelength and therefore the output color can be controlled precisely by controlling the size of the quantum dot. Passivation with oxygen has further consequences for the particles [86]. Surface passivation and absorption with different passivants are likely to give different impact on the electronic structures.

The discussions above gave an evidence that the electronic structures of gallium arsenide clusters could be influenced by plenty of factors. The bandgap is found to be strongly dependent on the factors as below:

i.) Surface passivation
ii.) Surface reconstruction
iii.) Surface orientation
iv.) Passivation with species other than hydrogen

CHAPTER 5

SUMMARY AND CONCLUSION

5.1 Summary and Conclusion

The electronic structure of gallium arsenide clusters have been presented. The electronic structures were simulated by using VASP, a simulation package which is based on the principle of density functional theory (DFT). In this research, structural properties of gallium arsenide clusters were also studied.

Simulation of bulk gallium arsenide has shown that the density functional theory underestimates the bandgap value. It has been claimed that the result is due to the discontinuity in the DFT exchange-correlation functional derivatives. The simulation shows the bandgap of 0.354 eV for gallium arsenide, which is 1.07 eV lower than the experimental value, 1.424 eV. However, geometry optimization done by DFT has produced quite accurate structures. Although DFT has underestimated the bandgap, it still give excellent qualitative results for insights on nanostructures. The bandgap underestimation does not demonstrate the failure of DFT since it is a

ground state theory and the bandgap is an excited state property. DFT produces good energy and excellent structure while scaling favorably with electron number and hence it is feasible on larger systems compared to other methods. Besides, it offers notable balance between accuracy and computational cost in which it produces accurate results with relatively smaller basis sets in comparison with other method such as Hartree-Fock . The success of DFT is also due to its availability of increasingly accurate approximations to the exchange-correlation energy. It is able to give the quantitative understanding of materials properties from the fundamental laws of quantum mechanics.

The simulation of hydrogenated gallium arsenide clusters was done to study the size effect to electronic structures of the clusters. Bandgap and density of states (DOS) were studied particularly. The energy quantization is shown by the discrete spectrum of DOS. It is called discrete energy spectrum instead of density of states which has continuous density. It shows the evolution of electronic structures of the clusters in comparison to bulk solids. From the graph of bandgap versus number of gallium arsenide atom, it is found that the bandgap increases with the decrement of the cluster sizes in term of the number of gallium arsenide atoms. This dependence of bandgap to the size of cluster is in agreement with the theory of nanostructures.

The lowest-energy structures of gallium arsenide clusters, Ga_xAs_y ($x + y \leq 15$) have been studied. The ground state structure of each cluster has entirely different structure with the tetrahedral bond structure of bulk gallium arsenide. Unlike hydrogenated gallium arsenide cluster, the bandgap values for these ground state clusters do not have a particular trend either increasing or decreasing. Instead, the bandgap values are up and down. Binding energy, second-order difference energy, and electron affinity were also studied for the ground state gallium arsenide clusters. These three analyses could show the local relative stability of the gallium arsenide cluster. The results show that Ga_1As_1, Ga_2As_2, Ga_3As_3, Ga_4As_4, Ga_5As_5,

Ga_6As_6 and Ga_7As_7 are more stable in comparison with their neighbors. When the stability was related to the bandgap, it was found that the clusters with larger bandgap (>1.0 eV) have higher stability, such as Ga_2As_2, Ga_3As_3, Ga_4As_4, Ga_5As_5, Ga_6As_6 and Ga_7As_7. However, it is found that Ga_2As_3 cluster has lower stability although it has a bandgap larger than 1.0 eV. The Ga_1As_1 is more stable and it has the smallest bandgap with 0.38 eV. Nonetheless, it is still larger than the bulk bandgap value (0.354 eV).

Comparing the hydrogenated gallium arsenide clusters with the bare ground state gallium arsenide clusters, it has been observed that the former have much larger bandgap in comparison with the latter. Another simulation results has showed that for the unrelaxed gallium arsenide clusters with tetrahedron bonds extracted from bulk gallium arsenide, their bandgaps are very small that they are even smaller than the bulk bandgap value and is approximately zero. This smaller bandgap of bare gallium arsenide clusters compared to the fully passivated gallium arsenide clusters is due to the dangling bonds. The dangling bonds introduce extra states in the energy gap near Fermi level which reduces the bandgap.

From the results obtained, it could be concluded that gallium arsenide clusters in nano-size have novel electronic structures that differ from the bulk gallium arsenide. The electronic structures of the gallium arsenide clusters can be affected by the surface reconstruction and also the surface passivations. Therefore, the bandgap of the clusters can be controlled by manipulating their size and shapes. These properties of clusters have contributed to the unique attributes of the novel transistors such as single electron transistor (SET). The objectives of this research have been achieved and this could be a good foundation for further research, for instance the study the electron transport in SET.

5.2 Suggestions

Some suggestions are given in the following to improve the research. These are the improvement in bandgap accuracy and computational time.

5.2.1 Improvement of the Bandgap Accuracy

Since DFT underestimates the bandgap value in semiconductor, other approximation could be taken to improve the accuracy. For example, Green's function and the screened Coulomb interaction approximation have been applied as the correction to DFT bandgaps [88]. Besides this, Quantum Monte Carlo (QMC) approach for calculating electronic structures would give more accurate results for the bandgap. QMC is an important and complementary alternative to density functional theory when performing computational electronic structure calculations in which high accuracy is required. The method has many attractive features for probing the electronic structure of real atom, molecules and solids. In particular, it is a genuine many-body theory with a natural and explicit description of electron correlation which gives consistent, highly-accurate results while at the same time exhibiting favorable (cubic or better) scaling of computational cost with system size. The most important characteristics and advantages of the QMC methodology can be summarized as follows:

(a) it gives a direct and accurate wave-function-based treatment of quantum many-body effects.

(b) it is a very general approach, applicable to solids and molecules and able to calculate almost any ground-state expectation value, including energies and static correlation functions.

(c) the N^3 scaling of the computational cost is very favorable when compared with other correlated wave-function methods. N is the number of particles. In contrast, Monte Carlo simulations for the ground state of many-body systems scale as N^3 so that they can be applied to sufficiently large systems to allow extrapolation to the bulk limit.

(d) it has the significant computational advantages of easily achieved scalability on parallel architectures and low storage requirements.

(e) the diffusion monte carlo (DMC) method does not suffer from the basis set errors inherent in other correlated wave-function methods.

5.2.2. Improvement of the Computation Time

Ab-initio calculations are accurate but computationally expensive. The representation of structures by unit cells is the reason leads to redundancies within the high dimensional search space. To shorten the computation time, more high power computation units (CPUs) are needed. This problem can be solved by parallel computing, which is the simultaneous execution of the same task on multiple processors in order to obtain results faster. A problem can be divided into smaller task and broken down to a series of instructions. These instructions from each task execute simultaneously on different CPUs.

Computer cluster is a group of tightly coupled computers that work together closely so that in many respects they can be viewed as though they are a single computer. The components of a cluster are commonly connected to each other through fast local area networks. The cluster built can be categorized as high-performance cluster (HPC). HPC with nodes running Linux as the open system (OS) and free software to implement the parallelism is often referred to as a Beowulf cluster.

To test the performance of the parallelization, two factors were studied, which are speedup and efficiency. Speedup refers to how much a parallel algorithm is faster than a corresponding sequential algorithm. It is defined by the following formula:

$$S_N = \frac{T_1}{T_N} \quad , \quad 1 \leq S_N \leq N$$

where N is the number of processors, T_1 is the execution time of the sequential algorithm, and T_p is the execution time of the parallel algorithm with p processors [89]. Ideal speedup is $S_N = N$, which is called linear speedup. Efficiency is a performance metric estimating how well-utilized the processors are in solving the problem compared to how much effort is wasted in communication and synchronization. It is defined as:

$$E_N = \frac{S_N}{N} \quad , \quad 0 \leq E_N \leq 1$$

Algorithms with linear speedup and algorithms running on a single processor have an efficiency of 1.

Table 5.1: Execution time, speedup and efficiency of VASP using parallel computing [90].

Number of CPU	Execution Time (s)	Speedup	Efficiency
1	308.447	1	1
2	180.798	1.706031	0.853016
3	131.688	2.342256	0.780752
4	109.984	2.804472	0.701118
5	92.549	3.332797	0.666559
6	80.901	3.812648	0.635441
7	73.709	4.184659	0.597808
8	68.259	4.518774	0.564847
9	65.806	4.687217	0.520802
10	61.958	4.978324	0.497832
11	57.473	5.366816	0.487892

Figure 5.1 and 5.2 show a simple performance benchmark of VASP running at 2 to 11 CPUs. It is obvious that the execution time for the parallel calculation reduces as the number of CPU increases (refer to Table 5.1).

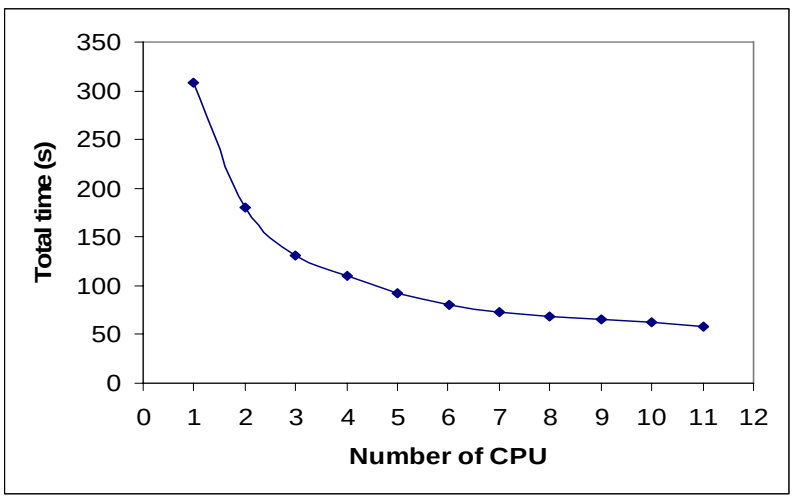

Figure 5.1: Graph of total time used for completing a parallel calculation versus the number of CPU.

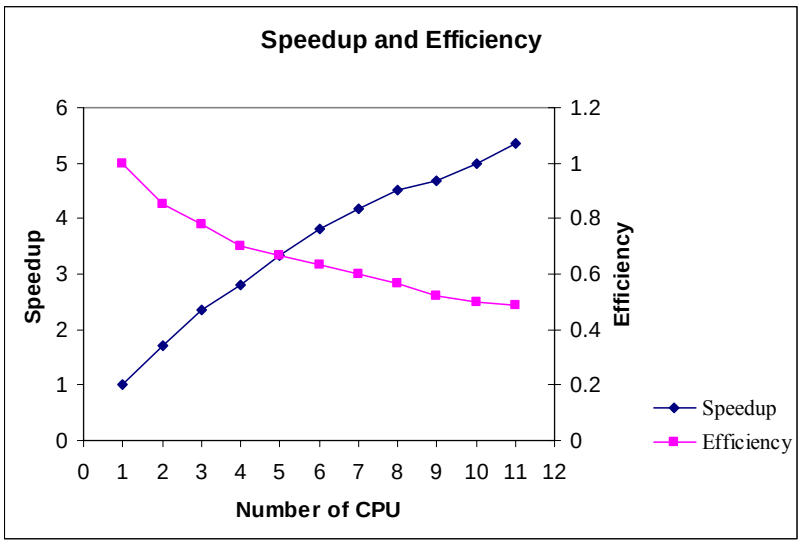

Figure 5.2: Graph of speedup and efficiency vs number of CPU.

From the graph, it can be observed that the speedup is not linear. For 11 CPUs, the speedup is 5.4 times faster than the sequential algorithm. Both speedup and efficiency trends show the decreasing of the speedup and efficiency as the number of CPU increases. This is owing to the communications between the CPUs are getting more massive when the number of CPU increases.

REFERENCES

[1] S.H. Yang, D.A. Drabold, J.B. Adams, A. Sachdev. Stability, structural transformation and reactivity of Ga_{13} clusters. *Phys. Rev. B*. 2000. 61(11): 7277-7290.

[2] H.K. Quek, Y.P. Feng, C.K. Ong. Tight binding molecular dynamics studies of Ga_mAs_n and Al_mAs_n clusters. *Zeitschrift Für Physik D*: Atoms, Molecules and Clusters. 1997. 42(4): 309-317.

[3] Y.P. Feng, C.K. Ong, H.C. Poon, D. Tomanek. Tight binding molecular dynamics simulation of semiconductor alloy: Cluster, surfaces and defects. *J. Phys. Condens. Matter*. 1997. 9(21): 4345.

[4] K.M. Song, A.K. Ray, P.K. Khowash. On the electronic structure of GaAs clusters. *J. Phys. B*: Atomic, Molecular and Optical Physics. 1994. 27(8): 1637-1648.

[5] L. Lou, L.Wang, L.P.F. Chibante, R.T. Laaksonen, P. Nordlander, R.E. Smalley. Electronic structure of small GaAs clusters. *J. Chem. Phys*. 1991. 94(12): 8015.

[6] L. Lou, P. Nordlander, R.E. Smalley. Electronic structure of small GaAs clusters II. *J. Chem. Phys*. 1992. 97(3): 1858.

[7] M.A. Al-Laham, K. Raghavachari. Theoretical study of small gallium arsenide clusters. *J. Chem. Phys*. 1991. 187(2): 13-20.

[8] R.M. Graves, G.E. Scuseria. Ab initio theoretical study of small GaAs clusters. *J. Chem. Phys*. 1991. 95(9): 6602.

[9] J.-Y. Yi. Atomic and electronic structures of small GaAs clusters. *Chem. Phys. Lett.* 2000. 325: 269-274.

[10] P. Piquini, A. Fazzio, S. Canuto. Ab initio self-consistent-field studies of the structures, energetics and bonding of small gallium arsenide clusters. *Zeitschrift Für Physik D*: Atoms, Molecules and Clusters. 1995. 33(2): 125-131.

[11] M.Z. Liao, D.G. Dai, K. Balasubramanian. Electronic states of the Ga_3As_2 and Ga_2As_3 clusters. *Chem. Phys. Lett*. 1995. 239: 124-130.

[12] G.W. Lemire, G.A. Bishea, S.A. Heidecke, M.D. Morse. Spectroscopy and electronic structure of jet-cooled GaAs. *J. Chem. Phys*. 1990. 92(121): 121.

[13] R. Schäfer, S. Schlecht, J. Woenckhaus, J.A. Becker. Polarizabilities of isolated semiconductor clusters. *Phys. Rev. Lett*. 1996. 76: 471-474.

[14] J.A. Becker. Molecular beam studies on semiconductor clusters: Polarizabilities and chemical bonding. *Angew. Chem. Int. Ed*. 1997. 36(14): 1390-1404.

[15] A. P. Alivisatos. Semiconductor clusters, nanocrystals and quantum dots. *Science, New Series*. 1996. 271(5251): 933 – 937.

[16] Jing Shi, S. Gider, K. Babcock, D. D. Awschalow. Magnetic clusters in molecular beams, metals, and semiconductors. *Science, New Series*. 1996. 271(5251): 937 – 941.

[17] David J. Wales. Structure, dynamics and thermodynamics of clusters: Tales from topographic potential surfaces. *Science, New Series*. 1996. 271(5251): 925 – 929.

[18] Keith D. Ball, R. Stephen Berry, Ralph e. Kenz, Feng-Yin Li, Ana Proykova, David J. Wales. From topographies to dynamics on multidimensional potential energy surface of atomic clusters. *Science, New Series*. 1996. 271(5251): 963 – 966.

[19] K. Liu, J. D. Cruzan, R.J. Saykally. Water Clusters. *Science, New Series*. 1996. 271(5251): 929 – 933.

[20] Gustavo E. Scuseria. Ab Initio calculations of fullerenes. *Science, New Series.* 1996. 271(5251): 942 – 945.

[21] P. Piquini, S. Canuto, A. Fazzio. Structural and electronic studies of Ga_3As_3, Ga_4As_3 and Ga_3As_4. *Int. J. Quantum Chem.* 1994. 52(S28): 571-577.

[22] P. Korambath, S.P. Karna. (Hyper) polarizabilities of GaN, GaP and GaAs clusters: An initio time dependent Hartree-Fock study. *J. Phys. Chem. A*. 2000. 104(20): 4801-4804.

[23] M.A Al-Laham, G.W. Trucks, K. Raghavachari. Theoretical study of small aluminium phosphide and magnesium sulfide clusters. *J. Chem. Phys*. 1992. 96(2): 1137.

[24] U. Meier, S.D. Peyerimhoff, F. Grein. Ab initio MRD-CI study of $GaAs^-$, $GaAs_2(\pm)$, $Ga_2As_2(\pm)$ and As_4 clusters. *Chem. Phys*. 1991. 150(3): 331-351.

[25] P.Y. Feng, K. Balasubramanian. Electronic state of Ga_2P_2. *Chem. Phys. Lett.* 1996. 258(4): 387-392.

[26] Serdar Öğüt. First Principles Modeling of Nanostructures. *Turkish Journal of Physics*. 2003. 27(5): 443-458.

[27] C. Delerue and M. Lannoo. *Nanostructures: Theory and Modelling*. Berlin: Springer. 2004.

[28] Takeyce K. Whittingham. *Scaling Relations in Density Functional Theory and Applications of Electronic Structure Methods*. PhD Dissertation. The State University of New Jersey; 2004.

[29] Attila Szabo and Neil S. Ostlund. *Modern Quantum Chemistry: Introduction to Advanced Electronic Structure Theory*. Revised Edition. US: McGraw-Hill. 2003.

[30] Enrico Lipparini. *Modern Many-Particle Physics: Atomic Gases, Quantum Dots and Quantum Fluids*. Singapore: World Scientific, 2003.

[31] L. H. Thomas. The calculation of atomic fields. *Proc. Cambrigde Philos. Soc*. 1927. 23: 542.

[32] E. Fermi. Application of statistical gas methods to electronic systems. *Atti. Accad. Naz. Lincei, Cl. Sci. Fis. Mat. Nat. Rend*. 1927. 6: 602.

[33] P. A. M. Dirac. Quantum Mechanics of Many-Electron Systems. *Proc. Royal Soc.(London) A.* 1929. 123(792)**:** 714-733.

[34] S. J. Vosko, L. Wilk and M. Nusair. Accurate spin-dependent electron liquid correlation energies for local spin density calculations: A critical analysis. *Can. J. Phys.* 1980. 58: 1200.

[35] J. P. Perdew and A. Zunger. Self-interaction correction to density-functional approximations for many-electron systems. *Phys. Rev. B*. 1982. 23(10):5048-5079.

[36] D. M. Ceperley and B. J. Alder. Ground State of the Electron Gas by a Stochastic Method. *Phys. Rev. Lett.* 1980. 45(7): 566.

[37] P. Hohenberg and W. Kohn, Inhomogeneous Electron Gas. *Phys. Rev.* 1964. 136(3B): B864 - B871.

[38] J. Kohanoff and N.I. Gidopoulos, Density Functional Theory: Basics, New Trends and Applications. In: Stephen Wilson. *Handbook of Molecular Physics and Quantum Chemistry*. Chichester: John Wiley & Sons. Volume **2**, Part 5, Chapter 26, 532–568; 2003.

[39] D. C. Langreth and M. J. Mehl. Easily Implementable Nonlocal Exchange-Correlation Energy Functional. *Phys. Rev. Lett.* 1981. 47(6): 446-450.

[40] Langreth, D.C. and Mehl, M.J. Beyond the local-density approximation in calculations of ground-state electronic properties. *Phys. Rev. B*. 1983, 28(4): 1809.

[41] Perdew, J.P. and Wang, Y. Accurate and simple density functional for the electronic exchange energy: Generalized gradient approximation. *Phys. Rev. B*. 1986. 33(12): 8800-8802.

[42] J. P. Perdew. Density-functional approximation for the correlation energy of the inhomogeneous electron gas,*Phys. Rev. B*. 1986. 33(12): 8822-8824.

[43] A. D. Becke. Density-functional exchange-energy approximation with correct asymptotic behavior. *Phys. Rev. A*. 1988. 38(6): 3098-3100.

[44] Chengteh Lee, Weitao Yang, and Robert G. Parr. Development of the Colle-Salvetti correlation-energy formula into a functional of the electron density. *Phys. Rev. B*. 1988. 37(2): 785-789.

[45] J. P. Perdew and Y. Wang. Accurate and simple analytic representation of the electron-gas correlation energy. *Phys. Rev. B*, 1992. 45(23): 13244-13249.

[46] J. P. Perdew, Unified Theory of Exchange and Correlation Beyond the Local Density Approximation. In: P. Ziesche and H. Eschrig. *Electronic Structure of Solids '91,* Berlin: Akademie Verlag, 11-20; 1991.

[47] J. P. Perdew, K. Burke and M. Ernzerhof. Generalized Gradient Approximation Made Simple. *Phys. Rev. Lett.* 1996. 77(18): 3865-3868.

[48] J. P. Perdew, K. Burke and M. Ernzerhof. Generalized Gradient Approximation Made Simple. *Phys. Rev. Lett.*1997. 78**:** 1396 (E).

[49] Yingkai Zhang and Weitao Yang. Comment on "Generalized Gradient Approximation Made Simple". *Phys. Rev. Lett*. 1998. 80(4): 890 – 890.

[50] M. Levy and J. P. Perdew. Hellmann-Feynman, virial, and scaling requisites for the exact universal density functionals. Shape of the correlation potential and diamagnetic susceptibility for atoms, *Phys. Rev. A.* 1985. 32(4):2010-2021.

[51] E. H. Lieb and S. Oxford. An Improved Lower Bound on the Indirect Coulomb Energy. *Int. J. Quantum Chem*. 1981. 19:427.

[52] R. P. Feynman. Forces in Molecules. *Phys. Rev*. 1939. 56(4): 340 – 343.

[53] J. C. Slater. Atomic Shielding Constants. *Phys. Rev*. 1930. 36(1): 57 – 64.

[54] W. J. Hehre, R. F. Stewart, and J. A. Pople. Self-Consistent Molecular Orbital Methods. I. Use of Gaussian Expansions of Slater Type Atomic Orbitals, *J. Chem. Phys*. 1969. 51(6): 2657-2664.

[55] W. J. Hehre, W. A. Lathan, R. Ditchfield, M. D. Newton, and J. A. Pople, *Gaussian 70,* Quantum Chemistry Program Exchange, Program No. 237, 1970.

[56] M. T. Yin and Marvin L. Cohen. Theory of ab initio pseudopotential calculations. *Phys. Rev. B*. 1982. 25(12): 7403 – 7412.

[57] P. E. Blöch. Projector augmented-wave method. *Phys. Rev. B*. 1994. 50(24): 17953.

[58] A.R. Tackett, N.A.W. Holzwarth and G.E. Matthews. A Projector AugmentedWave (PAW) code for electronic structure calculations, Part II: pwpaw for periodic solids in a plane wave basis. *Computer Physics Communications*. 2001. 135(3): 348–376.

[59] Georg Kresse and Jürgen Furthmüller. *VASP the GUIDE*. Institut für Materialphysik, Universität Wien. 2005. (retrieved from: http://cms.mpi.univie.ac.at/VASP/)

[60] G. Kresse and J. Joubert. From ultrasoft pseudopotentials to the projector augmented wave method. *Phys. Rev. B*. 1999. 59(3): 1758-1775.

[61] H. J. Monkhorst and J. D. Pack. Special points for Brillouin-zone integrations. *Phys. Rev. B*. 1976. 13(12): 5188-5192.

[62] R. O. Jones. Cluster Geometries From Density Functional Calculations – Prospects and Limitations. Eur. Phys. J. D. 1999. 9: 81-84.

[63] N. Metropolis, A.W. Rosenbluth, M.N. Rosenbluth. A.H. Teller and E. Teller. Equation of State Calculations by Fast Computing Machines. *J. Chem. Phys*. 1953. 21(6): 1087-1092.

[64] R.C. Weast. *Handbook of Chemistry and Physics*. 62nd ed. CRC Press, Inc, Boca Raton. 1981.

[65] Andréîa Luísa da Rosa. *Density Functional Theory Calculations on Anti-Surfactants at Gallium Nitride Surface*. Master Dissertation. Universität Berlin; 2003.

[66] G. S. Rohrer. *Structure and Bonding in Crystalline Materials*. Cambridge University Press, Cambridge, England. 2001.

[67] Thang B. Hoang, L. V. Titova, H. E. Jackson and L. M. Smith; *Imaging and optical properties of single core-shell GaAs-AlGaAs nanowires*. University of Cineinnati, OH. 2006.

[68] K. Balasubramaniam. Electronic states of GaAs and $GaAs^+$. *J. Chem. Phys*. 1987. 86(6): 3410.

[69] G.E. Scuseria. Application of open-shell coupled cluster theory to the ground state of GaAs. *Theor. Chim. Acta*. 1991. 80: 215-219.

[70] P. Karamanis, D. Begue and C. Pouchan. Ab initio finite field (hyper) polarizability computations on stoichiometric gallium arsenide clusters Ga_nAs_n (n = 2-9). *J. Chem. Phys*. 2007. 127: 094706.

[71] K. Balasubramaniam. Spectroscopic constant for $GaAs_2^-$, $GaAs_2$, Ga_2As^- and Ga_2As. *J. Phys. Chem. A*. 2000. 104(10): 1969-1973.

[72] T. R. Taylor, H. Gomez, K. R. Asmis and D. Neumark. Photoelectron spectroscopy of GaX_2^-, Ga_2X^-, $Ga_2X_2^-$ and $Ga_2X_3^-$ (X = P, As). *J. Chem. Phys*. 2001. 115: 4620.

[73] J. J. Belbruno. Bonding and energetics in small clusters of gallium and arsenic. *Heteratomic chem*. 2003. 14: 189-196.

[74] S. Brownridge and F. Grein. Geometries, electronic g-tensor elements, hyperfine coupling constants and vertical excitation energies for small gallium arsenide doublet radicals, Ga_xAs_y (x + y = 3, 5). *J. Phys. Chem. A*. 2003. 107(39): 7969-7980.

[75] A. Costales, A. K. Kandalam, R. Franco and R. Pandey. Theoretical study of structural and vibrational properties of $(AlP)_n$, $(AlAs)_n$, $(GaP)_n$, $(GaAs)_n$, $(InP)_n$ and $(InAs)_n$ clusters with n = 1,2,3. *J. Phys. Chem. B*. 2002. 106: 1940-1944.

[76] X. Zhu, Spectroscopic properties of gallium arsenide tetramers: Ga2As2, $Ga_2As_2^+$ and $Ga_2As_2^-$. *Spectrochim. Acta A*. 2005. 61: 2730-2736.

[77] S. Burrill and F. Grein. Structure and bonding of III/V compounds X_2Y_2 with X_2B, Al, Ga and Y = N, P, As. *J. Mol. Struct. Theochem*. 2005. 757: 137-142.

[78] S. Li, R. J. Van Zee and W. Weltner Jr. Hyperfine interaction and structure of a gallium arsenide cluster: Ga2As3. *J. Chem. Phys*. 1993. 98: 4335

[79] Bei Liu, Zhong- Yi Liu, Bicai Pan, Cai-Zhuang Wang and Kai-Ming Ho. Ionization of medium sized clusters and the geometries of the cations. *J. Chem. Phys*. 1998. 109(21): 9401 – 9409.

[80] Q. L. Lu, J. C. Jiang, J. G. Wan and G. H. Wang. Density-functional study of ring-like Ga_nAs_n ($3 \leq n \leq 14$) clusters. *J. of Molecular Structure*. 2008. 851: 271-276.

[81] Thomas Bachels, Rolf Schäfer. Binding energies of neutral silicon clusters. *Chem. Phys. Lett.* 2004. 324: 365-372.

[82] C. Jin, K. J. Taylor, J. Conceicao and R. E. Smalley. Ultraviolet photoelectron spectra of gallium arsenide clusters. *Chem. Phys. Lett*. 1990. 175: 17-22.

[83] D. J. Frankel, C. Yu, J. P. Harbison and H. H. Farell. High- resolution electron energy loss spectroscopy studies of GaAs (100) surfaces. *J. Vac. Sci. Technol. B* .1987. 5(4): 1113-1118.

[84] J. A. Schaefer, T. Allinger, C. Stuhlman, U. Beckers and H. Ibach. Interaction of hydrogen at GaAs (100) surfaces. *Surf. Sci.* 1991. 251/252: 1000-1005.

[85] E.D. Lu, Y. Yang, X. J. Zhou, S.A. Kellar, P. V. Bogdanor, A.C. Huan, F. Cerina, Z. Hussain and Z. X. Shen. *Photoemission spectromicroscopy study on passivation of GaAs (100) by CH_3CSNH_2 / NH_4OH*. University Stanford, Stanford. CA94305.

[86] Ronald Schailey and Asok K. Ray. A cluster approach to hydrogen chemisorption on the GaAs (100) surface. *J. Computational Material Science*. 2001. 22: 169-179.

[87] Asok K. Ray and Michael L. Mayo. *An ab initio cluster study of atomic oxygen chemisorption on Ga-rich GaAs (100) (2x1) and β(4x2) surface*: University of Texas at Arlington, Arlington, Texas 76019.

[88] Kurt A. Johnson and N. W. Ashcraft. Corrections to Density-Functional Theory Band Gaps. *Phys. Rev. B*. 1998. 58(23): 15548-15556.

[89] Norahanim Mohd Jais. *Ujian Prestasi Pembangunan Makmal Pemprosesan Selari Dengan Antaramuka Laluan Pesanan (MPI) Kaedah Pengenduran Berturut-turut Merah Hitam (SOR RED BLACK)*. Degree Dissertation, Universiti Teknologi Malaysia; 2002.

[90] Lee Jia Yen. *Electronic Structures of Silicon Quantum Dots as Nanoclusters for Single Electron Transistors*. Master Dissertation, Universiti Teknologi Malaysia; 2008.

[91] P. Pulay. Convergence Acceleration in Iterative Sequences: The Case of SCF Iteration. *Chem. Phys. Lett*. 73, 393 (1980) .

[92] P. Pulay and S. Saebo: Variational CEPA: Comparison with Different Many-body Methods. *Chem. Phys. Lett*. 117, 37 (1985).

APPENDIX A

Parallelization of VASP

Traditionally, software has been written for serial computation executed on a single computer having a single Central Processing Unit (CPU). A problem is broken into a discrete series of instructions and carried out one after another. In this case, only one instruction may execute at any moment in time. Therefore, when a CPU is given a massive and complex ab-initio calculation, it will take a very long time to handle and the calculation might fail due to the insufficient memory problem. This serial computing problem can be solved by parallel computing, which is the simultaneous execution of the same task on multiple processors in order to obtain results faster. A problem can be divided into smaller task and broken down to a series of instructions. These instructions from each task execute simultaneously on different CPUs.

Parallel version of VASP is available and computer cluster approach (see Figure 2) is used in this research. Computer cluster is a group of tightly coupled computers that work together closely so that in many respects they can be viewed as though they are a single computer. The components of a cluster are commonly connected to each other through fast local area networks. The cluster built can be categorized as high-performance cluster (HPC). HPC with nodes running Linux as the OS and free software to implement the parallelism is often referred to as a Beowulf cluster.

Figure 1 shows the parallel computing cluster used for VASP calculation in this research. The following lists the important components including hardware and software of the Beowulf cluster used for the VASP calculation:

i) 11 units of CPU with Intel 3.06Ghz Pentium 4 Hyper-Threading
ii) Gigabit Ethernet card

iii) Gigabit network switch

iv) Operating system of Fedora Core 4

v) MPICH2 for the MPI implementation

Network is an important element in determining the performance of the parallel cluster. It had been shown that Gigabit cards can reduce the latency (delay-time for a packet of data to get from one designated point to another) to 30 μs in comparison to the typical 100 MBit Ethernet based network which shows around 90 μs latency. In consideration of bandwidth (maximum transfer rate limits the communication speed), VASP uses all-to-all communication.

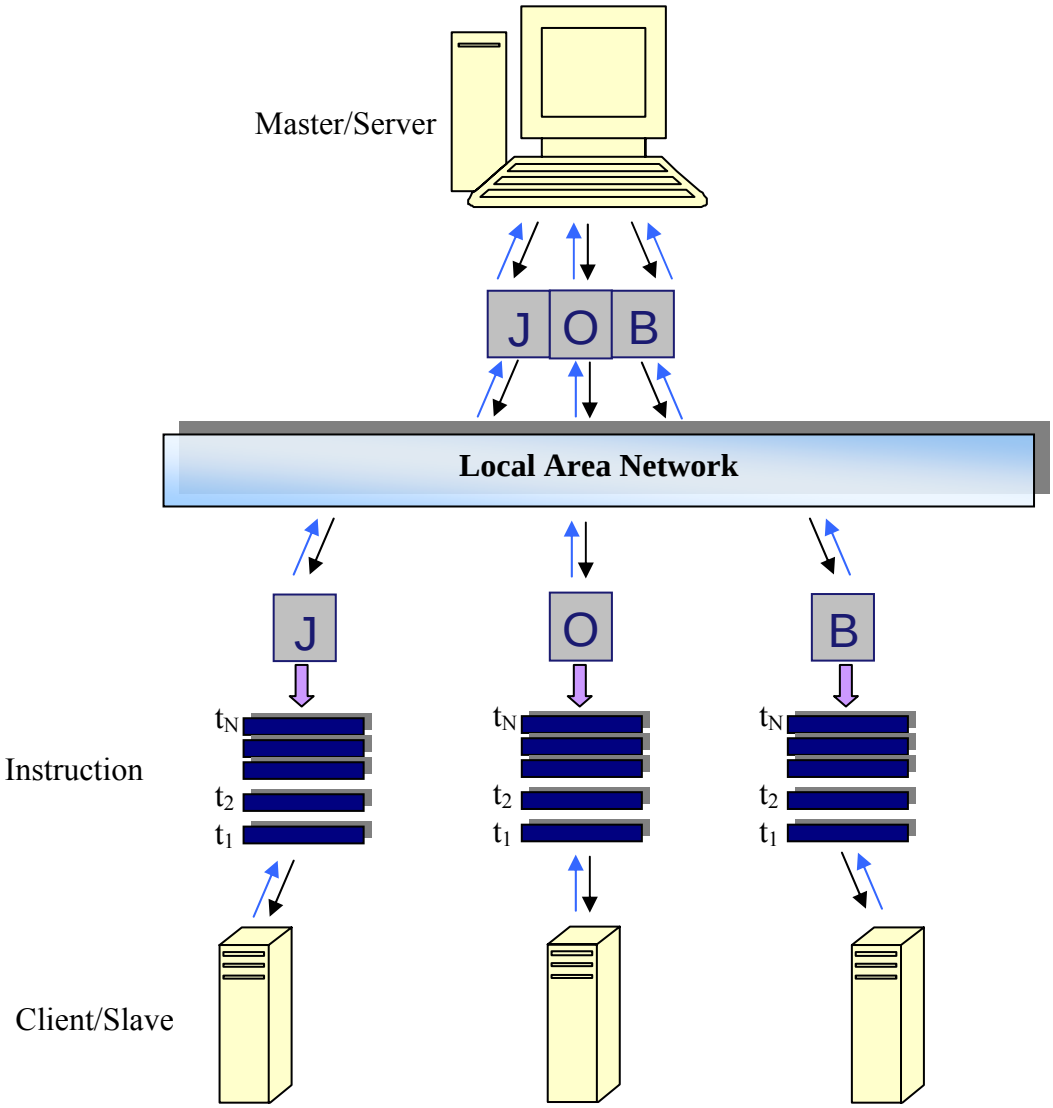

Figure 1. Schematic of parallel computing cluster illustrating a master-server distributes a job to 3 client nodes and communication between them is showed.

The MPI version of VASP is compiled and installed by using the Fortran 90 of Intel Fortran Compiler (IFC). Therefore, MPICH2 is also compiled by using IFC before the installation of VASP. Below are the brief descriptions on how to build the 11-nodes Beowulf cluster:

1) The network of the cluster is configured. Hostnames and unique IP addresses are assigned for each node in the cluster. All the nodes should be in the same local network. One node is designated as the master node and is assigned IP address of 192.168.10.101. IP address is added one for each client node (192.168.10.102, etc.) for easy recognition and there would be no problem as long as the IP address is in the range of 192.168.10.255. The nodes are named setpar01 through setpar11 to keep things simple, using setpar01 as the master node. An identical user account is created in all nodes so that VASP is run as common user but not root.

2) The communication protocol of the cluster is configured. There are commonly two protocols which are RSH and SSH. Because of the cluster is exposed to the public networks, SSH (Secure Shell) is chosen to provide a more secure system since it encrypts all communication by means of private plus public key encryption methods. The MPICH2 must be also using SSH protocol.

3) Password-less login is enabled. The communication between the cluster nodes must be free from password request to ensure a non-barrier environment for data sending and receiving. This can be done by first enabling the global cluster node authentication. A database of all nodes' public keys is kept in the file named ‘ssh_known_hosts’ in the SSH directory and this file is saved in each of the node. In the second step, the list of all hostnames of the cluster nodes is created in the file ‘shosts.equiv’ in SSH directory and also list of all hosts and user who allowed to log in is created in file ‘.shosts’ in home directory. This is a authentication method combines shosts or shosts.equiv with RSA-based host authentication. It means that is the login would be permitted by ~/.shosts or /etc/ssh/shosts.equiv, and additionally it can verify the client’s host key from /etc/ssh/ssh_known_host, only then login is permitted. This authentication method closes security holes due to IP spoofing, DNS spoofing and routing spoofing.

4) NFS (Network File System) server and clients is configured. NFS allows hosts to mount partitions on a remote system and use them as though they are local file systems. This allows the system administrator to store resources in a central location on the network, providing authorized users continuous access to them. Master node is configured to be NFS server and shares the directory of VASP and MPICH2 with other client nodes.

5) MPICH2 is configured and a file mpd.hosts containing a list of hostnames is created. The process manager of MPICH2 which is called MPD will start the MPI jobs on the nodes specified in the file.

6) VASP is run by giving the command 'mpiexec –np 11 <directory of VASP>' in the working directory where the calculation is to be run.

Figure 2. Cluster of parallel-computing set up for VASP calculation.

Performance of Parallelization

To test the performance of the parallelization of VASP, two factors were studied, which are speedup and efficiency. Speedup refers to how much a parallel algorithm is faster than a corresponding sequential algorithm. It is defined by the following formula:

$$S_N = \frac{T_1}{T_N} \quad , \quad 1 \leq S_N \leq N$$

where N is the number of processors, T_1 is the execution time of the sequential algorithm, and T_p is the execution time of the parallel algorithm with p processors [103]. Ideal speedup is $S_N = N$, which is called linear speedup. Efficiency is a performance metric estimating how well-utilized the processors are in solving the problem compared to how much effort is wasted in communication and synchronization. It is defined as:

$$E_N = \frac{S_N}{N} \quad , \quad 0 \leq E_N \leq 1$$

Algorithms with linear speedup and algorithms running on a single processor have an efficiency of 1.

Table 1. Execution time, speedup and efficiency of VASP using parallel computing

Number of CPU	Execution Time (s)	Speedup	Efficiency
1	308.447	1	1
2	180.798	1.706031	0.853016
3	131.688	2.342256	0.780752
4	109.984	2.804472	0.701118
5	92.549	3.332797	0.666559
6	80.901	3.812648	0.635441
7	73.709	4.184659	0.597808
8	68.259	4.518774	0.564847
9	65.806	4.687217	0.520802
10	61.958	4.978324	0.497832
11	57.473	5.366816	0.487892

Figure 2 and 3 show a simple performance benchmark of VASP running at 2 to 11 CPUs. It is obvious that the execution time for the parallel calculation reduces as the number of CPU increases (refer to Table 1).

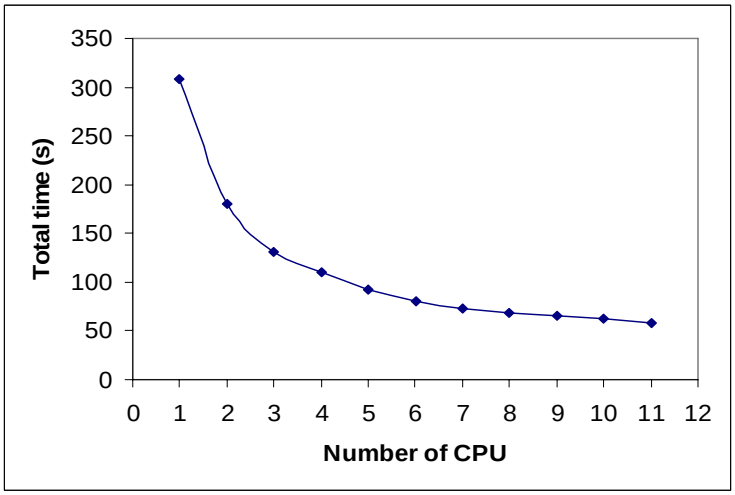

Figure 2. Graph of total time used for completing a parallel calculation versus the number of CPU.

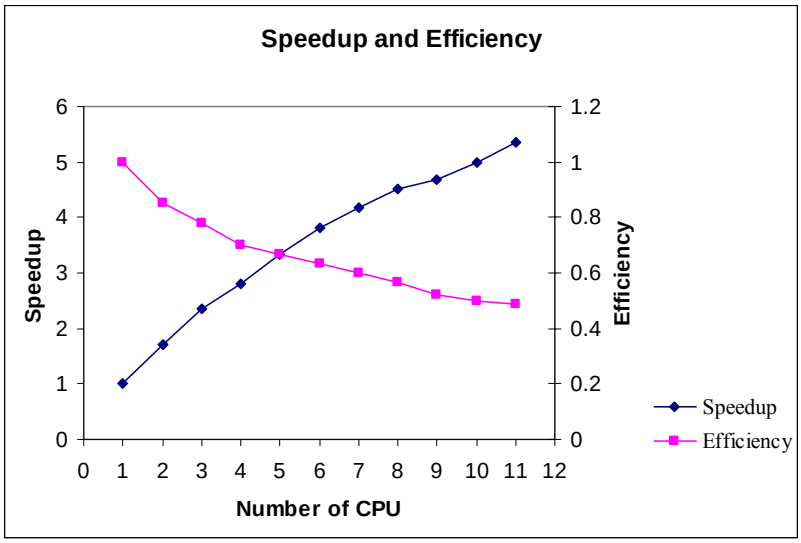

Figure 3. Graph of speedup and efficiency vs number of CPU.

From the graph, it can be observed that the speedup is not linear. For 11 CPUs, the speedup is 5.4 times faster than the sequential algorithm. Both speedup and efficiency trends show the decreasing of the speedup and efficiency as the number of CPU increases. This is owing to the communications between the CPUs are getting more massive when the number of CPU increases.